THE GRAVITATIONALLY LENSED GALAXY IRAS FSC 10214+4724

Roger Paul Deane

Jesus College, Oxford

A thesis submitted for the degree of Doctor of Philosophy
in the University of Oxford.

Hilary Term 2012

Dedicated to mentors, and to those who have lost one.

Three giants in my life were lost in the final nine months of this thesis. I will be eternally grateful for their intellectual, moral, and emotional guidance.

Steve, you really were larger than life. I arrived in Oxford thinking what a privilege it was. Yet, the privilege of learning from you dwarfed everything else.

DJ, the wisdom and love you brought to us all during your shortened life is the only reprieve we clutch onto in the immensity of losing you.

Oumsie, jou liefde het geen grense geken nie. Soos jy altyd gese het, 'n duisend dankie vir alles. Al my liefde 'n duisend keer oor.

Declaration

I declare that no part of this thesis has been accepted, or is currently being submitted, for any degree or diploma or certificate or any other qualification in this University or elsewhere. Except where explicit reference is made to the work of others, the work contained in this thesis is my own. The *GMRT* 330 MHz data in Chapter 3 were reduced by Tom Mauch and Hans-Rainer Klöckner. The *AMI* 16 GHz data in Chapter 3 were reduced by Keith Grainge.

Roger P. Deane

February 2012

Acknowledgements

Before Steve's tragic death, I had written the following in an early draft of my thesis: "Firstly, I would like to extend my deepest thanks to my supervisor, Steve Rawlings. He has never failed to make even the most challenging of tasks seem easily achievable. He has inspired me to push myself and demand a high standard of research, but somehow maintained a relaxed, easy-going relationship at the same time. I am greatly indebted for this privledged experience." I am happy that I would write something very similar, but saddened that he would never read it. Steve was an incredible mentor who will always have a profound imprint on my life and the way I think. I hope he knew how deeply I respected him.

Ian Heywood has been a constant source of scientific, technical and moral support. I am grateful for his guidance and ever-ajar office door.

Phil Marshall made essential contributions to this work at a critical period in my D.Phil. I greatly appreciate his patience with a lensing enthusiast significantly his junior.

I am greatly indebted to Mike Garrett for his feedback on the VLBI chapter after Steve's passing. He gave of his time despite being wedged between a plethora of *SKA* meetings.

Hans-Rainer Klöckner shared a great deal on expert radio interferometric data reduction and analysis, particularly in VLBI.

Mike Garrett, Zsolt Paragi, Bob Campbell and Richard Porcas provided heaps and heaps of expert advice in the design, scheduling, and reduction of VLBI observations. Anita Richards was very helpful and generous with her time in passing on some of the nuances of calibrating *MERLIN* data.

Alejo Martínez-Sansigre gave freely of his time through many detailed conversations and mini-tutorials. Later on, his student Hana Schumacher provided an excellent crash course in LVG modelling.

Aprajita Verma offered many enlightening discussions (and encouragement) on IRAS 10214 in particular, sharing great insight in optical/IR observations and analysis.

I must thank my brilliant office mates: Henry Tillson, Olaf Davis and Sarah Miller. Our frequent discussions were a wonderful confluence of not only theory, simulation, and observation in astrophysics, but also on life beyond our work. I have a deep respect for these outstanding scientists.

The Oxford *SKA* research group has been a very supportive and enriching set of friendships, not only in radio astronomy matters. In this much thanks go to Charles Copley, Aris Karastergiou, Ian Heywood, Danny Price, Griffin Foster, Jack Hickish, Kris Zarb Adami, Richard Armstrong and Tom Mauch.

The Oxford graduate group is a particularly vibrant, closely-knit community. I have greatly enjoyed tea and pub-time conversations with this diverse group. In particular I would like to thank Richard Masters, Cristina Fernandez, James Allison, Natalie Christopher, Jasmeer Virdee and Thibault Louis.

One of the key attributes of life in Oxford is the collegiate system. I am very grateful to the life-long friendships I have made at Jesus College. The high intellectual level; mix of research themes, nationalities and personalities; and general relaxed atmosphere led to an experience that broadened my view of the world in a way that I will always be grateful for. I am also very grateful to Jesus College for awarding me a graduate scholarship from 2009-2011.

All the great house-mates (and alumni) of 26 Western Road provided me with what was truly a home away from home. Thanks to each of you for your wonderful spirit and (in)famous house parties. I would also like to thank my friend Lyle (Bubs) Murray for making sure my head was above water in the final year of the D.Phil.

My family provided much support during my time at Oxford, keeping me rooted to African soil. My parents have shown great strength and courage in evermore trying circumstances. They continue to provide much inspiration. I look forward to living in the same city as my two sisters Shani and Kerry, and brother Tim for the first time in over 20 years.

Tess has somehow managed to show great courage and provide sustained support through ultimate tragedy. For this I will always be grateful beyond words.

Abstract

We present a multi-wavelength analysis of IRAS FSC 10214+4724 from radio to X-ray wavelengths. This is a gravitationally lensed galaxy at z=2.3 (3 Gyr after the Big Bang) which hosts prodigious star formation as well as an obscured active nucleus. We derive a new lens model for the system employing a Bayesian Markov Chain Monte Carlo algorithm with extended-source, forward ray-tracing. An array of spatially resolved maps (radio, millimetre, near-infrared, optical) trace different physical components which enables a high resolution, multi-wavelength view of a high-redshift galaxy beyond the capabilities of current telescopes. The spatially-resolved molecular gas total intensity and velocity maps reveal a reasonably ordered system, however there is evidence for minor merger activity. We show evidence for an extended, low-excitation gas reservoir that either contains roughly half the total gas mass or has a different CO-to-H_2 conversion ratio. Very Long Baseline Interferometry (VLBI) is used to detect what we argue to be the obscured active nucleus with an effective angular resolution of $\lesssim$ 50 pc at $z = 2.3$. The source plane inversion places the VLBI detection to within milli-arcseconds of the modeled cusp caustic, resulting in a very large magnification ($\mu \gtrsim$70) which is over an order of magnitude larger than the derived CO$\,(1\rightarrow0)$ magnification. This implies an equivalent magnification difference between the starburst and AGN components, yielding significant distortion to the global continuum spectral energy distribution (SED). A primary result of this work is therefore the demonstration that emission regions of differing size and position within a galaxy can experience significantly different magnification factors ($>$ 1 dex) and therefore distort our view of high-redshift, gravitationally lensed sources. This not only raises caution against unsophisticated uses of IRAS 10214 as an archetype high-redshift Ultra-Luminous Infra-Red Galaxy (ULIRG), but also against statistical deductions based on samples of strong lenses with poorly constrained lens models and spatially-unresolved detections. Analogous to the continuum SED distortion quantified in this thesis, we predict a

distortion of the CO spectral line energy distribution of IRAS 10214 where higher order *J* lines, that are increasingly excited by the AGN and shock heating from the central starburst, will be preferentially lensed owing to their smaller solid angles and closer proximity to the AGN, and therefore the cusp of the caustic. This distortion is predicted to affect many high redshift lenses and will be tested most synergistically by the *Jansky Very Large Array (JVLA)* and the *Atacama Large Millimetre Telescope (ALMA).*

Contents

Appendices

CHAPTER 1

INTRODUCTION

This thesis reports the results of an extensive observing programme of one of the most famous high-redshift galaxies: IRAS FSC10214+4724 (IRAS 10214 hereafter). In the early 1990s, it appeared to be the most luminous object in the Universe (Rowan-Robinson et al., 1991). A myriad of observations with the world's premier ground- and space-based facilities followed its discovery to investigate what was thought to be a primeval galaxy due to its extra-ordinary apparent bolometric luminosity. One notable attribute of its history is that it was the first CO detected galaxy at high redshift (Brown & Vanden Bout, 1991), which was followed by the major new research thrust of high-redshift molecular gas studies; a key science goal of the *JVLA* and *ALMA*. 2011 marked the 20^{th} year since the discovery of IRAS 10214, which has over 100 publications with titled matches using NASA's Astrophysics Data System (ADS) Bibliographic Services. For this reason, one might question if a PhD thesis dedicated to its study is justified. However, as is almost always the case in scientific enquiry, answers are followed by even more questions. This is particularly true in the case of IRAS 12014 since new observations have revealed counter-intuitive, and in some cases, seemingly conflicting results. Furthermore, new and upgraded telescopes enable new observational opportunities to investigate this galaxy which is very often used as an archetype high-redshift Ultra-Luminous InfraRed Galaxy (ULIRG) in comparison with other high-redshift galaxies. Broadly, this work focuses on two themes:

- Development of a Bayesian Markov Chain Monte Carlo, extended-source, gravitational lensing algorithm to derive a robust lens model of IRAS 10214 and fully exploit the wealth of ground- and space-telescope observations.

- Design and analysis of new observations, specifically to disentangle emission from star formation and the actively accreting super-massive black hole (SMBH) in IRAS 10214.

As will be discussed later, detailed observations of the earliest galaxies is of fundamental importance in contemporary astrophysics and cosmology. Detailed analyses of appropriate cosmic laboratories are an essential ingredient in the triad of observation, theory and simulation. Each progresses at its own rate, while being driven by breakthroughs in the other disciplines. Numerical simulations and the observational domain in particular are on the cusp of exponential growth in the next 1-2 decades enabled by technology advancement as astrophysics moves into the regime of building large-scale, multi-purpose facilities. There are currently a large number of such facilities in the planning or commissioning phase across the electromagnetic spectrum. The sensitivity, angular resolution, survey speed, and instrument flexibility of these observatories will dramatically increase the range of feasible scientific investigations, and gravitational lensing provides a preview of such possibilities with these next-generation telescopes. The effective sensitivity and spatial resolution afforded by strong-lensing greatly enhances current observing capabilities, *provided the lenses can be accurately modelled.* In addition to the large number of new observatories in planning/commissioning, instruments are becoming significantly easier to use and understand for the non-specialist, enabling a more multi-wavelength analysis in any given project. In this way, observers are moving to a more holistic approach to understanding the Universe rather than being entrenched in a particular observational window, as was the case in the past due to the required level of technical expertise in order to perform competitive experiments.

The rest of this introduction outlines the importance of studying the high-redshift Universe. Since Chapters 2-5 are stand-alone academic journal submissions, each of these chapters has its own introduction. This introductory chapter is therefore a brief, top-level overview. It is written from an observer's perspective, and more specifically with a radio astronomy bias, the region of the electromagnetic spectrum where the author finds himself most comfortable. Having stated this bias, we start with some context in describing large-scale structure formation in the Universe, and discuss how the first stars and black holes formed and re-ionised the Universe. We then provide an overview of how galaxies evolve from this early stage to what we observe in the local Universe. While there is much to be answered by the next-generation of astronomical facilities, the current and continuing understanding of galaxy formation and evolution is a testament to the remarkable progress made in 80 years of multi-wavelength astronomy.

1.1 The Early Universe

One of the great successes of astronomy is the emergence of a field coined 'precision cosmology' – the ability to make precision measurements of fundamental cosmological parameters enabled by a confluence of pioneering theoretical work (e.g. Silk, 1968); sophisticated space and ground-based instruments (e.g. *WMAP, Planck, ACT, SPT, CBI*); and large-scale cosmological simulations (e.g. Springel et al., 2005). This has been primarily driven by Cosmic Microwave Background (CMB) physics, specifically the temperature anisotropy angular power spectrum of the projected volume of last scattering (e.g. Spergel et al., 2007). But cosmological parameter constraints have come from a wide range of observational approaches including a measurement of the matter power spectrum (Eisenstein et al., 2005); the Hubble parameter from strong-lensing (e.g. Keeton & Kochanek, 1997); gas fractions and redshift-independent cluster surveys using the Sunyaev-Zel'dovich effect (see review in Carlstrom et al., 2002); and distance determinations of high-redshift supernovae showing an apparent acceleration of the expansion of the universe (Perlmutter et al., 1997; Schmidt et al., 1998).

From the improved measurement of cosmological parameters, a so-called standard model of cosmology has emerged, the ΛCDM model (e.g. Dodelson, 2003; Coles & Lucchin, 2002), where Λ denotes a vacuum energy present in empty space and CDM denotes Cold Dark Matter. This appears to be the simplest model that explains the large-scale structure of the Universe, the Cosmic Microwave Background (CMB) temperature power spectrum, and the apparent accelerated expansion of the Universe implied by high-redshift supernovae distance measurements (e.g. Dodelson, 2003). The standard model proposes that following the Big Bang, a rapid period of inflation occurred which flattened the Universe. At this time, the Universe was a smooth, almost featureless ionised plasma apart from tiny primordial density (ρ) compressions and rarefactions of order $\delta\rho/\rho \sim 10^{-5}$, where $\delta\rho$ is the energy-density contrast. In this early period the baryons and photons were coupled through Compton scattering. As expansion ensued and the Universe cooled to a temperature $T_{\mathrm{CMB}} \sim 3000$ K, the CMB photons and baryons began to decouple over a volume roughly centred on a redshift of $z \sim 1100$. This frozen volume of last scattering is the primary source of the inferred values in the cosmological standard model.

With the Compton scattering mean path rapidly increasing, the majority of photons begin to free-stream, leaving the dark matter and baryons which are weakly coupled by gravity. A characteristic trait of this era is the embedded sound horizon, observable as the primary peak in the matter power spectrum today on a scale of $D \sim 140$ Mpc, referred to as Baryonic Acoustic Oscillations (BAO), which can be used as a powerful cosmological 'standard ruler', enabling accurate distance estimation (Eisenstein et al., 2005). This is one of the key science objectives of a number of facilities to be built over the next 1-2 decades (e.g. *HETDEX, SKA, W-FIRST, EUCLID, BOSS*).

As the CMB photons decoupled, protons and electrons combined during the 'Recombination Era'. The Universe continued to expand, with the matter over-densities growing in amplitude. This period ($z \sim 15-3000$) is referred to as the dark ages given the lack of stars and accreting black holes. However, it is observable in principle by virtue of the 21 cm hyper-fine transition of neutral hydrogen and the matter anisotropy. The statistical properties of this period is a promising observational frontier (Hernandez & Holder, 2011; Pritchard & Loeb, 2008; Burns et al., 2012) however it has extraordinary sensitivity and calibration requirements due to the weakness of the signal and the myriad physical and instrumental contaminants.

A more feasible avenue, but still remarkably challenging, is the statistical detection and direct imaging of the epoch of re-ionisation (EoR), when the first galaxies and black holes re-ionised the Universe in the period constrained between $z \sim 6-15$ via the same H I emission line. The initial masses and conditions for Population III stars (e.g. Tumlinson & Shull, 2000; Dekel & Silk, 1986) and seed black holes (e.g. Volonteri et al., 2008) are observationally unconstrained, however they could only form once the matter over-densities had reached a critical level to allow gravitational collapse. These first stars and black holes emitted the ultraviolet and X-ray radiation (respectively) that re-ionised the Universe. The relative importance of stars and black holes during the epoch of re-ionisation is unknown but key statistical observational signatures for both have been theorised (e.g. Pritchard & Loeb, 2008) and will be tested by future 21-cm experiments (e.g. *LOFAR*, *SKA*, *HERA*). There are even ambitious plans to perform similar experiments with other spectral lines through the intensity mapping technique where low resolution ($\gtrsim$10 arcmin) observations map the aggregate signal of large numbers of high-redshift galaxies to probe EoR large-scale structure (e.g. CO, C II, Gong et al., 2011; Carilli, 2011; Lidz et al., 2011; Gong et al., 2012).

On a more individual level, direct observations of the galaxies that re-ionised the Universe have been and will be performed through the drop-out technique using the *HST* Wide Field Planetary Camera 3 (WFPC3) (e.g. Bouwens & Illingworth, 2010; Bunker et al., 2010); narrow-band *Ly-α* surveys (e.g. *Subaru*, Ota et al. 2010; *VISTA*) and through molecular tracers (high-J CO, C II with the *JVLA* and *ALMA*, e.g. Wang et al. 2010). Observations of individual galaxies will always remain important to probe the relevant physics which is linked to the cosmological conditions at their particular epoch, especially at high redshift.

1.2 Galaxy Formation and Evolution

As dark matter clustering ensues during the EoR, the most massive systems build up first, and constitute the hosts of the most massive galaxies and black holes. This is confirmed by a number of empirical results including: high-redshift radio luminosity functions (Dunlop & Peacock, 1990); clear evolution in the stellar mass function (traced by the stellar luminosity function, Bundy et al., 2006); as well as the X-ray luminosity function (Hasinger et al., 2005; Barger et al., 2005). As the most massive systems build up, star formation is largely driven by violent major mergers of two or more gas rich galaxies, with most Milky Way type galaxies expected to have had as least one major merger since $z \sim 1$. Direct evidence for this is provided by *HST* statistical morphology comparisons and close companion fractions of low- and high-redshift galaxies (e.g. Le Fèvre et al., 2000); as well as the detection of a population of submillimetre galaxies with exceptionally high star formation rates and broad, disrupted integrated CO spectra (Hughes et al., 1998; Frayer et al., 2000; Greve et al., 2005).

We observe a significant increase ($\gtrsim$1 dex) in the star formation rate density in the Universe as well as the number density of radio-loud quasars and hard X-ray point sources, proxies for SMBH accretion

(Madau et al., 1996; Dunlop & Peacock, 1990; Barger et al., 2005). At low to intermediate redshifts we observe clear statistical correlations between SMBH mass and the stellar bulge luminosity and velocity dispersions (Magorrian et al., 1998; Gebhardt et al., 2000; Tremaine et al., 2002). This implies a fundamental relationship between the growth of SMBHs and their host galaxies, and has spawned a new field within galaxy evolution studies referred to feedback, in which accretion onto the central SMBH has a radiative and/or mechanical regulation of star formation through gas expulsion. Feedback is not only generated by AGN, but by supernovae as well (Larson, 1974). The latter have greater significance in lower mass systems with shallower potential wells and lower angular momentum in their disks. It is asserted that both forms of feedback are necessary to reconcile numerically predicted stellar luminosity functions from ΛCDM cosmological simulations with the observations (see Silk, 2011, for a concise review). The strong correlations between SMBH mass with stellar velocity dispersion and bulge luminosity are promising in the sense that fundamental relationships have been identified, however, it is essential we pursue more detailed investigations to understand these cosmic trends and correlations on an individual level.

Through the study of low-redshift systems (e.g. Holt et al., 2008) and results from numerical simulations (e.g. Hopkins et al., 2006) we have a broad-based understanding of how galaxies plausibly form and evolve in a process of hierarchical merging, which triggers star formation and provides the angular momentum ‘kick’ leading to a significant increase in accretion onto central super-massive black holes. The latter process leads to jet outflows and super-winds which are thought to drive gas out of the galaxy through mechanical and radiative feedback, which in turn quenches star formation. However, detailed analyses of galaxies at the relevant cosmological epoch ($z \sim 2-3$) are essential to understand the underlying physical mechanisms more thoroughly.

However, the challenges faced by high-redshift observations are large, with 8 kpc arcsec^{-1} spatial resolution at $z \sim 2$. This rules out sufficiently spatially resolved images at these redshifts for most current observatories. This is a key observational goal of next-generation telescopes which will enable the detailed analyses on large samples of lower mass/luminosity systems necessary to probe the underlying physics. However, these capabilities can be probed by strong gravitational lensing - the technique employed in this thesis.

1.3 The Role of Strong Gravitational Lensing

We will introduce gravitational lensing in greater detail in Chapter 2, however, for the purposes of this overview we provide a qualitative description of the benefits, and challenges, offered by strong gravitational lensing. In short, this phenomenon results in the large magnification of a source (galaxy, quasar, star) by a foreground, line-of-sight gravitational potential, usually in the form of a massive cluster or elliptical galaxy. Strong lensing is an elegant interface of astrophysics and cosmology, since the optics depend on the mass distribution of the lensing galaxy(ies); and the geometry of the Universe (through the relative angular diameter distances of source, lens and observer). For this reason, strong lensing can be used not only to study high-redshift sources in greater detail (the focus of this thesis), but also to investigate dark matter distribution of lensing galaxies and clusters, as well as cosmography (see Schneider, 2006, for a comprehensive review). The latter is highly competitive with large-scale cosmology experiments, an example of which is the quasar $B\,1608{+}656$ (Suyu et al., 2010) which, when combined with WMAP5 results yields a Hubble Parameter estimate with 6.9% uncertainty (cf. 6.6% from WMAP5 + BAO, Percival et al., 2007). This demands sophisticated lens modelling techniques and a careful estimation of systematic uncertainties (see detailed description in Suyu et al., 2009).

Therefore, the price we pay for exploiting the angular and flux density boost afforded by strong lensing is the effort required in accurate model fitting and the additional uncertainties that result. Nonetheless, accurate, independently verified lens models are possible, which enable the study of high-redshift systems that would be out of reach without these ‘cosmic telescopes’. However, the effects of magnification bias and lensing distortions need careful consideration. In this thesis we consider an additional lensing effect not previously investigated in any great detail: the distortion of the global (radio through X-ray) SED, resulting from the differing *source* structure at different wavelengths. The latter is a result of different emission components that dominate the SED at different wavelengths due to their source size and position relative to the lensing galaxy. Therefore, this distortion is solely dependent on the multi-wavelength properties of the background, *lensed* source and not on the lensing potential distribution or geometry of the Universe. This has been referred to as ‘differential’ lensing by some authors, however we argue this is an inappropriate term since any source-plane image is differentially magnified due to the optics of the system. We use the term ‘preferential lensing’ for the purposes of this work to convey the idea that different emission regions (which dominate the global SED at different wavelengths) have different magnification factors based on their position and size. Therefore, preferential lensing at the very least avoids the confusion that arises between strong-lensing ‘chromacity’ and magnification varying as a function of position for any single frequency image of a strongly-lensed system.

The number of known strong lenses is currently of order $\sim$ 200 (Treu, 2010) and certainly at a sample size large enough to do meaningful statistical analyses. The sample size is set to increase by over 2 orders of magnitude in the coming decades with the number of large-scale facilities set to begin operating (Treu, 2010). It is therefore timely to characterise the effect of preferential lensing in a ‘well-known’ source with extensive multi-wavelength coverage, particularly since IRAS 12014 is a ‘cusp-caustic’ lens where the effects of preferential lensing should be most accentuated.

1.4 A Brief History of IRAS FSC10214+4724

Rowan-Robinson et al. (1991) first identified IRAS 10214 as the highest redshift ($z \sim 2.3$) source detected in the IRAS Faint Source Catalogue. For a period of time in the early 1990s its apparent bolometric luminosity, $L_{\rm bol,app} \sim 10^{14}$ $\rm L_{\odot}$, made it the most luminous object in the known Universe. This enormous luminosity, $\sim$99% of which is radiated in the infrared, led to suggestions that this was a primeval galaxy in the process of formation (Rowan-Robinson et al., 1991). However spectroscopic and morphological arguments purported IRAS 10214 to be gravitationally lensed by a foreground galaxy at redshift $z \sim 0.9$ resulting in a total magnification between 50-100 at rest-frame optical/UV wavelengths (see Broadhurst & Lehar, 1995; Serjeant et al., 1995; Close et al., 1995), *based on the observed arc-to-counter-image flux ratio*. The lensing hypothesis was quite spectacularly confirmed by high resolution imaging with the Hubble Space Telescope (Eisenhardt et al. *HST* 1996). Even after accounting for this high magnification factor, IRAS 10214 remained amongst the most luminous of the Ultra Luminous InfraRed Galaxies (ULIRGs).

Spectro-polarimetry revealed the rest-frame ultraviolet to be $\sim$28% polarized as well as the presence of broad ultraviolet lines (Goodrich et al. 1996), providing strong evidence that this was the reflected light (presumably off dust clouds associated with the narrow-line region) from an obscured AGN. The model of IRAS 10124 could now conclusively include an active nucleus, however X-ray observations with both the Chandra (Alexander et al. 2005) and XMM-Newton (Iwasawa et al. 2010) space telescopes made low S/N detections, seemingly inconsistent with the powerful AGN suggested by the luminous [O III]λ5007Å line emission strength ($L_{\rm OIII} \sim 2 \times 10^{37}\,\mu^{-1}$ W, Serjeant et al. 1998). This lead to the suggestion that this is a Compton thick object (i.e. $N_{\rm H} > \sigma_{\rm T}^{-1} \sim 1.5 \times 10^{24}\,{\rm cm}^{-2}$). The lower than expected X-ray luminosity could also be explained by preferential lensing of the scattering clouds (i.e. the observable hot, ionised medium) due to a suggested offset from the AGN and as a result a larger magnification than that of the AGN. However, Nguyen et al. (1999) use arguments (that are re-investigated in §5) about the smooth polarisation position angle variation along the emission arc in their *HST* ultraviolet map that limits this distance to $\sim$ 40 – 100 pc in the source plane (assuming μ = 50 – 100). The uncertainty in the intrinsic quasar bolometric luminosity at this stage was clearly very large given the suggestions of preferential lensing and/or Compton thick obscuration.

Multiple detections of a large reservoir of molecular gas ($M_{\rm H_2} \sim 10^{11-12}\,\mu^{-1}\,{\rm M}_{\odot}$, Brown & Vanden Bout 1991, Solomon et al. 1992a, Tsuboi & Nakai 1997, Radford et al. 1996) supported previous suggestions that the far-infrared radiation originates from a massive starburst. Conditions of the inter-stellar medium were probed with the detection of higher transition CO lines (6$\rightarrow$5, 7$\rightarrow$6), as well as heavier molecules formed in the denser cores of star forming clouds (e.g. HCN (1$\rightarrow$0), Vanden Bout et al. 2004; C I, Ao et al. 2008). Despite this immense star-formation activity, mid-infrared *Spitzer* spectroscopy did not reveal the strong polycyclic aromatic hydrocarbon (PAH) emission typical of ULIRGs (Teplitz et al., 2006). Furthermore, this same *Spitzer* spectrum showed a 9.7 μm silicate feature in *emission* as opposed to the usual silicate absorption seen towards obscured AGN. These attributes led Teplitz et al. (2006) to conclude that IRAS FSC10214 is unlike any ULIRGs or AGN in the local Universe. They proposed that the AGN is preferentially magnified and therefore masks the dominant starburst activity. The very first publication on IRAS

10214 (Rowan-Robinson et al., 1991) questioned the source of its enormous luminosity: massive, dust-enshrouded star formation, or a buried active galactic nucleus? Clearly the relative contribution of these two components remains an outstanding question in the case of IRAS 10214, as well as a major challenge in current galaxy evolution models.

1.5 Adopted Cosmology

In this thesis, a flat ΛCDM cosmology is assumed with parameter values $\Omega_{\rm M} = 0.3$, $\Omega_\Lambda = 0.7$, $\Omega_{\rm k} = 0$ which refer to the present epoch's matter, dark/vacuum, and curvature energy densities respectively; and $h = 0.71$ where h is the Hubble constant scaled to 100 $\rm km\,s^{-1}\,Mpc^{-1}$ (Spergel et al., 2007).

1.6 Thesis Summary

This thesis describes the multi-wavelength observations and gravitational lens modelling of the high-redshift, strongly-lensed, starburst/AGN galaxy, IRAS FSC10214+4724. Summaries of each chapter are outlined below.

Chapter 2 gives a brief overview of gravitational lensing theory followed by a description of the purpose-built Bayesian Markov Chain Monte Carlo algorithm. The results of three lens models are reported.

Chapter 3 details the resolved radio and *HST* observations of IRAS 10214.

Chapter 4 presents spatially and spectrally resolved CO $(1\rightarrow0)$ observations of IRAS 10214 using the *Jansky VLA*. We invert individual channel maps into the source plane and explore the evidence for a regularly rotating cold molecular disk. Furthermore, we explore two LVG models based on the spatial information from the CO $(1\rightarrow0)$ map; calculate the CO-to-H_2 conversion factor through dynamical mass estimates; and present evidence for an extended, cold gas reservoir.

Chapter 5 reports results from IRAS 12014 VLBI observations and investigates the scale of preferential lensing in the system. We also estimate the black hole mass as well as the bolometric luminosity of the obscured quasar using five methods from mid-IR to X-ray wavelengths.

Chapter 6 explores the properties of the host galaxy in IRAS 10214 based on a deep near-IR *HST* observation and makes an estimate of the black hole-spheroid mass ratio.

Chapter 7 makes qualitative conclusions of the thesis and outlines the progress to be made with upcoming observations.

Appendix A gives a brief overview of additional projects undertaken during the course of this D.Phil.

CHAPTER 2

GRAVITATIONAL LENS MODELLING

R.P. Deane, S. Rawlings, P.J. Marshall, I. Heywood, H.-R. Klöckner, K. Grainge, T. Mauch, S. Serjeant

Section 3 in *"The preferentially magnified active nucleus in IRAS F10214+47: I. Lens model and spatially resolved radio emission"*

MNRAS, submitted

2.1 Basic Equations

Gravitational lensing occurs as a result of the apparent deflection of light between the astrophysical source and observer by an intervening mass that curves the local spacetime. If we are in the regime where the lens can be considered to have negligible thickness compared to the angular diameter distances between source and observer, ($D_{\rm s}$), lens and observer ($D_{\rm l}$), and lens and source ($D_{\rm ls}$); then the lensing geometry can be described in two dimensions and is quantified as angular position vectors on the sky. This reduces to the mapping of a point on the source plane β to a point on the image plane θ through

$$\beta \;=\; \theta - \alpha(\theta) \;=\; \theta - \nabla\psi(\theta), \tag{2.1}$$

where $\vec{\alpha}$ is the deflection angle which depends on the total lens gravitational potential ψ. The angular mass surface density, $\Sigma(\theta)$ is related to the projected lensing potential, through the Poisson equation

$$\Sigma(\theta) \quad = \quad \frac{c^2}{8\pi \mathrm{G}} \frac{D_{\mathrm{l}} D_{\mathrm{s}}}{D_{ls}} \nabla^2 \psi(\theta). \tag{2.2}$$

The mass surface density is modelled as a radial density profile described in the form of a singular isothermal ellipsoid potential (see Kochanek 1991; Kormann et al. 1994) which has the same potential profile of the Singular Isothermal Sphere (SIS), however the radius r is replaced with

$$r' \quad = \quad \sqrt{(qx^2 + y^2)}, \tag{2.3}$$

where the source plane position $\theta \,=\, (r', \phi)$ in angular coordinates, q is the semi-minor to semi-major axis ratio, ε is the ellipticity parameter (ε = 1 - q), (x, y) are the source plane co-ordinates rotated through the position angle ϕ_{PA} of the major axis. We note that potentials with high ellipticity ($\varepsilon \gtrsim$ 0.5) can have unphysical dumbell-shaped iso-density contours. We shall see that the best-fit ellipticity in this work is significantly less than this value for this to be a concern.

Given the singular isothermal ellipsoid assumption, we can equate θ_E to a 1D velocity dispersion σ_v via:

$$\sigma_v^2 = \frac{c^2}{4\pi} \frac{D_{\mathrm{s}}}{D_{\mathrm{d}s}} \theta_{\mathrm{E}}, \tag{2.4}$$

where θ_{E} is the Einstein radius (or asymptotic critical radius) for a circularly symmetric lens.

So under these assumptions, given an ellipticity, position angle and θ_E (or σ_v) we can calculate the mapping from source plane to image plane. It is useful to also define the convergence

$$\kappa(\theta) \quad = \quad \frac{\Sigma(D_{\mathrm{d}} \theta)}{\Sigma_{\mathrm{cr}}}, \tag{2.5}$$

where $\Sigma_{\mathrm{cr}} = \frac{c^2 D_{\mathrm{s}}}{4\pi \mathrm{G} D_{\mathrm{ds}} D_{\mathrm{d}}}$. The resultant magnification is given by

$$\mu \quad = \quad [(1-\kappa)^2 - \gamma_1^2 - \gamma_2^2]^{-1}, \tag{2.6}$$

where γ is the shear which is comprised of a real (γ_1) and imaginary (γ_2) component, $\gamma = \sqrt{\gamma_1^2 + \gamma_2^2}$. The critical line is defined where $\mu \to \infty$. If multiple mass components are added, their respective convergence and shear are simply added to one another in Eq. 2.6

$$\begin{aligned} \mu_{\rm multi} \quad = \quad & \left[\{1-(\kappa_a+\kappa_b+...+\kappa_z)\}^2 - (\gamma_{1,a}+\gamma_{1,b}+...+\gamma_{1,z})^2 \right. \\ & \left. -(\gamma_{2,a}+\gamma_{2,b}+...+\gamma_{2,z})^2\right]^{-1}, \end{aligned} \tag{2.7}$$

where the subscripts {a,b,...,z} represent multiple individual lenses. With a basic description of model parameters required, we now seek to estimate the posterior probability distribution function (PDF) of each lens model parameter through a Markov Chain Monte Carlo (MCMC) sampler.

2.1.1 Data

HST F814W

IRAS 10214 was observed with the WFPC2 F814W filter during two orbits on 10 December 1994. This rest-frame ultraviolet map was the first conclusive evidence that IRAS 10214 is indeed gravitationally lensed. All data were processed through the Canadian Astronomy Data Centre (CADC) *HST* pipeline[1]. The morphology (see Fig. 2.1) shows a clear ~1 arcsec long arc and a low S/N detection of the counter-image. The lensing galaxy has been subtracted using a GALFIT 3 (Peng et al., 2010) Sersic fit. The integrated arc/counter-image flux density ratio is $\breve{\mu} \sim 75 \pm 25$. The observations, derived properties and lens modelling are fully described in Eisenhardt et al. (1996). Two key attributes of this map are accurate point spread function (PSF) characterisation and astrometry. The PSF FWHM is ~100 mas as derived from the 'Tiny Tim' *HST* software package using a *K*-star source colour since an accurate empirical estimate was not possible. This is fully described in Eisenhardt et al. 1996 and is consistent with two stars in the

---

[1] http://cadcwww.dao.nrc.ca/hst

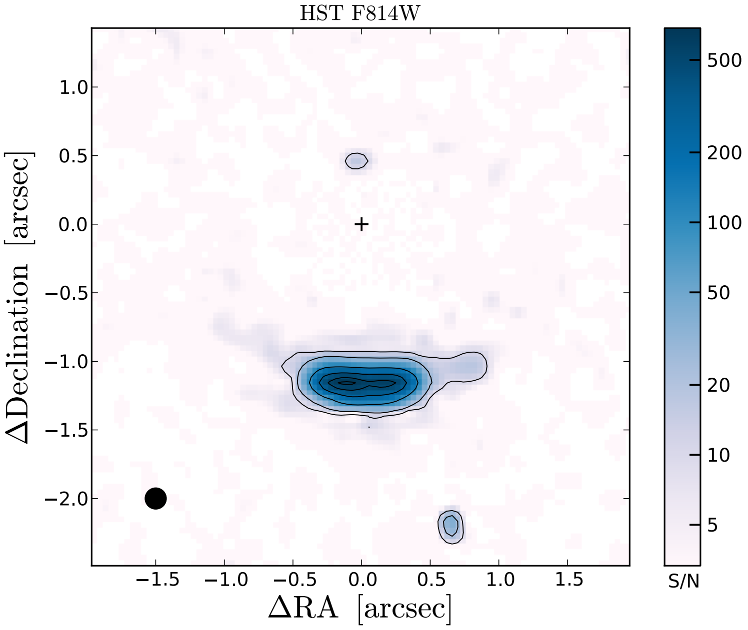

Figure 2.1: *HST* F814W map with counter-image and arc. The integrated arc/counter-image flux density ratio is $\breve{\mu} \sim 75 \pm 25$. The *HST* PSF through this filter has a FWHM of ~100 mas, as detailed in (Eisenhardt et al., 1996) and is indicated in the lower left of the frame. Note that the lens has been fit using GALFIT and removed from this image.

field, one of which is saturated and the other too weak for accurate PSF estimation. The astrometry is in agreement with determinations from Nguyen et al. (1999); Eisenhardt et al. (1996); Evans et al. (1999) and Simpson et al. (2012, in prep.) to within $\Delta\theta < 10$ mas.

HST **F160W**

IRAS 10214 was observed with the NICMOS camera 2 on 22 March 2004 within a single orbit under Proposal ID 09744 (PI: Kochanek). The wide band filter F160W was used, resulting in a PSF FWHM of ~0.15 arcsec. The map (Fig. 2.2) shows the arc structure, the lens as well as a counter-image to the north of the lens, as well as all the nearby, line-of-sight galaxies (components 3,4,6). The arc shows two clear components: an extensive, faint arc, as well as a larger, more dominant component (see an enlarged version later in Fig. 6.1). We attribute the latter to the scattered quasar light (that dominates the *HST* F814W map) as well as a more extended, lower magnification host galaxy component. This is supported by the global SED as well as the 4000 Å break first identified by Lacy et al. (1998). The detection of the counter-image has higher significance than the *HST* F814W map and an arc/counter-image flux ratio $\breve{\mu} = 69 \pm 7$. Despite

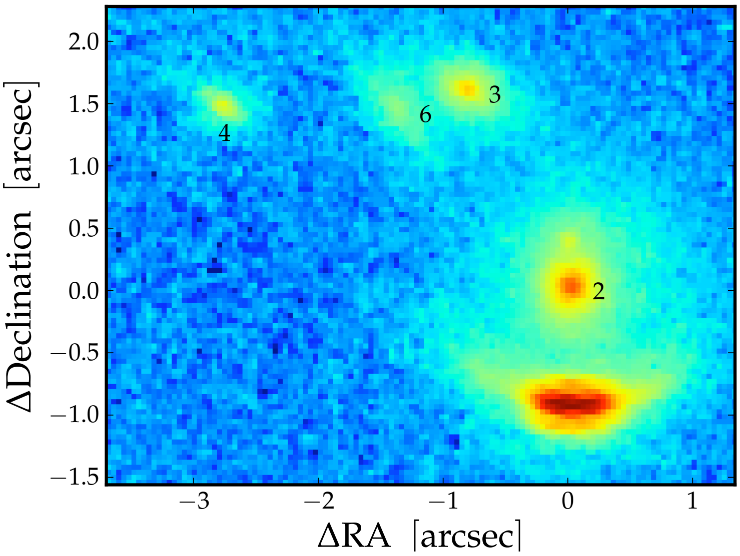

Figure 2.2: Larger field of view of the IRAS 10214 region (*HST* F160W map) showing three satellite galaxies to the north-east. The IRAS 10214 arc can be seen south of the main lensing galaxy (component 2).

this higher S/N we do not use the *HST* F160W map for our lens modelling since it clearly has a complex source structure. For the purposes of this work, the larger field-of-view map is used to investigate the lensing potential of nearby galaxies (§2.1.7) and to determine the ellipticity and position angle priors for main lens (component 2). The source plane properties of the *HST* F160W map will be shown in Chapter 6. All data were processed through the CADC *HST* pipeline and astrometry was corrected to be consistent with Nguyen et al. (1999), Eisenhardt et al. (1996), Evans et al. (1999) and Simpson et al. (2012, in prep.), as in the case of the *HST* F814W map.

2.1.2 Lens Model Derivation

We derive the lens model parameters, given the data which are the *HST* F814W map pixel values presented in Fig. 2.1. This is not only a very high S/N map but is at a wavelength we believe to be dominated by a single physical source (i.e. the emission is dominated by scattered QSO light, despite showing some structure along the arc) and therefore likely to have a simpler intrinsic source structure than a filter with both stellar and QSO components. We predict data pixel values which are derived by ray-tracing trial source models into the image plane based on a trial lens model. We have developed software that implements a MCMC routine to compare ray-traced trial models to the data and so sample the posterior probability distribution function (PDF) of all free parameters. The posterior PDF is defined by Bayes' Theorem

$$Pr(x|d,H) = \frac{Pr(d|x,H)\,Pr(x|H)}{Pr(d|H)}, \tag{2.8}$$

where $Pr(d|x,H)$ is the likelihood and $Pr(x|H)$ is the product of our informative priors to be described below. $Pr(d|H)$ is known as the *evidence* which normalises the posterior. In our MCMC routine we sample the unnormalised posterior distribution. All ray-tracing from source to image plane is performed by routines in the software package GLAMROC[2]. These ray-tracing routines adaptively increase the spatial resolution (i.e. the number of pixels) as a function of the local magnification, the thresholds of which can be set by the user. This improves the accuracy (and/or computational efficiency) when modeling lensed sources that have close proximity to the caustic. This software is especially powerful in the cusp-caustic lens configuration as in the case of IRAS 10214. Computational efficiency limits the source plane resolution, however the magnification around the cusp can change dramatically inside a single source plane pixel. Therefore, GLAMROC alleviates the computational challenge by enabling higher resolution in regions that exceed a defined magnification. This sub-division of source plane pixels can be repeated an arbitrary number of times.

Before describing the MCMC routine in further detail, we first introduce the existing IRAS 10214 lens model and describe the observables on which we base our informative priors. The most sophisticated IRAS 10214 lens model in the literature is that derived by Eisenhardt et al. (1996). They use a least-squared approach, minimising the distance between the model and the brightest 96 pixels in the arc as well as the brightest pixel in the counter-image, using the *HST* F814W data. They assume a uniform (constant surface brightness) circular disk source model and found a best-fit isothermal ellipsoid mass distribution ellipticity of $\varepsilon = 0.3$. The observed stellar ellipticity of the lensing galaxy is $\varepsilon \sim 0.16$-0.2 for the *HST* 0.8, 1.1 and 1.6 μm images. In the Sloan Lens ACS Survey (SLACS), Koopmans et al. (2006) model 15 massive early-type field galaxies with a singular isothermal ellipsoid (SIE). They find that the stars and dark matter have highly correlated position angles (*PA*) and ellipticities (ε). The average ratio of dark matter to stellar ellipticity is $\langle q_{\rm SIE}/q_* \rangle = 0.99 \pm 0.11$, and the average difference between the derived dark matter *PA* and stellar *PA* is $\langle \Delta PA \rangle = 0^\circ \pm 10^\circ$, the uncertainties indicate the total scatter σ, not $\sigma/\sqrt{N}$. Leveraging off this evidence

---

[2] Gravitational Lens Adaptive Mesh Raytracing of Catastrophes, see http://kipac.stanford.edu/collab/research/lensing/glamroc

that baryons in lensing galaxies broadly follow the dark matter potential, we select an observationally motivated approach and set lens model parameter priors based on the baryon distribution. The *HST* F160W observation offers two major advantages in the gravitational lensing analysis of IRAS 10214.

1. **Sensitivity:** the *HST* F160W map has roughly a factor of 2 better S/N than the *HST* F814W map.
2. **Dark Matter Tracer:** the foreground lens galaxy is observed at rest-frame *R*-band tracing the older, more virialised stellar population which should, in principle, better sample the dark matter potential.

We therefore use this *HST* F160W map to set the lens model priors. We derive the *mean* of these position angle and ellipticity priors using GALFIT two-dimensional Sersic fits. GALFIT is run for 5×10^4 Monte Carlo iterations with each initial parameter randomly varied by an order of magnitude (or between 0.5-8 for the Sersic index, 0–180° for the position angle). We find an ellipticity $\varepsilon = 0.20 \pm^{0.01}_{0.004}$ at a position angle $\theta_{\rm PA}$ = -4.8° ± 0.9° (East of North) and a Sersic index[3] n = 2.65 ±0.23, in the range between that measured for typical ellipticals ($n = 4$) and disk galaxies ($n = 1$).

These results are used to set Gaussian mass distribution priors of $\varepsilon_{\rm prior}$ = 0.2 ±0.4 and $PA_{\rm prior}$ = -4.8 ±10° for the ellipticity and position angle respectively. Note that for an SIE, the projected mass density ellipticity $\varepsilon_{\rm M} \approx 3 \times \varepsilon_{\Phi}$, if the potential ellipticity $\varepsilon_{\Phi} << 1$ (Golse & Kneib, 2002). The width of these priors are determined from the rms scatter in the Koopmans et al. (2006) sample, however we broaden the ellipticity prior by a factor of 5 in view of the best-fit ellipticity derived by Eisenhardt et al. (1996). Furthermore, this is a higher redshift lens ($z = 0.893$) than the $z \sim 0.1-0.3$ SLACS lenses, and therefore would be less virialised from a statistical viewpoint. This is to say that given two elliptical lens galaxies, one at $z \sim 0.1$ and the other at $z \sim 0.9$, there is a higher probability that the former is virialised as a result of hierarchal structure formation (e.g. Springel et al., 2005) and the difference in mergers rates at these two epochs (e.g. Le Fèvre et al., 2000). We assume Gaussian, spherically symmetric source profiles. The Gaussian profile assumption was later relaxed, however, other Sersic indices did not improve the residuals. Following previous authors (e.g. Koopmans et al., 2006; Kormann et al., 1994) we assume a singular isothermal ellipsoidal potential (i.e. $\Phi \propto r^{-2}$ where Φ is the potential and r is the radius). Deviation from this assumed density profile is likely

---

[3] Note that the lens is simultaneously fit with a Sersic component and an unresolved core component. The luminosity of this core component contributes ~ 0.4% of the total and therefore does not make a significant contribution to the mass within the Einstein radius.

our largest source of systematic error which is quantified in §2.1.7. Although GLAMROC is able to model potentials with Sersic profiles, our attempts to free the inner density slope (assuming the *HST* F814W data) did not yield successful results.

The lens fitting is first performed with one SIE lens in a coarse grid mode where the reduced-χ^2 (denoted χ^2_ν for the remainder of this thesis) is recorded for the full range of plausible lens and source parameters. These results are used solely to make a rough approximation of the macro-lensing model. They are combined with an approximate measurement of the arc curvature, as well as the Eisenhardt et al. (1996) modelling results, to derive an Einstein radius Gaussian prior of $\theta_{\rm E} = 0.85 \pm 0.1$ arcsec. The source-plane centroid and scale radius have uniform (flat) priors.

With priors in place, the algorithm is run. The MCMC routine employs the Metropolis-Hastings algorithm which compares the posterior probability of the current model with a candidate model. We employ a Gaussian proposal distribution which is tuned to have an acceptance rate of 20% of all proposal steps that result in a lower posterior probability, which allows local minima to be avoided. The full routine is set to run for 5×10^5 iterations, where convergence occurs after $\sim 1 \times 10^5$ iterations (i.e. sub-chains of this length exhibit equivalent statistics). A typical ‘burn-in’[4] period of $\sim 2 \times 10^4$ iterations is observed.

The MCMC routine must be run in uncorrelated parameter space to achieve convergence within a reasonable time-scale ($<$ 24 hrs on a dual core 2.8 GHz machine). We derive the parameter vector covariance matrix by performing a long (10^6 iteration) run in correlated space. We then perform a principal component analysis (PCA) to transform the parameter vector into uncorrelated space where all trial steps are made. We use all Eigenvectors and Eigenvalues in the PCA analysis since the added computational time is negligible compared to the ray-tracing calculations and disk read/write speed.

2.1.3 Lens Models

The lens model derivation has followed three stages:

1. Lens Model 0: a single main lens (SIE);
2. Lens Model A: main lens (SIE) + an additional neighbouring mass (SIS)

---

[4] The burn-in period refers to the number of MCMC iterations discarded before the overall statistics of the chain are determined. This is done because the algorithm takes an initial period to sufficiently explore the posterior, find the parameter sub-space of interest and exhibit statistics that are independent of the initial parameter vector.

3. Lens Model B: main lens (SIE) with free position + SIS neighbour.

These three stages are motivated by the counter-image positional offset, the achieved χ^2_ν values, as well as a measurement of the centre of arc curvature from both *HST* F160W and *HST* F814W maps. All of these are described in more detail below. Each stage has two runs, the first is performed using the process of 'annealing' where the Gaussian proposal distribution FWHM decreases as a function of iteration number. This allows the full parameter space to be explored efficiently and is also used to determine the covariance matrix. Once the minima are found, the chain is re-run in uncorrelated space without annealing, using Gaussian proposal distributions, the variance of which are proportional to the corresponding Eigenvalues. The second run sets the initial parameter values to the best-fit of the first run.

Lens Model 0: Single SIE Lens

This model has a total of 6 parameters: the unlensed source position (RA, Dec), source scale radius (r_s), Einstein radius (θ_E), lensing potential ellipticity (ε), and its position angle (PA). The results of Lens Model 0 are surprisingly good (${\chi^2}_\nu \sim 32$) given the simplicity of the lens and source models. A single Gaussian source component models the majority of the flux in the arc, however there is a 150 mas North-East offset between the data and model counter-images. An analysis of all the individual model frames from the MCMC chain shows that there is no place within the parameter space that yields co-spatial data and model counter-images while simultaneously maintaining a reasonably symmetric arc. We disregard this lens model, since it clearly fails to reproduce the counter-image position not only in the best-fit model, but in all models in the allowable parameter space. Shear is a parameter that is routinely added in lens modelling and often leads to a dramatic improvement to the χ^2_ν, particularly for point sources. Shear was added to the lens model (requiring two additional two parameters: γ_1, γ_2) and marginally decreased the distance between the model and data counter-image to ~ 120 mas, however it distorts the extended main arc, resulting in a χ^2_ν that is almost unchanged. The best-fit shear magnitude was $\log_{10}(|\gamma|) = -1.94 \pm 0.55$ with a position angle towards component 3 ($\theta_\gamma \sim 30^\circ \pm 25^\circ$), as would be expected. This suggests that the inclusion of shear is not optimal for the extended emission present in the *HST* F814W map, unlike the case of point sources.

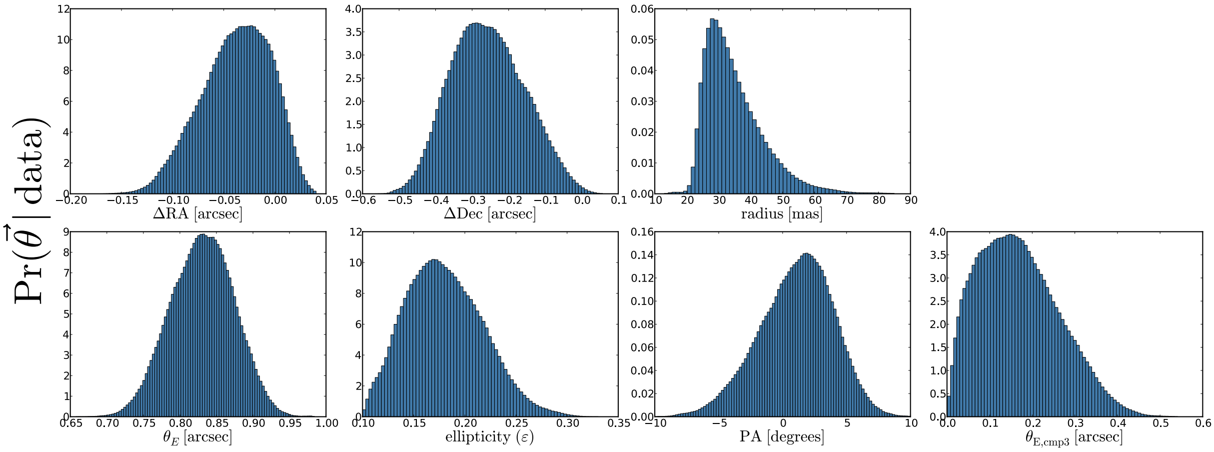

Figure 2.3: The 7 histograms show the normalised, MCMC derived samples of the source (RA, Dec, scale radius) and lens parameters (Einstein radius, lens ellipticity, lens position angle, component 3 SIS Einstein radius), given the *HST* F814W data.

Lens Model A: SIE + satellite SIS

To solve the counter-image position discrepancy encountered in Lens Model 0, we introduce an additional parameter in Lens Model A which comprises of the main lens SIE potential as well as a Singular Isothermal Sphere (SIS) potential to account for the influence for the nearby galaxy which is $\Delta\theta \sim$2.2 arcsec NNE from the primary lensing galaxy (component 3 in Fig. 2.7). A broad Gaussian prior PDF is adopted for the SIS velocity dispersion, based on the Faber-Jackson relation (Faber & Jackson, 1976). The resultant Gaussian prior of the isothermal velocity dispersion has a mean σ_v = 160 km s^{-1} with a FWHM = 100 km s^{-1} at a photometrically determined redshift of z = 0.782 (Simpson et al. 2012, in prep.). Note that the mean of this prior is likely an over-estimate since closer inspection of the galaxy shows an slightly inclined morphology more representative of an S0 galaxy. A Faber-Jackson estimate of the stellar velocity dispersion based on the K-band integrated flux ratio of component 2 and 3 (and the derived component 2 isothermal velocity dispersion) would result in an over-estimate of the component 3 mass since S0 galaxies have systematically lower M/L_B ratios than ellipticals (e.g. Faber & Gallagher, 1979). In addition, the photometrically derived redshift of component 3 ($z = 0.782$) is essentially the most favourable lensing configuration for a source at redshift $z = 2.3$ (due to their relative angular diameter distances). We therefore expect the mean of the component 3 isothermal velocity dispersion prior to be exaggerated, however a suitably broad prior alleviates this concern.

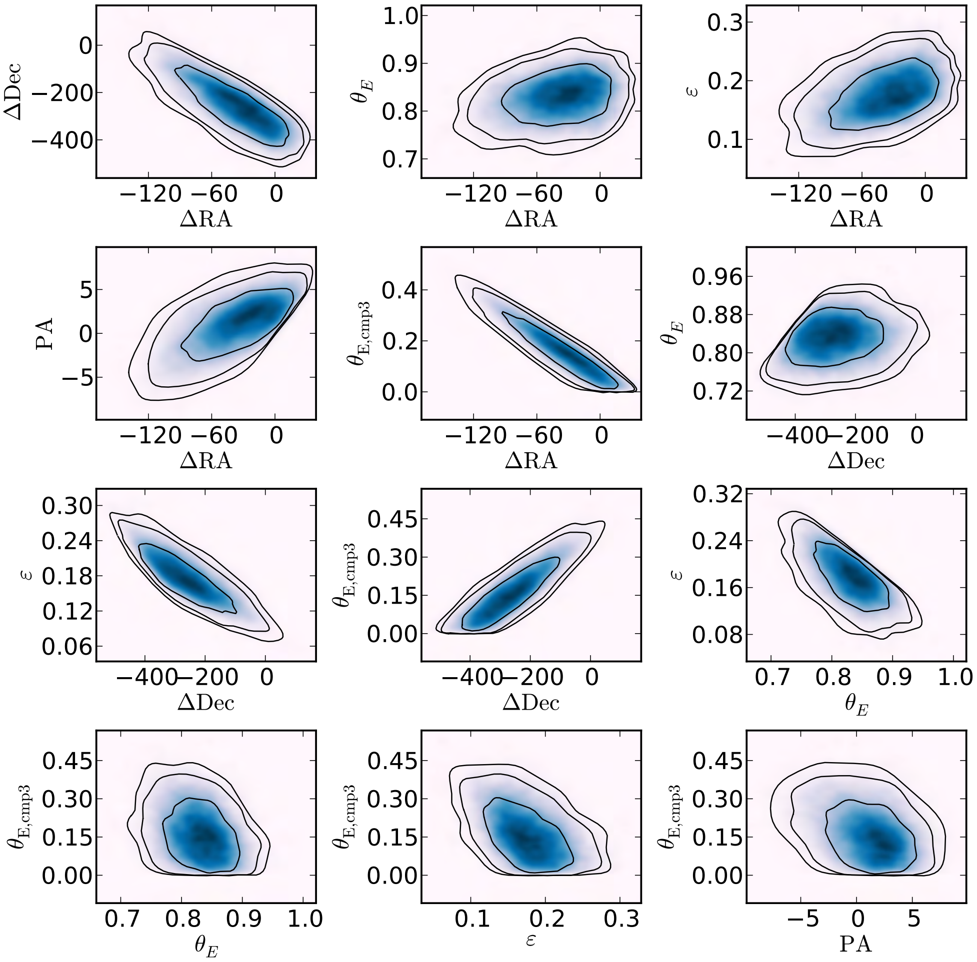

Figure 2.4: The 12 contours plots show a selected subset of the total of 21 2D marginalised PDFs of the source plane and lens parameters given the *HST* F814W data. The selected two-dimensional posterior PDFs are those that showed any sign of degeneracy between the two parameters. The contours show the 68%, 95% and 99% confidence levels. Note that plots are zoomed in to show the degeneracies clearer, in all cases the allowable parameter space is beyond the plot boundaries.

This results in a model with 7 free parameters with physically motivated priors. The MCMC algorithm is tuned as described previously and run for 5×10^5 iterations. The one-dimensional marginalised posterior PDFs of all parameters are reasonably approximated by Gaussian distributions, which are plotted in Fig. 2.3 and listed in Table 2.2. While the average $\chi^2_\nu = 30$ values are roughly the same for Lens Model A compared to Lens Model 0, the major difference is that the counter-image position has a far superior fit. There is still a $\sim 20-30$ mas southern offset between data and the model generated with the mean of all parameter posterior PDFs. However, it is clear that the additional SIS parameter results in putting the model counter-images in regions consistent with the data counter-image, justifying the additional model complexity. Further complexity could be added in the form of an external shear parameter, however we do not feel this is entirely necessary for our primary objectives of modelling dominant emission regions and their relative magnification, source plane position and size.

The model makes two improvements on the Eisenhardt et al. (1996) lens model (apart from estimating uncertainties). Firstly, we use a more physical source model profile (Gaussian) than the uniform, constant surface brightness circular disk they employed. Secondly, we free the component 3 Einstein radius which they fixed to $\theta_{\rm E,cmp3} = 0.6$ arcsec, derived from the *K*-band flux ratio of component 2 and 3 (which they assumed to both be at a redshift of $z = 0.9$). The derived Einstein radius of the component 3 galaxy greatly affects the component 2 Einstein radius and ellipticity, particularly since the redshift is not known. As a result, fixing the component 3 Einstein radius effectively rules out parts of the main lens parameter space. Our lens model has therefore explored a more extensive parameter space in its derivation.

Lens Model B: SIE (free centroid) + satellite SIS

This model is identical to Lens Model A (1 SIE, 1 SIS) however the main lens (SIE) potential centroid is allowed to vary, whereas before it was fixed to the *HST* F160W map component 2 Sersic fit centroid. This model therefore has a total of 9 parameters. Varying the potential's centroid is primarily motivated by the Eisenhardt et al. (1996) comment that 'The center of curvature of the arc was fitted and found to be 0.12" west-northwest of the center of component 2'. The two additional parameters ($\Delta Lens RA$ and Dec) are assigned narrow Gaussian priors ($\pi(\theta) = 0.0 \pm 0.1$ arcsec). The algorithm is then run in the precisely the same manner as before, yielding some evidence for an offset between the stellar and lensing potential centroids. The derived values are listed in Table 2.2, and the fitted RA and Dec offsets are plotted in Fig. 2.5. This plot shows that the enforced prior strongly influences the $\Delta Lens\,Dec$ posterior PDF, however if the prior is broadened, the MCMC algorithm does not converge. For the sake of brevity, the term ‘centroid offset’ is referred to as the offset between any given component and the fixed lens potential centroid from Lens Model A. Again, the latter is derived from a Sersic fit to the *HST* F160W map of component 2 and has co-ordinates (0,0) in all maps presented in this work.

Lens Model B yields an average $\chi^2_\nu = 23$ that is 30% lower than achieved by Lens Model A. Furthermore, it results in a component 2 lens potential ellipticity and position angle more closely aligned with the stellar distribution. As we will see in §2.1.6, the resultant component 3 mass and mass-to-light ratios are arguably more probable. The MCMC-derived centroid offset is broadly consistent with the curvature fitted value reported in Eisenhardt et al. (1996). We repeat the curvature fitting here using two techniques to check consistency: a least-squares approach and an orthogonal distance regression algorithm. Both approaches yield the same results. The data are the pixel co-ordinates and the distance minimisation algorithm assigns the statistical weighting to different co-ordinate pairs by their normalised flux density. The fit is almost entirely insensitive to S/N clips and weighting schemes and both the *HST* F160W and *HST* F814W maps yield consistent fits, however the centre (black diamond in Fig.2.5) is not consistent with the Eisenhardt et al. (1996) fit (blue dot).

The lowest χ^2_ν colour-scale tier in Fig. 2.5 clearly demonstrates that the adopted lens potential centroid (0,0) is not consistent with the residuals minima, however the MCMC-derived centroid (red cross) and Eisenhardt et al. (1996) estimate (blue dot) are. There are two more intriguing aspects of the data that are relevant. Firstly, there is some low level *MERLIN* 1.7 GHz emission consistent with lens emission (as discussed in §3.1.1). The peak of this ‘lens emission’ is ~ 0.2 arcsec north-west of fixed lens centroid and indicated by a red dot. Secondly, Sersic modelling of the *HST* F160W lens emission reveals a distinct core that is offset from the Sersic component centroid. This component is assumed to be unresolved and so is modelled with a 0.1 arcsec PSF profile and has a fitted centroid ~ 0.125 arcsec east of the fixed potential centroid and is indicated on the map with an orange dot.

Based on the results above, we select Lens Model A for the remainder of this thesis. The χ^2_ν values from all three models are summarized in Table 2.1. While some evidence exists for offset baryon and

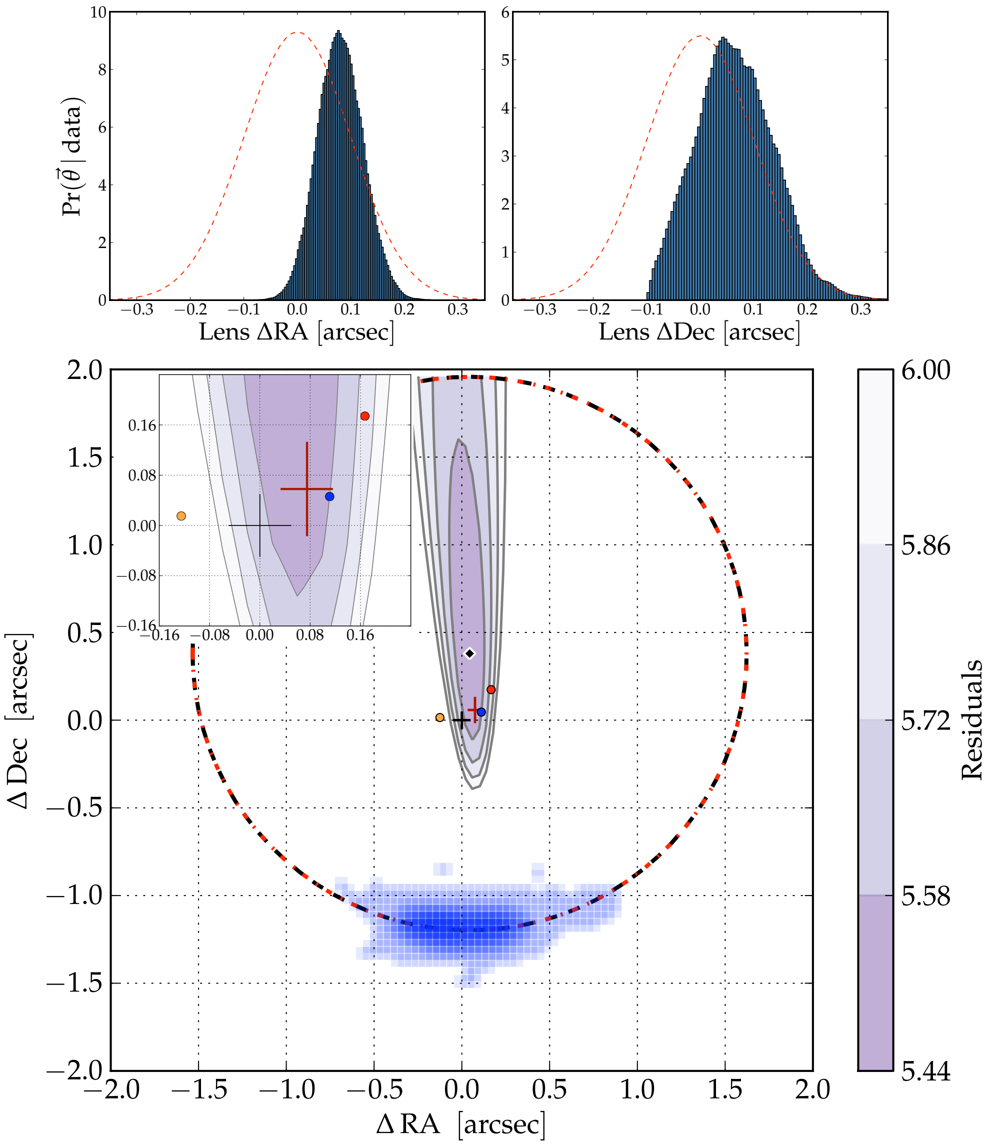

Figure 2.5: **Top:** Posterior PDFs of the lens potential centroid from Lens Model B. Over-plotted in red dashed lines are the assumed priors. **Bottom:** *HST* F814W curvature fit using both least squares (red dot-dashed circle) and orthogonal distance regression (black dashed circle) algorithms with the centre shown with a black diamond. The colour-scale shows the resulting χ^2_ν residuals, which are generated by minimising the sum of the square of the distance (units: pixels) between each pixel and a circle. The inset is a zoomed in view of the *HST* F160W Sersic fit centroid (black cross); the Lens Model B best-fit lens potential centroid (red cross); the Eisenhardt et al. (1996) *HST* F814W curvature fit (blue dot); the *MERLIN* 1.7 GHz lens emission peak (red dot); and the distinct core seen in the residuals of the *HST* F160W Sersic fit (orange dot). Note the red cross represents the MCMC-derived uncertainty, however the black cross is purely illustrative, with a size >> 10 times the formal Sersic fitting uncertainty.

Model	Number of parameters	χ_ν^2	Notes
Lens Model 0	6	32.3	SIE main lens
Lens Model A	7	29.7	SIE main lens + SIS neighbour
Lens Model B	9	23.4	SIE main lens (free centroid) + SIS neighbour

Table 2.1: Resultant mean χ_ν^2 values from Lens Model 0, A and B.

lensing potential centroids, it does not appear convincing enough to add the complexity to the model. We therefore continue with Lens Model A, however will later derive the source magnifications and source plane parameters of both models to demonstrate the systematic uncertainties of this assumption. We set the lens parameters (component 2 Einstein radius, lens ellipticity and lens position angle; component 3 Einstein radius) to the mean of these 1D distributions for all subsequent modelling in this work. These fixed values are listed in Table 2.2.

Finally, a lens modelling routine with a more flexible, pixelated source model (as performed in e.g. Warren & Dye, 2003; Vegetti & Koopmans, 2009; Suyu et al., 2009) was attempted but is currently computationally limited and is the topic of future work following optimisation of the source code.

2.1.4 Source Plane Modelling of IRAS 10214

The same lens modelling procedure is now performed on the two resolved radio maps, and once again for the *HST* F814W map. However, the lens model is now fixed to the Lens Model A values in Table 2.2, given the S/N of the radio data. We note that noise in the radio interferometric data includes correlated components, but we ignore this due to its low level and the dramatic gain in computational efficiency achieved by not performing the χ_ν^2 calculations in Fourier space[5]. In holding the lens model constant, there are three free parameters in all fits: the source's centroid coordinates (*RA*, *Dec*) and scale radius r_s. Uniform priors are assumed for these three parameters. Once again we assume Gaussian, spherically symmetric source profiles.

Our primary aim here is to place constraints on the relative source-plane properties of the three maps shown in Fig. 3.1, using as few free parameters as possible. It is for this reason and the low S/N of the radio data that we assume that each component is modelled by a simple, spherically symmetric Gaussian profile. This results in large χ_ν^2 values for all models ($\chi_\nu^2 \sim 23 - 32$), since high redshift galaxies are observed to

---

[5] We note that a more sophisticated treatment of lens modelling, given interferometric data, allows a direct comparison with the measured visibilities and has the advantage of uncorrelated noise (see Wucknitz, 2004).

Parameter	**Prior**	**Lens Model A**	**68% CL**	**Lens Model B**	**68% CL**	**Measured**†	**Eis96**
x	–	-0.025”	± 0.037”	-0.186”	± 0.035”	–	n/a
y	–	-0.269”	± 0.11”	-0.0857”	± 0.095”	–	n/a
r_{s}	–	0.028”	$\pm^{0.009''}_{0.006''}$	0.031”	$\pm^{0.012''}_{0.009''}$	–	0.010”
θ_{E}	0.85±0.1”	0.827”	±0.044”	0.839”	± 0.040”	–	0.82”
ε	0.07±0.15	0.174	±0.042	0.133	±0.036	0.2	0.12
PA	-4.8° ± 10°	1.9°	±3.0°	-4.1°	±3.7°	-4.8°	-11°
$\theta_{\mathrm{E,cmp3}}$	0.4±0.2”	0.124	± 0.114”	0.379”	± 0.088”	–	0.6” (fixed)
Lens ΔRA	0.0±0.1”	–	–	0.0749”	±0.042”	–	–
Lens ΔDec	0.0±0.1”	–	–	0.058”	±0.074”	–	–

Table 2.2: Lens Model A and B parameters derived from the *HST* F814W map and their 68% confidence levels as determined from their sampled posterior distributions. x, y are the offsets between the source plane position and the *observed* lens centroid; r_s is the source plane scale radius; σ_{v} and $\sigma_{\mathrm{v,cmp3}}$ are the 1D isothermal velocity dispersions for the main lens (component 2) and the line-of-sight galaxy (component 3); ε is the intrinsic potential ellipticity of the main lens; PA is the main lens position angle; $Lens\,\Delta RA, Dec$ is the lens potential offset from the *HST* F160W Sersic fit centroid. The systematic uncertainty is discussed in §2.1.7. The **Prior** column lists the mean of each assigned Gaussian prior and the associated standard deviation. The **Measured** column is based on GALFIT Sersic fits to the *HST* F160W map. The final column (**Eis96**) indicates the derived model values from Eisenhardt et al. (1996). Note that the source plane parameters in Eisenhardt et al. (1996) were not published. We set the lens parameters to the mean of the 1D distributions for all subsequent modelling.
† This is the observed mass distribution ellipticity, as derived from a Sersic fit to component 2 in the *HST* F160W map.

be clumpy, particularly in the ultraviolet (e.g. Le Fèvre et al., 2000). However, our aim is not the perfect reconstruction of the source plane pixels, *but rather the relative source plane configuration and sizes (and uncertainties thereof) of the dominant components of the three different emission sources proposed.*

2.1.5 Relative Absolute Astrometry at Different Wavelengths

While the absolute astrometry can be well defined within a given waveband, the relative offsets between these absolute astrometric reference frames is more challenging to quantify. The primary reasons for this are:

- The emission mechanisms that dominate the received flux at differing wavelengths may be fundamentally different. Therefore, the centroid positions and scales of the emission is not necessarily the same across the full SED of a calibrator source. For example, if a standard mid-IR source is not perfectly co-incident with a well-defined optical source, however is still tied to the known optical position, this will result in some degree of astrometric shear in this region of the mid-IR sky.

- The *HST* absolute astrometric precision is poor in comparison to ground-based measurements, despite the superior angular resolution. As a result, *HST* observations must be made consistent with ground-based observations of the same objects. However, the latter typically have seeing-limited angular resolution. Therefore, the relative astrometric accuracy is typically limited by seeing and the signal-to-noise of sources detected in the sky region of interest.

In this thesis, the primary concern is the correspondence between the radio and optical reference frames. An analysis of this has been performed by Lawrence et al. (1993) who compare the optical and radio positions of 20 compact radio sources in the region around IRAS 10214. They find no significant mean difference, however, they note the error on the mean difference is 0.2 arcsec which we take as the systematic uncertainty in the radio-optical co-ordinate system alignment. Since we use the same data (described in Sec. 3.1.1), and our calibrators (as well as the 8 GHz centroids) are consistent, we assume have an equivalent astrometric matching between radio and optical reference frames. To improve the uncertainties on this measurement, one would need to improve the signal-to-noise of the observations, target more nearby sources, and perhaps employ adaptive optics to improve the optical/NIR angular resolution. However, the latter would further complicate the process since the applied phase corrections compromise the astrometric accuracy, in an analogous way to self-calibration in radio astronomy. In summary, it appears the relative radio-optical astrometry is secure, however systematic distortions may exist at the $\lesssim$200 mas level.

2.1.6 Component 3 Physical Properties

In Fig. 2.6 we show the physical properties of component 3 based on our derived lens models. As stated before, the redshift is photometrically determined yielding large uncertainty in the intrinsic properties. Figure 2.6 (top panel) shows the mass of component 3 (inside the Einstein ring radius) as function of redshift. As can be seen, all three estimates are below M^* ($\sim 10^{11.3}$ M$_\odot$) for the most probable redshift range. The adopted Lens Model A has the lowest mass prediction which is $M_{\rm cmp3} \sim 8 \times 10^9 \,{\rm M}_\odot \ \pm 0.5$ dex inside the Einstein radius of $\theta_{\rm E,cmp3} = 0.12$ arcsec. A consistency check is the derived mass-to-light ratio plotted in Fig. 2.6 (bottom panel). Rest-frame B-band magnitudes for the $z = 0-2$ range were interpolated from a high order polynomial fit to the F555W, F814W, F110W, F145M and F205W *HST* filters. No stellar model can be assumed without a spectroscopic redshift, however the L_B uncertainty is dominated by the lensing model and the not the assumed stellar spectrum. The three models all have plausible M/L_B ratios (2–40) at the photometric redshift. Since this is in the dwarf galaxy regime, direct comparisons with large statistical samples are difficult, however the Lens Model B derived M/L_B appears in the middle of the typical 3-30 range. Although Fig. 2.6 does not rule any of the three Einstein radii out, it does demonstrate that they are all physically plausible values at the photometric redshift.

2.1.7 Systematic Uncertainties

The source of systematic error that is likely to dominate the error budget is the assumption of an isothermal density profile, which implies a fixed inner density power law slope $m = 1$, where m is defined in terms of the Einstein radius following Marshall et al. (2007) who show the convergence to be expressed by,

$$\kappa = \frac{2-m}{2}\left(\frac{\theta_{\rm E}}{\theta}\right)^{m}, \tag{2.9}$$

in a generalised power law form. To quantify to the systematic error associated with this assumption we follow Marshall et al. (2007, Appendix A). They quantify the inferred source size, Ω, that results from small perturbations away from the isothermal logarithmic density slope ($m = 1$). Their detailed appendix relates the inferred source size uncertainty (σ_Ω) to the spread in the logarithmic density slope σ_m. To quantify the latter, these authors use the intrinsic spread of the power law indices fitted in the Koopmans et al. (2006) analysis of 15 early-type galaxies from the SLACS survey. We use the updated work in Koopmans et al. (2009), which uses a larger sample of 58 early-type galaxies and finds an intrinsic spread of $\sigma_m = 0.2$. With σ_m quantified and the Marshall et al. (2007) relation between σ_m and σ_Ω

$$\frac{\sigma_\Omega}{\Omega} = \mu \, \frac{\partial \mu^{-1}}{\partial m}\bigg|_{m=1} \sigma_m \, , \tag{2.10}$$

we find a systematic magnification uncertainty $\sigma_\Omega/\Omega \approx 2\sigma_m$ and so $\sigma_\mu \sim 0.4$. This 40% uncertainty on the total magnification due to the density slope uncertainty is expected to dominate the systematic error budget given a particular lens model.

In principle, one could test our isothermal assumption by comparing the thickness of the arc and the

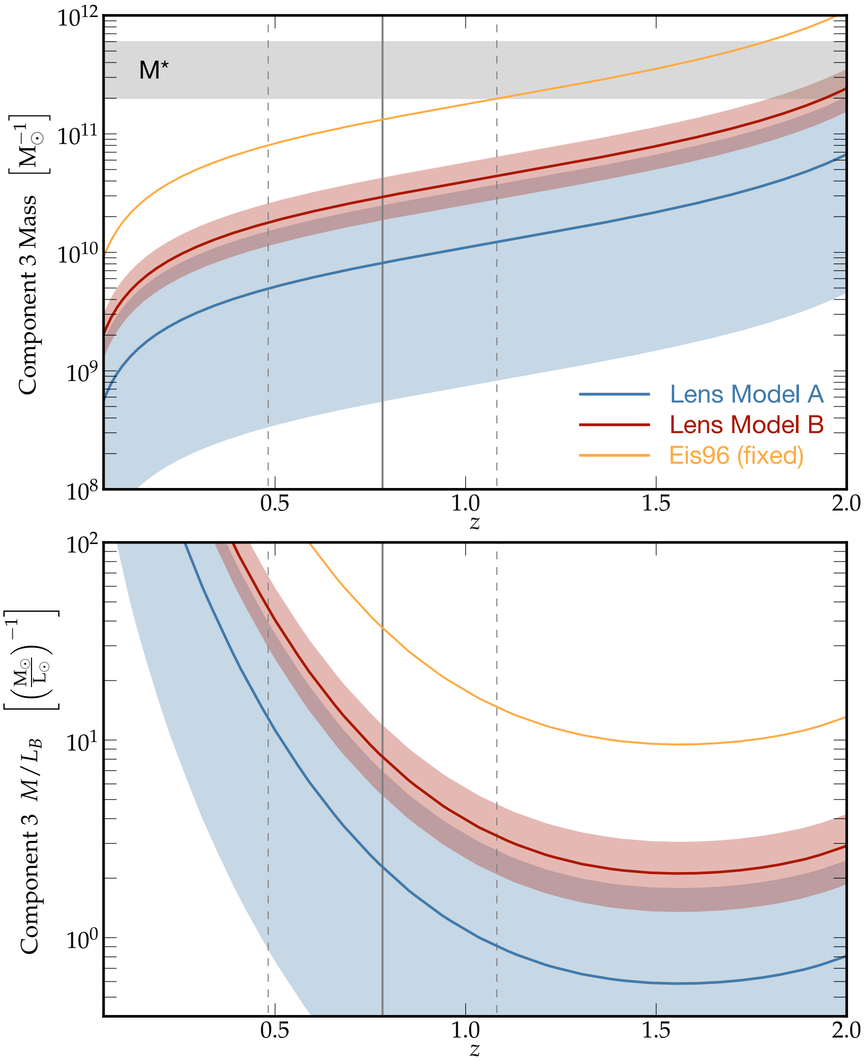

Figure 2.6: **Top panel:** Component 3 mass (with Einstein radius) as a function of redshift, based on the Einstein radii derived in Lens Models A and B (blue and red respectively) shown with their MCMC-derived uncertainties in lower opacity. The orange line represents the fixed Einstein radius assumed in Eisenhardt et al. (1996). The solid grey vertical line indicates the Simpson et al. (2012, in prep.) photometric redshift for component 3, with the rough 68% confidence levels indicated by the dashed grey lines. The grey horizontal bar indicates an M^* galaxy with an assumed mass-to-light ratio of 10-30. The angular diameter distances required are generated with the cosmological parameters listed at the end of Chapter 1. **Bottom panel:** Component 3 mass-to-light (M/L_B) ratio as function of redshift. Colour coding as in the top panel.

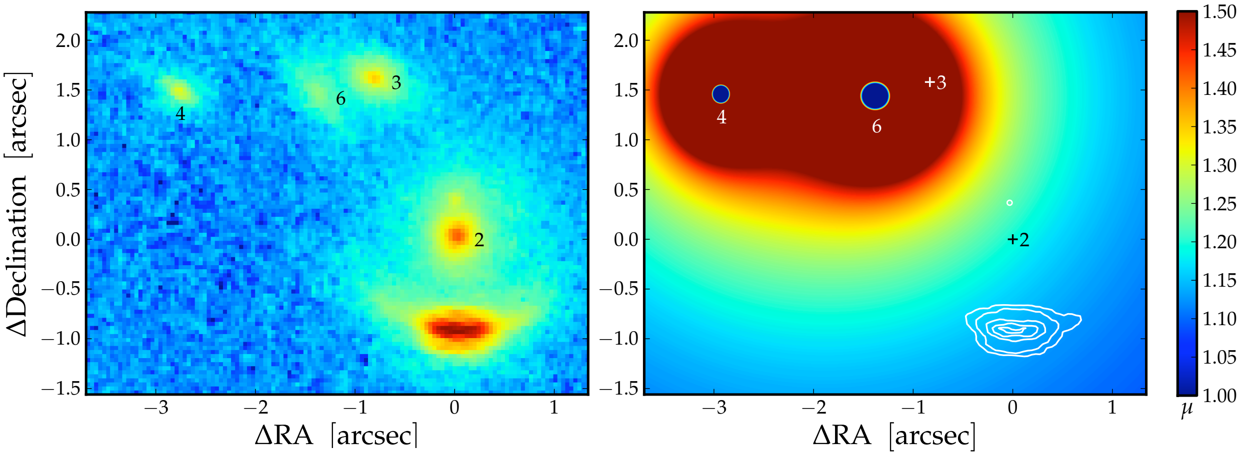

Figure 2.7: **Left:** Larger field of view of the IRAS 10214 region (*HST* F160W map) showing three satellite galaxies to the north-east. **Right:** A map of the estimated magnification contribution from the component 4 and 6 galaxies, which are not included in our modelling. Note that the colour-scale is clipped between $1 < \Delta\mu < 1.5$, i.e. 0–50% additional magnification. We argue this is an exaggerated estimate of the added magnification (see § 2.1.7 for a full description). The inner blue circle represents the saturated reverse parity magnification within each SIS critical curve. The numbered crosses indicate the centroids of the galaxies included in the lens model.

north-south dimension of the counter-image. In the isothermal case, the two measurements have equivalent dimensions. However, in practice we could not get meaningful constraints on the counter-image thickness. We attempted this with the *HST* F814W map, however there is significant uncertainty since the counter-image is located within the lens galaxy emission. Using GALFIT, the only case in which the Sersic fitting converges is if the counter-image dimensions are fixed during the minimisation. For all results in this thesis, these dimensions were fixed to that of the *HST* F814W PSF. Attempts to marginally increase this to the north-south dimensions of the *HST* F814W arc yields indistinguishable (quantitative and qualitative) residuals. This fitting challenge is compounded in the *HST* F160W map since the host contamination is even greater.

We have quantified the systematic uncertainty that results from the isothermal assumption, but it is also useful to consider the effect on source plane configuration. From the range of models considered in this work, it is clear that the Einstein radius and lens potential ellipticity share a degeneracy (as seen in their 2D posterior PDFs in Fig. 2.4). These two parameters counteract one another, in order to position the inner caustic so that the image-plane source positions are suitably reproduced. Variations to the inner density slope can be thought of in an analogous way: steeper inner-density slopes result in smaller Einstein radii which are compensated by larger ellipticity. Conversely, shallower density slopes equate to larger Einstein radii and therefore lower ellipticity. These statements are captured in the first order approximation in Marshall et al. (2007), expressed as

$$\mu \propto \frac{1}{m^2\,\varepsilon}, \tag{2.11}$$

where ε is a small ($<< \theta_{\mathrm{E}}$) angular offset from the Einstein radius. In summary, changes to the inner density slope will cause shifts to the inner caustic position, which are compensated for by the lens ellipticity. The source-plane configuration is relatively similar in our three models. It is just the size of the source plane models (and hence the relative source-plane distances from one another) that change due to the changes in total convergence (κ_{tot}). Departures from the isothermal profile will have similar results, the spread of which will reflect the observed spread in m. Stellar velocity dispersion measurements of the lens galaxy are required in order for this degeneracy to be broken, and for the inner density slope to be further constrained. This independent lens galaxy mass estimate will allow a more definitive mass model to be constrained, where the inner density slope is a free parameter in the lens modelling process.

Another source of systematic error is the neglect of two additional galaxies north-east of the main lensing galaxy. In Fig. 2.7 (left panel) we show a larger field-of-view of the *HST* F160W observation, revealing other galaxies in the field. Maintaining consistency with Eisenhardt et al. (1996) we label these galaxies component 4 and 6 (see Fig. 2.7; component 5 is the IRAS 10214 counter-image in their original paper). Component 4 has a spectroscopic redshift measured by the Goodrich et al. (1996) Mg II absorption detection at $z = 1.316$, which is consistent with the photometric redshift of $z = 1.358$ derived by Simpson et al. (2012, in prep.) using multiple *HST* filters. Component 6 has neither a spectroscopic nor a photometric redshift. For the purpose of uncertainty estimation we assign it the redshift of its nearest neighbour (component 3 at $z = 0.782$). This is a conservative assumption, since this redshift has the highest lensing potential due to the source-lens redshift configuration (i.e. the relative angular diameter distances). The posterior PDFs of these photometric redshift estimates are non-Gaussian, however the 68% confidence levels are of order $\Delta z = 0.3$. The differing redshifts of the main lens and satellite galaxies are easily accounted for since the GLAMROC software package is able to perform ray-tracing in multiple lens planes.

The Einstein radii of component 4 and 6 are estimated by scaling the main lens Einstein radius using the ratio of the K-band magnitudes and the Faber-Jackson relation where mass $m \propto \sigma_v^4$ (Faber & Jackson, 1976) as well as accounting for their different redshifts[6]. This over-estimates their Einstein radii since the primary lens and component 3 Einstein radii already include some convergence from component 4 and 6.

The additional magnification from component 4 and 6 is calculated by

$$\Delta\mu = \left[\{1-(\kappa_4+\kappa_6)\}^2 - (\vec{\gamma}_4^2+\vec{\gamma}_6^2)\right]^{-1}, \tag{2.12}$$

where $\kappa_{4,6}$ and $\vec{\gamma}_{4,6}$ are the convergence and shear of component 4 and 6 respectively. In the right panel of Fig. 2.7 we show the additional magnification from these two satellite galaxies. The colour-scale has been clipped between values of $\Delta\mu$ = 1.0 - 1.5 (i.e. $\Delta\mu$ = 0 – 50%) for illustration. The figure shows that their combined potential results in a small additional magnification at the 10–15% level, bearing in mind that this is an exaggerated effect due to the reasons stated previously. This justifies our decision to neglect the potential of these galaxies and also illustrates why we were unable to get useful constraints on their velocity dispersions when an attempt was made to include them in the lens fitting procedure.

---

[6] This assumes that the stellar velocity dispersion (σ_v) is equal to the modelled isothermal dark matter velocity dispersion.

CHAPTER 3

RESOLVED RADIO EMISSION

R.P. Deane, S. Rawlings, P.J. Marshall, I. Heywood, H.-R. Klöckner, K. Grainge, T. Mauch, S. Serjeant
“The preferentially magnified active nucleus in IRAS F10214+47: I. Lens model and spatially resolved radio emission”
MNRAS, submitted

This chapter presents a new lens model and spatially-resolved radio data, as well as a deep *HST* F160W map of IRAS 10214. The lens modelling employs a Bayesian Markov Chain Monte Carlo algorithm with extended-source, forward ray-tracing. Using these high resolution *HST*, *MERLIN* and *VLA* maps, the algorithm allows us to constrain the level of distortion to the continuum spectral energy distribution resulting from emission components with differing magnification factors, due to their size and proximity to the caustic. Our lens model finds the narrow line region (NLR), and by proxy the active nucleus, is preferentially magnified. This supports previous claims that preferential magnification could mask the expected polycyclic aromatic hydrocarbon spectral features in the *Spitzer* mid-infrared spectrum which roughly trace the star-forming regions. Furthermore, we show the arc-to-counter-image flux ratio is not a good estimate of the magnification in this system, despite its common use in the IRAS FSC10214+47 literature. Our lens modelling suggests magnifications of $\mu \sim 15-20 \pm 5$ for the *HST* F814W, *MERLIN* 1.7 GHz and *VLA* 8 GHz maps, significantly lower than the canonical values of $\mu = 50-100$ often used for this system. Systematic errors such as the dark matter density slope and co-location of stellar and dark matter centroids dominate the uncertainties in the lens model.

3.1 Observations

The radio regime was one of the least studied sectors of the electromagnetic spectrum in the case of IRAS 10214 prior to this work. In this section we present the new and archival data that are used in this thesis for both the lens model derivation and source plane investigation.

3.1.1 Archival Observations

A significant number of competitive, yet unpublished observations lay in the *MERLIN*, *VLA* and *HST* archives prior to this work. We obtained all these datasets and reprocessed them as is described below. We also use the quoted flux densities and centroid positions of the *VLA* 1.49 GHz, 4.86 GHz and 8.44 GHz maps described in Lawrence et al. (1993).

MERLIN 1.7 GHz

IRAS 10214 was observed for 24 hours with the *MERLIN* array on 2 November 1995. The observation included the 76 metre Lovell Telescope as well as the Wardle antenna making this an 8 element observation (28 baselines). $J1027+480$ was used as a phase calibrator (angular separation $\Delta\theta \sim 1^{\circ}$) and *JVAS* $J2136+0041$ was used as a pointing calibrator (positional accuracy < 0.36 mas). IRAS 10214 was observed for an average of 5 minutes in the roughly 7.5 minute phase-target cycle (this period varied by ∼30 percent over the course of the observation). Preliminary calibration of the uv-data set was carried out with the *MERLIN AIPS* pipeline[1], which performs initial fringe-fitting (calibration of delays, rates and phase), and phase and amplitude calibration. Following this preliminary calibration, a more detailed, manual calibration is performed in *AIPS*. This was performed in a cyclic process with detailed data editing to excise Radio Frequency Interference (RFI); refine delay calibration, as well as perform phase and amplitude self-calibration on the phase reference source.

---

[1] http://www.merlin.ac.uk/user_guide/AIPS_scripts.html

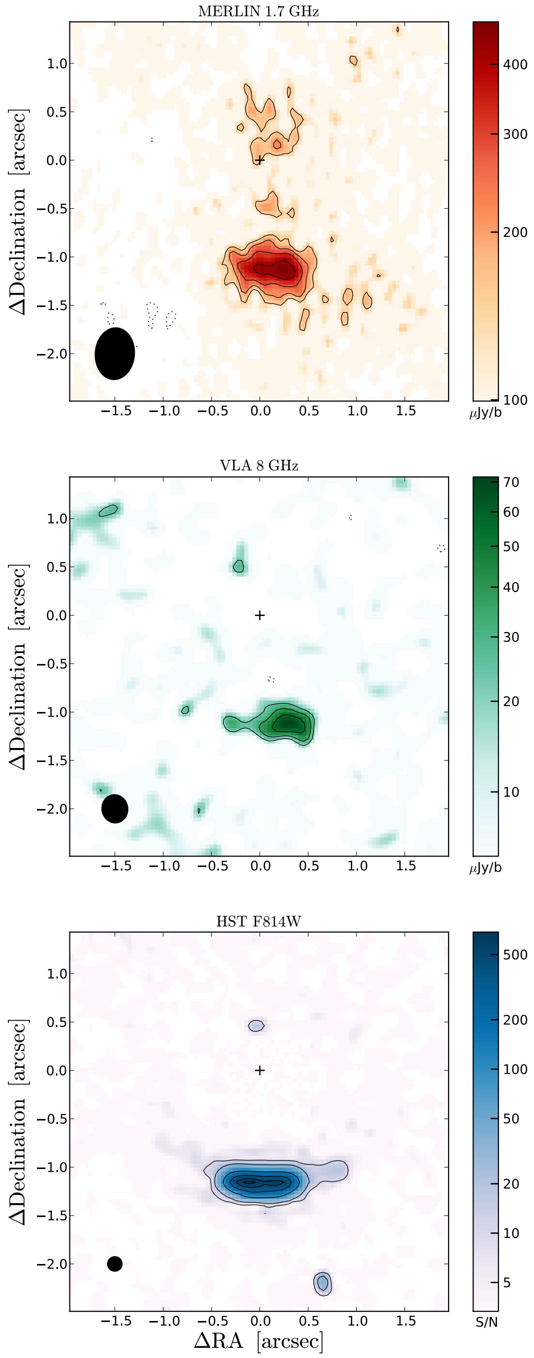

Figure 3.1: **Top panel:** *MERLIN* 1.7 GHz map with $\sigma \sim 46$ μJy per 405 × 349 mas^2 beam. **Middle panel:** 8 GHz *VLA* map with $\sigma \sim 11$ μJy per 292 × 267 mas^2 beam. Contours for both radio maps are at $\pm 3\sigma$ and increase by a factor of $\sqrt{2}$. Dashed lines represent the negative contours. **Bottom panel:** *HST* F814W map with counter-image and arc. The integrated arc/counter-image flux density ratio is $\breve{\mu} \sim 75 \pm 25$. The *HST* PSF through this filter has a FWHM of ~100 mas, as detailed in (Eisenhardt et al., 1996). Note that the lens has been fit using GALFIT and removed from this image. The FWHM of all PSFs are shown in the lower left of each frame. In all panels the cross indicates the Sersic-fitted centroid of the lensing galaxy as measured from the *HST* F160W map which is within 10 mas of the equivalent measurement with the *HST* F814W map.

We achieve a 1-σ noise sensitivity of $\sim$46 μJy per 405 × 349 mas^2 naturally-weighted beam (Briggs `robust` weighting parameter = 5). The resultant map reveals a resolved 'arc' (Fig. 3.1, top panel) roughly co-spatial with the *HST* F814W image (Eisenhardt et al., 1996), however the *dominant* peaks of these two maps are offset by $\sim$0.4 arcsec in RA. A resolved 1.7 GHz detection is only achieved for visibility weightings with a Briggs `robust` weighting parameter > 2. The foreground lensing galaxy centroid is indicated by a cross in all three panels in Fig. 3.1. The 1.7 GHz map shows a number of 2-3 σ peaks that are seen in this region as well as the counter-image position as reported by (Eisenhardt et al., 1996), however nothing further can be reliably inferred at this low significance. To probe larger scale features we taper the *uv*-data (< 700 kλ) which imposes a Gaussian weighting to the data as function of baseline length measured in wavelengths. This is a function centered on 0 λ and has a 700 kλ FWHM.

A comparison of the *uv*-tapered and full resolution maps suggests that no flux is resolved out within the uncertainties. In addition, the 330 MHz through 4.8 GHz apparent spectral index suggests, within the errors, that no significant extended flux is resolved out in the *MERLIN* 1.7 GHz observations. It appears most likely that this 2-3 σ emission is associated with the lens given its inconsistency with the plausible counter-image locations. Radio emission at the mJy level in lensing galaxies is not unexpected, as shown in a CLASS[2] example (More et al., 2008) as well as a sample of 10 SDSS[3]-selected lenses (Boyce et al., 2006).

VLA A-array 8 GHz

IRAS 10214 was observed twice with the *VLA* (A-array) in the 8 GHz band (*X*-band) in the 1990s, both with consistent flux densities and centroid positions. The second, deeper observation (unpublished) achieved a sensitivity of 13 μJy beam^{-1} after careful calibration and editing. Both datasets were calibrated using standard techniques in the *AIPS* data reduction package, following which the two calibrated *uv*-datasets were combined using the DBCON task. These observations were not at the typical frequencies where antenna gain curves are required ($>$ 15 GHz), nonetheless they were applied to maximise accuracy. The re-reduced 1991 *uv*-dataset was precessed from Equinox B1950, Epoch B1979.0 (barycentric) to J2000 coordinates with offsets calculated with the STARLINK `COCO` task set on high resolution (0.1 mas precision). The

---

[2] Cosmic Lens All-Sky Survey, www.aoc.nrao.edu/~smyers/class.html

[3] Sloan Digital Sky Survey, www.sdss.org

peak of the precessed 1991 map is co-spatial with the 1995 map. Astrometric accuracy at the *VLA* can be $\Delta\theta \simeq 50$ mas in A-array in good conditions and $\Delta\theta \simeq 100$ mas under more normal conditions (Ulvestad et al. 2009). The absolute positions of the two phase calibrators used in the 1995 observation ($J1033$+4116 and $J1027$+480) were within $\Delta\theta < 3$ mas and 31 mas of their catalogued positions respectively. The positional errors are (ΔRA = 0.20 mas, ΔDec = 0.40 mas) and (ΔRA = 0.45 mas, ΔDec = 0.75 mas), as sourced from the International Celestial Reference Frame (ICRF, Ma et al. 1998) and the *VLBA* Calibrator Survey (VCS1, Beasley et al. 2002) respectively.

The *uv*-datasets were combined and transformed to produce the map in Fig. 3.1 (middle panel). Apart from the detection of the main peak associated with the optical arc, our combined 1991/1995 8 GHz map (Fig. 3.1, middle panel) reveals two lower significance ($\sim$3-σ) peaks, one eastward of the optical arc, the other eastward of the optical counter-image. The latter has a very low arc/'counter-image' ratio ($\breve{\mu}$ = 8), inconsistent with all previous lensing results (and this work, as seen in §**??**). The 'counter-image' is not seen in either of the 1991 and 1995 maps and so despite its 4-σ significance this is not a robust feature. We therefore assume the detection is *not* secure leading to an 8 GHz lower limit of $\breve{\mu} > 24$, however the $4-\sigma$ peak remains in the lens fitting procedure allowing the Markov Chain Monte Carlo algorithm described in Section 3 to test whether this is a feasible counter-image.

3.1.2 New Observations

In order to increase the radio spectral coverage of IRAS 10214, we performed unresolved low and high frequency observations with the *GMRT* and *AMI* arrays respectively.

GMRT 330 MHz

IRAS 10214 was observed with the *GMRT* array on 3 July 2009 at 330 MHz for 25 minutes. Data processing was performed with an automated calibration and imaging pipeline. The pipeline is based on Python, AIPS and ParselTongue (Kettenis et al., 2006) and has been specially developed to process *GMRT* data. The full technical description of this calibration and imaging pipeline is extensive, and therefore presented in detail in Klöckner (2012, in prep.). Here we just give a brief description of the amplitude calibration. Absolute amplitude calibration is based on the AIPS task SETJY. Instead of using a pseudo-continuum

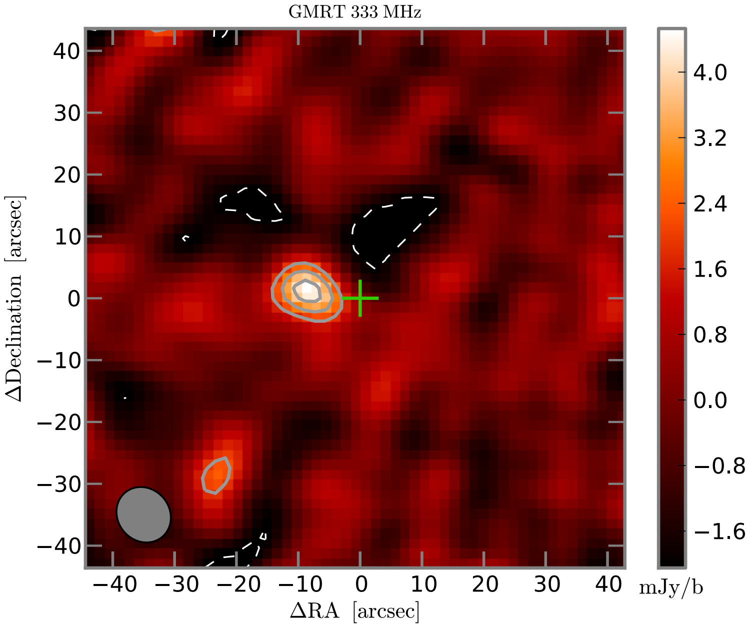

Figure 3.2: *GMRT* map with grey contours starting at ± 3-σ in 1-σ steps of $\sigma \sim 0.71$ mJy per 9.7×7.8 arcsec^2 beam. The integrated flux density is $S_{\rm int} \sim 4.42 \pm 1.48$ mJy. The green cross indicates the position of the centre of the arc of IRAS 10214 (RA = $10^{\rm h}$ $24^{\rm m}$ $34.564^{\rm s}$, Dec = 47° 09' 9.61"). Note that the size of this cross is purely illustrative and does not represent the astrometric uncertainty of $\Delta\theta \sim 1$ arcsec for the *GMRT* detection. Absolute astrometric accuracy is compromised in the faceted self-calibration process which is essential to achieve reasonable dynamic range over the large (> 1 deg^2) field of view at low frequencies.

measure to perform amplitude calibration, a single channel (chan #60, ν = 332.5 MHz) is used for improved accuracy. This resulted in a flux density measurement of 46.07 Jy for 3C 147. The final ∼1.4 deg field-of-view image is catalogued and evaluated on the basis of known radio catalogues such as FIRST, NVSS, WENSS (Becker et al., 1995; Condon et al., 1998; Rengelink et al., 1997) in order to verify the flux density calibration and astrometric accuracy (Mauch et al., 2012, in prep.).

The maximum in the final image is 706 mJy beam^{-1} and the noise is 0.56 mJy beam^{-1} at an averaged observing frequency of 333 MHz. The global dynamic range, using the maximum flux density and the noise, is ∼1253, whereas the local dynamic range, which is determined at 7 bright sources in the field and is 107. At a 5-σ detection limit of 2.82 mJy, 262 sources were catalogued.

IRAS 10214 is automatically detected at 6-σ, based on the local noise estimate quoted in Table 3.1. The source is not extended having a fitted major- and minor-axis of 9.7×7.8 arcsec and a position angle of 60°, the uncertainty in the positional fitting is 0.2 arcsec. The flux density measures of IRAS 10214 at 333 MHz

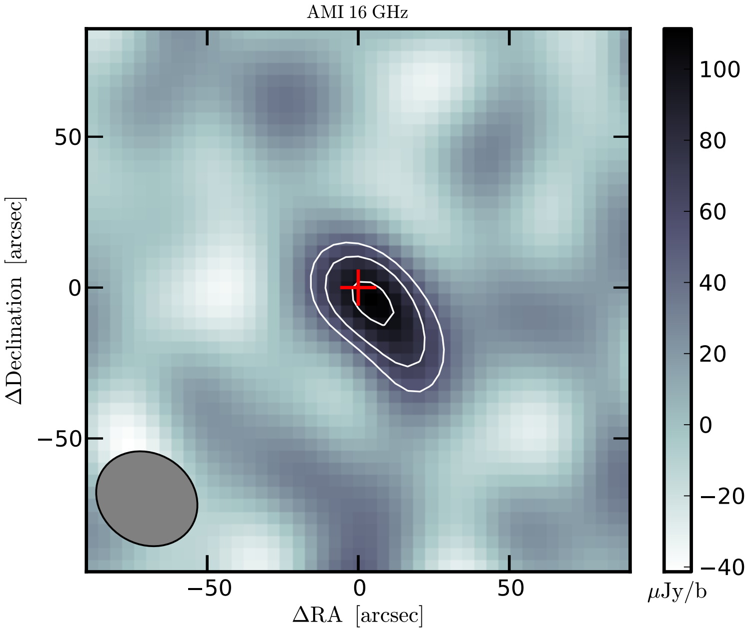

Figure 3.3: AMI map with white contours starting at ±3-σ in 1-σ steps of $\sigma \sim 17$ μJy per 34.8×30 arcsec^2 beam. The integrated flux density is $S_{\rm int} \sim 144$ μJy. The red cross indicates the position of the centre of the arc of IRAS 10214 (RA = $10^{\rm h}$ $24^{\rm m}$ $34.564^{\rm s}$, Dec = 47° 09' 9.61"). Note that the size of this cross is purely illustrative and does not represent the astrometric uncertainty of $\Delta\theta \sim 2$ arcsec.

are the peak flux density $S_{\rm peak} = 4.42\pm0.71$ mJy beam^{-1} and integrated flux density $S_{\rm int} = 4.42\pm1.48$ mJy.

16 GHz Arcminute Micro-Kelvin Imager Observations

IRAS 10214 was observed on 15 December 2009 for 12 hours by the AMI-LA (Zwart et al., 2008). The telescope observes between 13.5 and 18 GHz in six spectral channels of 0.75 GHz bandwidth. The source $J1027{+}4803$ was observed for 100 s every 600 s for accurate phase calibration. Flux calibration was performed using short observations of 3C 286, which was assumed to have an I+Q flux of 3.53 Jy at 15 GHz and a spectral index of 0.72 (Perley, private communication). The data were flagged and calibrated using REDUCE, a local software package developed for AMI. A total of 14% of the data were flagged due to a combination of pointing errors, shadowing and RFI. The calibrated data were then mapped and CLEANed in AIPS using the IMAGR task. The integrated flux density of the detection in Fig. 3.3 was $S_{\rm int} \sim 144$ μJy. The final thermal noise on the continuum map was 17 μJy beam^{-1} and the map has not been corrected for the telescope primary beam response, which is well modelled by a Gaussian of FWHM 5.6 arc-minutes. The CLEAN restoring beam is 34.8 × 30.0 arcseconds at a position angle of 32.2 degrees. We do not expect

Telescope	**Frequency** GHz	**Flux Density**† mJy	**Noise** μJy beam^{-1}	**Bandwidth** MHz	**Beam** arcsec^2
GMRT	0.33	4.42 ±1.48	706	16	9.7 × 7.8
MERLIN	1.66	1.12 ±0.12	46	13	0.41 × 0.35
VLA	8.4	0.28 ±0.03	11	100	0.29 × 0.27
AMI	15.75	0.144 ±0.032	17	4500	34.8 × 30.0

Table 3.1: Summary of all new radio observations of IRAS 10214.
† Integrated flux densities for the unresolved maps (*AMI, GMRT*) are from a fitted Gaussian, the uncertainty of which is listed alongside. Flux densities from the resolved maps (*MERLIN*, *VLA*) are calculated by summing over a region defined by a 2.5-σ threshold clip, while the uncertainties are defined by the quadrature sum of the absolute amplitude calibration uncertainty and the naturally-weighted map sensitivity.

confusion with other sources within this beam based on the higher resolution 8 GHz *VLA* continuum map as well as a 35 GHz *JVLA* continuum map with 1-$\sigma \sim 40$ μJy beam^{-1} discussed in Chapter 4.

3.1.3 Multi-wavelength Overview

To first order, IRAS 10214's global SED (Fig. 3.4) is typical of an obscured AGN with significant star formation (e.g. Martínez-Sansigre et al., 2005). Both of these properties are confirmed by a number of spectral features including a polarised (>20 %), broad (~6000 km s^{-1}) C IV line (Goodrich et al., 1996) and a vast reservoir of molecular hydrogen ($H_2 \sim 10^{11}$ μ^{-1} M$_{\odot}$, Ao et al. 2008, Solomon et al. 1992b). There is substantial mid- to far-infrared dust emission ($M_{\rm dust} \sim 5 \times 10^9 \mu^{-1}$ M$_{\odot}$), strong NIR emission with a steep downward slope toward shorter wavelengths which suggests high extinction by a dusty nuclear toroidal structure (under the unified quasar model, Antonucci 1993) and/or the host galaxy (see Martínez-Sansigre et al., 2005). The host galaxy appears to dominate in the optical band (rest-frame) as shown by the 4000 Å break observed in the NIR spectrum of Lacy et al. (1998).

Our extended radio SED coverage appears to confirm the steep spectrum component, first measured in Rowan-Robinson et al. 1993 ($\alpha = 0.92 \pm 0.04$, where $\alpha \equiv -\log(S_1/S_2)/\log(\nu_1/\nu_2)$) between $\nu_{\rm obs}$ ~330 MHz to 4.8 GHz. The spectral index uncertainty is Monte Carlo derived, incorporating the flux density uncertainties from four measurements in this frequency range. The spectrum flattens between 4.8 GHz and 16 GHz with an apparent peak at 8 GHz, plausibly due to the presence of a flat-spectrum radio core. However, the flux measurements at 8 GHz and 16 GHz are separated by ~15 yr, which increases the spectral index uncertainty due to instrinsic quasar variability. Nonetheless, our measured spectral indices are $\alpha_{4.8}^{8.4} =$

$-0.53 \pm 0.09\,(0.24)$ and $\alpha_{4.8}^{16} = -0.78 \pm 0.17\,(0.26)$, where the uncertainties are Monte Carlo derived and those quoted in parentheses include the absolute flux calibration uncertainties.

Inspection of the maps in Fig. 3.1 reveals a spatial offset of $\sim$0.4±0.1 arcsec between the 8 GHz peak and both the dominant *HST* F814W peak and the quoted *VLA* 1.4 GHz centroid in Lawrence et al. (1993). This offset of the 8 GHz peak is present in both the 1991 and 1995 8 GHz datasets. Adding the astrometric errors from the 1991 1.49 GHz and 8.44 GHz observations in quadrature, Lawrence et al. (1993) find an offset between the optical/NIR positions and the average radio position $\Delta\theta = 0.63 \pm 0.37$, consistent with our more sensitive observations here. Therefore, this offset appears reasonably robust and independently verified.

The regions of the global SED probed by the spatially-resolved maps presented in this work are illustrated by the vertical lines on the SED plot in Fig. 3.4: *MERLIN* 1.7 GHz (red), *VLA* 8 GHz (green), *HST* F814W (blue), and *HST* F160W (yellow). The *HST* F160W filter appears to be dominated by stellar emission based on the SED shape, and the 4000 Å break (Lacy et al., 1998), whereas the *HST* F814W map of Eisenhardt et al. (1996) is dominated by scattered quasar light as inferred from *HST* polarisation observations.

In subsequent modelling, we assume that the 1.7 GHz map is dominated by a radio lobe. The term 'radio lobe' is used relatively loosely here: the steep apparent spectral index suggests that this is an aged distribution of relativistic electrons in a magnetised plasma. As we will see in §**??**, the inferred source plane brightness temperature is evidence that this is not the core of a high powered jet. We therefore describe it as a radio lobe with the full expectation that some of this non-thermal emission is associated with star formation. While the radio spectrum flattening around 8 GHz suggests that this map may be dominated by a radio core, we show in Chapter 5 that VLBI observations are not consistent with this. We therefore expect the 8 GHz map includes emission contributions from star formation and/or radio jets. We emphasize here that we are modelling emission regions and not physical components, however, the polarisation properties of the *HST* F814W map suggests that this region in particular is dominated by a single physical component (i.e. the scattered quasar light). Finally, we later argue that the majority of the quasar light scattering occurs in the NLR. Therefore, the *HST* F814W map will also be used as a rough tracer of the NLR.

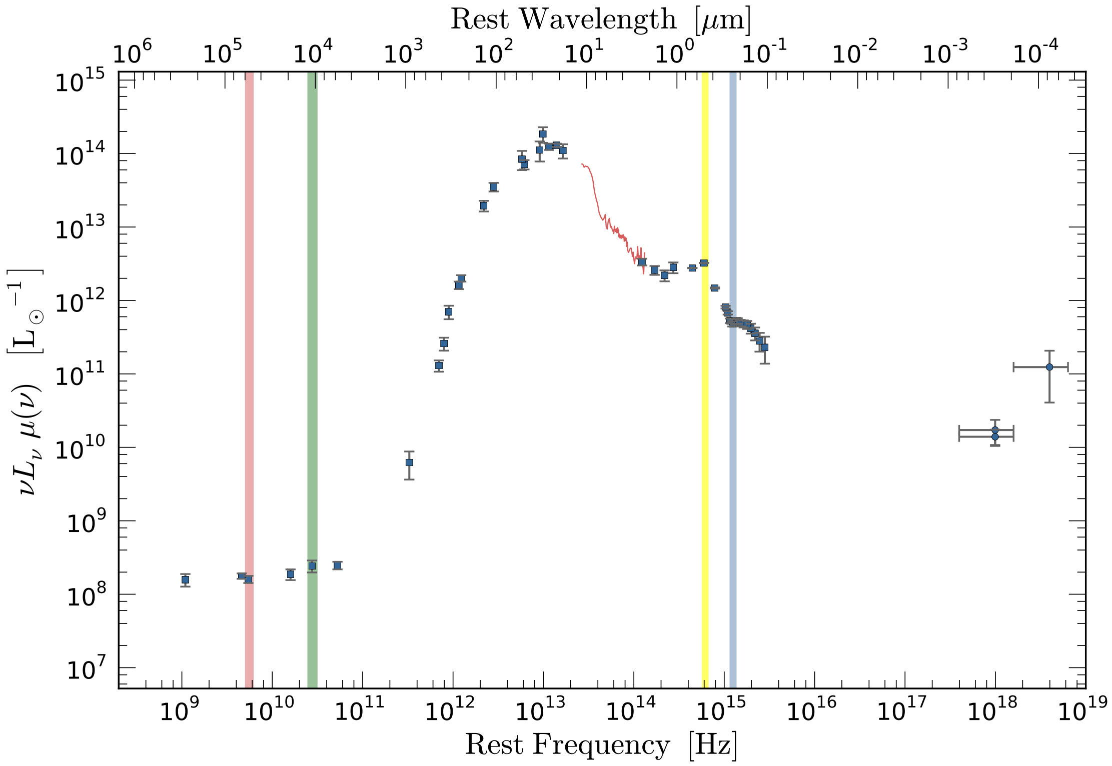

Figure 3.4: The *apparent* (i.e. lensed) X-ray through radio SED of IRAS FSC10214 showing the three bands probed by the high resolution imaging presented in this work: radio lobe (red), *VLA* 8 GHz (green), scattered quasar light (blue) as traced by the *MERLIN* 1.7 GHz, *VLA* 8 GHz and *HST* WFPC2 instruments respectively. The yellow band represents the *HST* NICMOS 1.6 μm (F160W filter) apparent luminosity which appears to trace the host galaxy's stellar component. The dark red line in the mid-infrared is the *Spitzer* spectrum (Teplitz et al., 2006). Note that the parameter $\mu(\nu)$ accounts for the magnification boost which varies as a function of frequency due to differing sizes and positions of emission components. This function is as yet undetermined and hence included in the ordinate label. The flux densities used in this plot are sourced from Rowan-Robinson et al. (1991); Downes et al. (1992); Rowan-Robinson et al. (1993); Lawrence et al. (1993); Barvainis et al. (1995); Benford et al. (1999); Teplitz et al. (2006); Alexander et al. (2005); Solomon & Vanden Bout (2005); Ao et al. (2008); Iwasawa et al. (2010).

3.1.4 Source Plane Properties

The source plane results that follow are entirely independent fits to each map, however the identical lens model is used in each case and each image plane is convolved with the appropriate PSF. Figure 3.6 shows the 2D marginalised posterior PDFs of the source plane parameters. Each colour corresponds to one of the three observations (1.7 GHz : red, 8 GHz : green, *HST* F814W : blue). We do not explore the *AMI* 16 GHz and *GMRT* 330 MHz source plane properties since they are both unresolved and the positional uncertainty is too large ($>>$ 0.1 arcsec) to make any meaningful constraints on the intrinsic position and radius.

The *HST* F814W source plane model radius r_s = 44 mas (360 pc) is larger than that derived in Eisenhardt et al. (1996) ($2r_{814,\mathrm{Eis96}} \sim$ 11-20 mas), with a lower magnification of μ = 20±1. However, direct comparison is difficult given that the Eisenhardt source model is a uniform surface brightness circular disk, that would lead to a smaller inferred radius. Furthermore, they assume an arc-to-counter-image flux ratio $\breve{\mu}$ = 100, which appears to be their estimate of the magnification. We measure $\breve{\mu}_{814,\mathrm{model}} = 38$ which compares favourably with the derived 'magnification' in previous work ($\breve{\mu} \sim$ 50-100 in Eisenhardt et al. 1996) particularly since some differential extinction is expected at this wavelength since the counter-image light-path travels a factor $\sim$3 closer to the centre of the main lens galaxy, as argued in Nguyen et al. (1999). To achieve the required arc-to-counter-image flux ratio, a $\Delta A_v = 0.23$ is required.

The radio lobe, which is presumed to dominate the 1.7 GHz map, is fit with an intrinsic scale radius r_s = 72 mas ($\sim$600 pc) with a magnification μ = 16±1.5 ($\breve{\mu}_{1.7\mathrm{GHz,model}}$ = 32), while the 8 GHz map, has the smallest source-plane scale radius (r_s = 23 mas, 190 pc at z = 2.3). Its size and position yield a magnification of μ_{8GHz} = 18±2.5. The rest-frame brightness temperature is calculated,

$$T_\mathrm{B}(\nu_\mathrm{e}) = \frac{c^2}{2k_\mathrm{B}} \frac{S(\nu_\mathrm{o})\, \nu_\mathrm{e}{}^{-2}\, (1+z)^3}{\Omega} \tag{3.1}$$

where $S(\nu_\mathrm{o})$ is the observed flux density, ν_e is the rest frequency of the observed emission, and Ω is the apparent solid angle since surface brightness is conserved for lensed emission. The inferred brightness temperatures, $T_B \sim 1.1 \times 10^4$ K and 5×10^3 K for both radio lobe and 8 GHz components respectively, do not rule out star formation as the source of the radio emission. Typically, brightness temperatures need be above $T_\mathrm{B} > 10^5$ K to exclude major contributions from thermal stellar emission and non-thermal supernova synchrotron emission. Note that the brightness temperature of a resolved radio component is conserved and

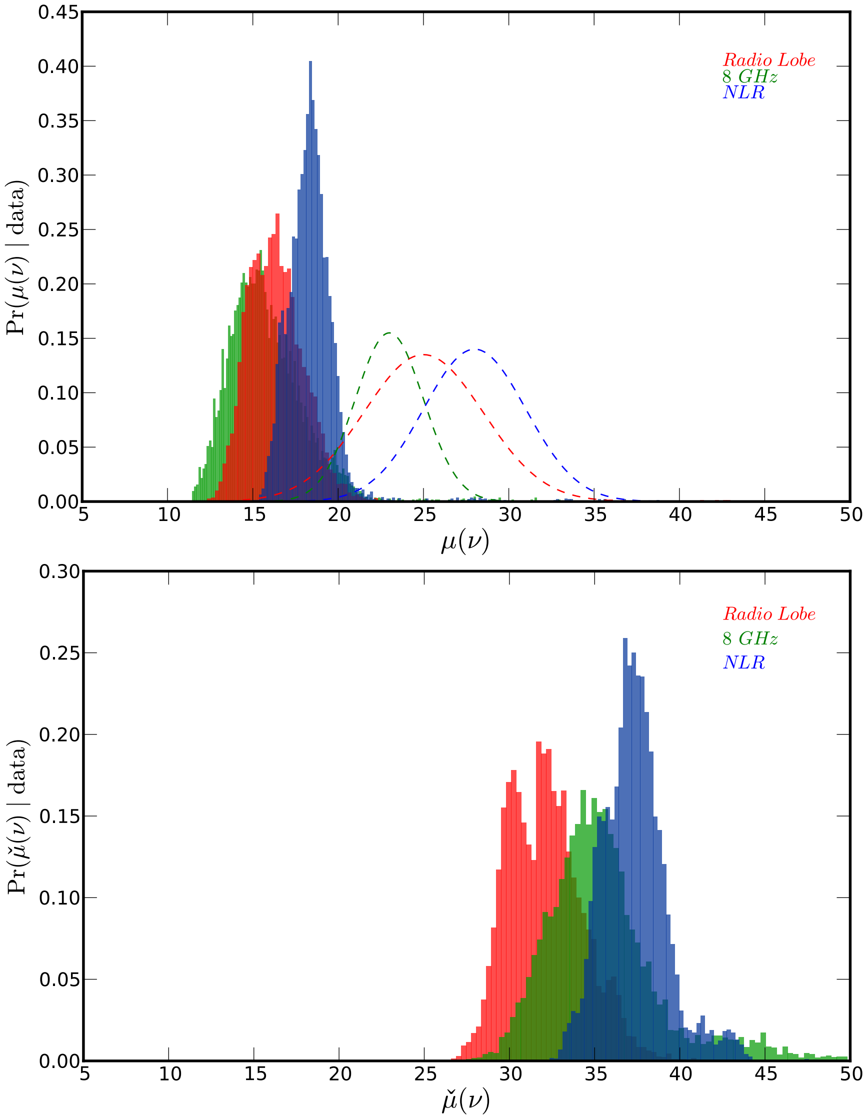

Figure 3.5: **Top Panel:** Magnification posterior PDFs of the three maps based on the derived source plane reconstruction. The colours represent the same maps as before. The dashed lines indicate the same result for Lens Model B, which indicates the scale of the systematics (∼40%) in assuming co-spatial stellar and lensing potential centroids in this system. Additional systematics are derived in §2.1.7. **Bottom Panel:** Arc-to-counter-image flux ratio posterior PDFs of all three components. Note the significant offset when compared to the true magnification shown in the top panel. This demonstrates that $\breve{\mu}$ does not accurately approximate magnification.

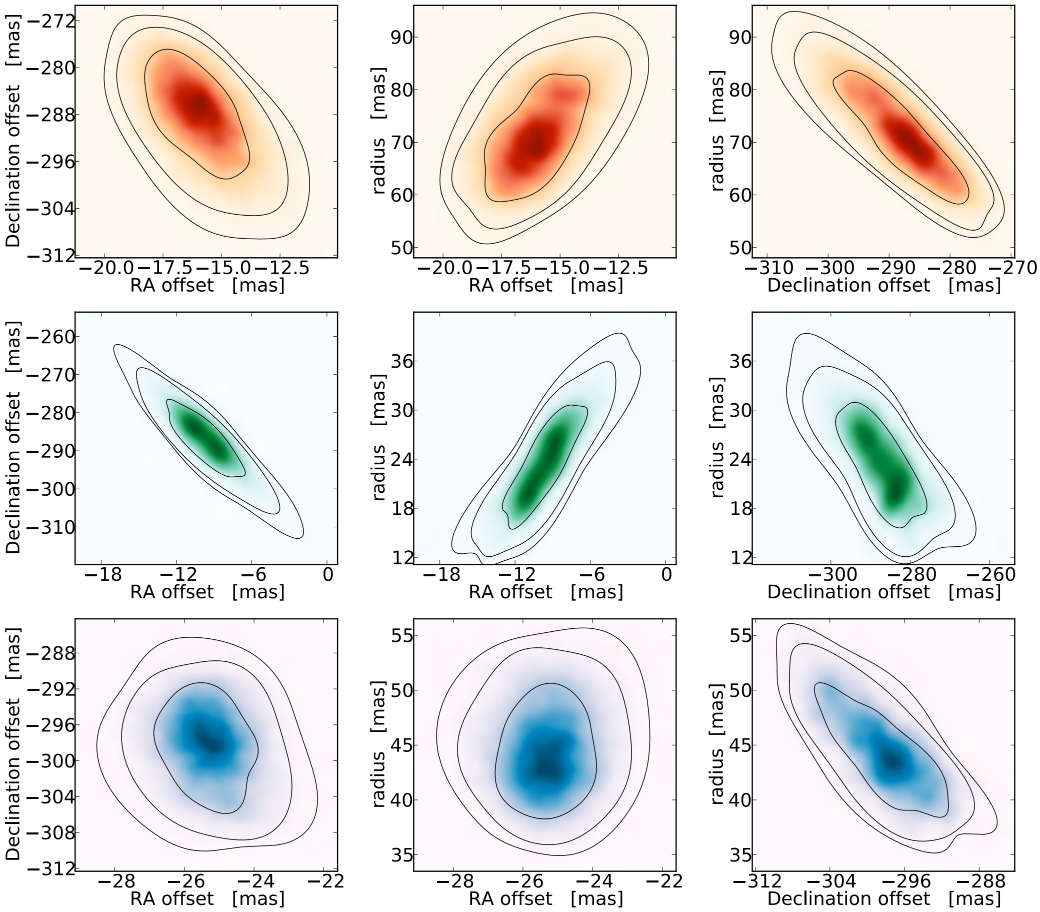

Figure 3.6: The nine contour plots show the 2D marginalised posterior PDFs of the source plane parameters (RA, Dec, scale radius) of the system. The same colour coding is used for the three source components (1.7 GHz : red, 8 GHz : green, *HST* F814W : blue). The contours show the 68%, 95% and 99% confidence levels.

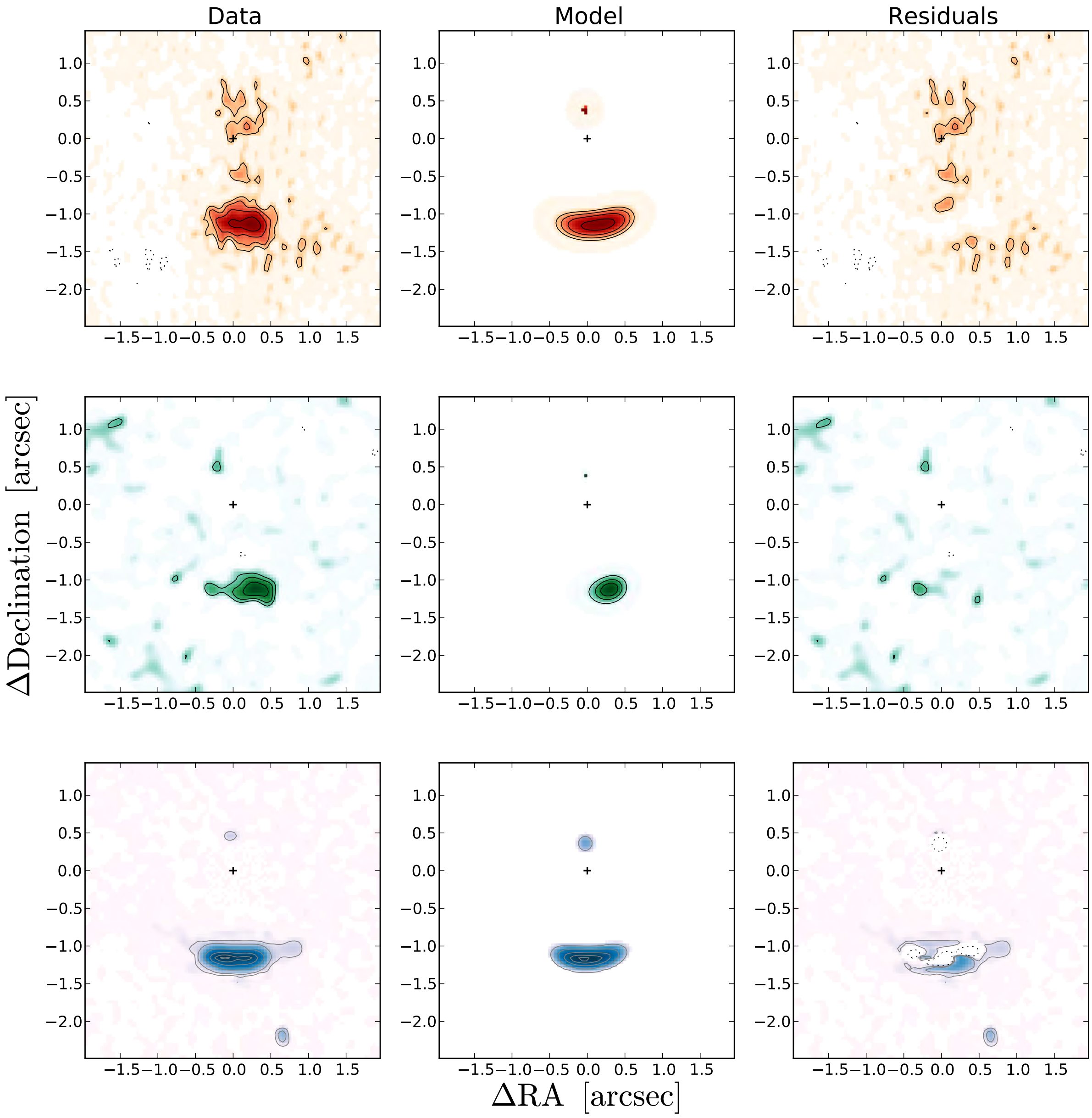

Figure 3.7: The nine images show the data, model and residuals of all three maps presented in Fig. 3.1. Note that the *logarithmic colour scaling* is the same for all images in a row. The dominant component in the arc of the *HST* F814W map is reasonably well modelled. The dashed lines indicate negative 3-σ contours in the two radio maps and 10-σ contours for the *HST* F814W map. The crosses indicate the assumed lens potential centroid (*HST* F160W Sersic centroid). The *HST* F814W residuals suggest structure/clumpiness which is repeated in some of the trial MCMC models, however this could just as likely be intrinsic source structure and not the multiple images claimed by some deconvolutions of *HST* maps. Over-plotted on the two radio maps are the *unconvolved* model counter-images for illustration. These are multiplied by a factor 10. The 1.7 GHz residuals suggest some emission consistent with the lens itself, however there is also emission south-west of the arc which is not fit by the simple source model used here.

therefore unaffected by lensing. In an analogous argument to that of brightness temperature we also calculate the source plane star formation rate density for comparison with the proposed value of a so-called 'maximal starburst', $\Sigma_{\rm SFR}^{\rm max} \sim 1000\ {\rm M}_\odot\,{\rm yr}^{-1}\,{\rm kpc}^{-2}$ (see Elmegreen, 1999; Thompson et al., 2005). To calculate the implied star formation rates from measured radio luminosities, we follow Condon et al. (2002) who find the relation

$$SFR = 1.2 \times 10^{-21}\, L_{1.4GHz}\ \ {\rm M}_\odot\,{\rm yr}^{-1} \tag{3.2}$$

which is extrapolated to masses between $0.1{\rm M}_\odot < M < 100\ {\rm M}_\odot$ assuming a Salpeter Initial Mass Function (IMF, Salpeter, 1955). We calculate the luminosity at 1.4 GHz by applying the appropriate k-correction, and converting from higher frequencies by assuming a spectral index of $\alpha = 0.8$. If we assume that all radio emission is due to star formation, we derive lensed star formation rates of $SFR \sim 4 \times 10^4\,\mu^{-1}\,{\rm M}_\odot\,{\rm yr}^{-1}$ for both the 1.7 GHz and 8 GHz flux densities. Applying the derived magnifications and source-plane scale radii, we derive star formation rate densities of $\Sigma_{\rm SFR} = 2.0 \times 10^3$ and $2.1 \times 10^4\ {\rm M}_\odot\,{\rm yr}^{-1}\,{\rm kpc}^{-2}$, both above the theoretically motivated and observed saturation value of $\Sigma_{\rm SFR}$ which seems to suggest some radio core contribution. Note that $\Sigma_{\rm SFR}$ is unaffected by lensing, analogous to brightness temperature estimates. We use the source-plane radii as simpler estimates of the solid angle, and therefore use the unlensed star formation rates.

Inspection of the 8 GHz best fit model reveals a arc-to-counter-image flux ratio of $\breve{\mu}_{\rm 8GHz,model}$ = 35, inconsistent with the $\breve{\mu}_{\rm 8GHz,data}$ = 7 measured from the 8 GHz map, which is in-line with our assessment that the tentative counter-image is not a robust feature and therefore disregarded. Moreover, an analysis of the MCMC chain shows that the model counter-image is at no point within 100 mas of the 8 GHz peak. The nature of this component is perhaps the most puzzling, since if it is a radio core, we would expect it to be barely resolved. Three possibilities could lead to an exaggerated inferred size: convolution with a time and space varying atmospheric screen (smearing out the unresolved component); a significant flux contribution from star formation; as well as the possibility of small scale (<100 pc) jets.

In Fig. 3.5 (top panel) we plot the magnification posterior PDFs of each source, given the fixed lens model. These three histograms show the confidence levels of preferential lensing in the system and that magnification μ is dependent on the emission region's size and proximity to the caustic. If these emission

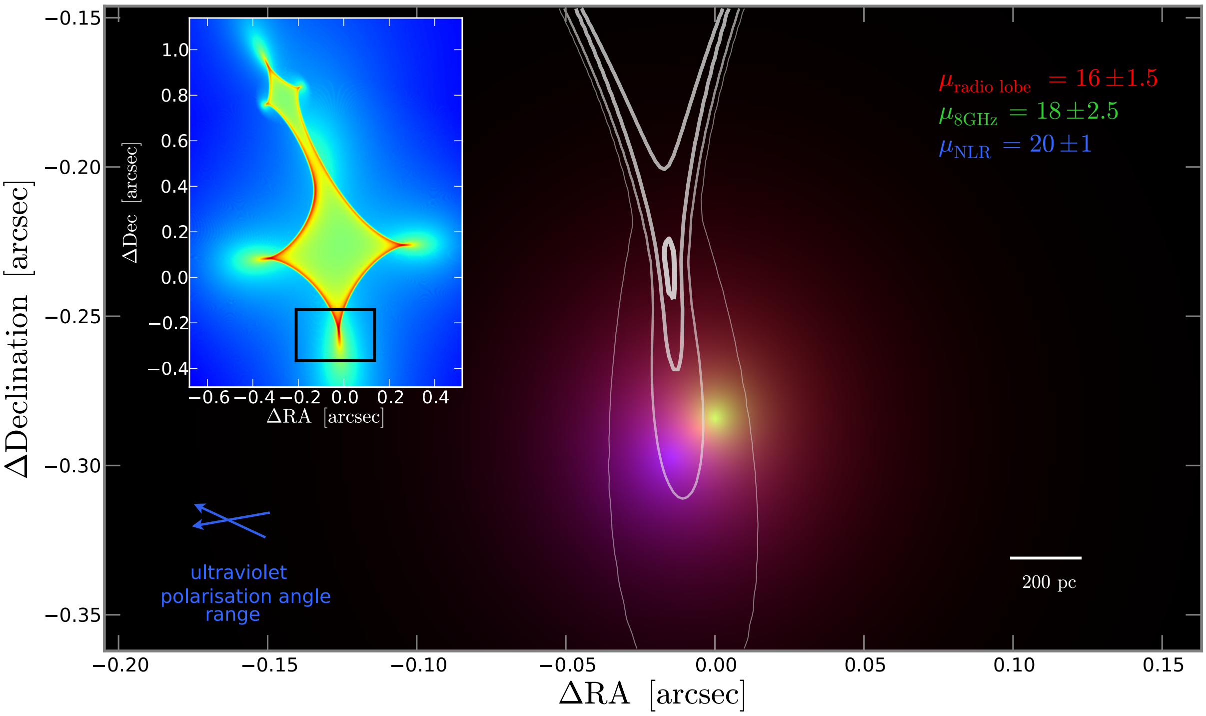

Figure 3.8: Source plane reconstruction of IRAS 10214 showing the 8 GHz component (green), scattered quasar light (blue), and radio lobe (red). The white contours represent lines of equal magnification extending from the caustic at levels μ = 10, 20, 50, 100. The inset shows the full lens caustic with colour-scale representing magnification and the black rectangle showing the borders of the enlarged region. The magnification of each source could be computed from the convolution of each source with this magnification map. This is consistent with the method we use in practice, which is to integrate the model flux in the image plane and the source plane and take the ratio.

regions dominate different regions of the spectrum, it will appear as though magnification μ is a function of frequency ν. The MCMC samples in Fig. 3.5 (top panel) were generated by taking the ratio of the image and source plane flux, where the source position and radius were taken from the original MCMC chain. The colours represent the same bands as before. We include the same magnification posterior PDFs that result from Lens Model B in dashed curves. At face value this suggests a systematic uncertainty of $\sim 40\%$, however this may be an over-estimate since the Lens Model B average χ^2_ν is ∼30% lower than that of Lens Model A. This makes a direct estimate of the systematic uncertainty that results from a fixed lens potential centroid more challenging. Nonetheless, this does demonstrate very similar *relative* magnifications in two lens models, to go with the similar source plane configurations of both Lens Models A and B. These *relative* values are the primary aim of this work and we argue that sufficient accuracy is achieved to accomplish this

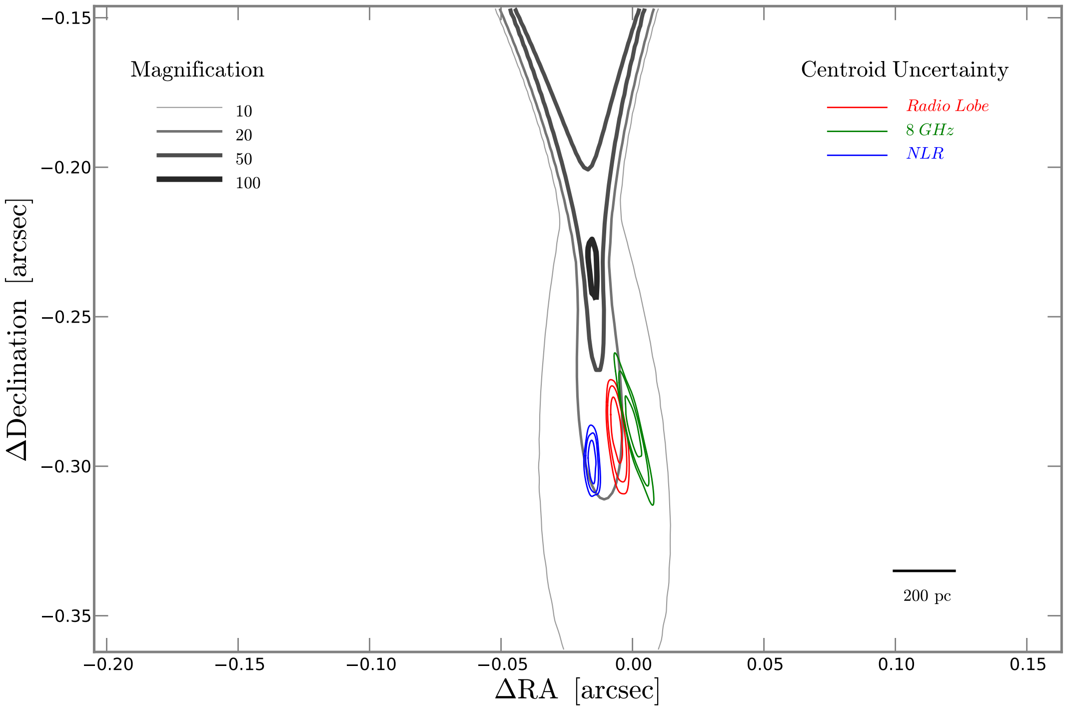

Figure 3.9: Source plane with 68, 95 and 99% confidence levels of the centroid position of each component shown in Fig. 5.3 (red, green, blue). Black contours indicate lines of equal magnification extending from the caustic at levels μ = 10, 20, 50, 100.

goal. In the bottom panel we plot the posterior PDFs of the arc-to-counter-image flux ratios for each source. The MCMC samples are drawn from each image plane model generated in the sampling of the magnification posterior PDFs (top panel) and so had higher spatial resolution and lower surface brightness thresholds set for higher accuracy. What the $\breve{\mu}$ posterior plot demonstrates is that this is *not* an accurate method to estimate magnification.

In Fig. 5.3 we show the derived source plane model with contours of magnification over-plotted. The source plane reconstruction shows the scattered quasar light in a south-easterly direction to the 8 GHz flat-spectrum component. The steep-spectrum 1.7 GHz centroid is positioned roughly along the same vector between 8 GHz and *HST* F814W centroids. The 1.7 GHz component has a larger size though, so the 8 GHz and *HST* F814W components are essentially immersed within it. In Fig. 3.9 we show the same contours of magnifications, however in this case we plot the 68, 95 and 99 % confidence levels of the centroid positions of the three components. This illustrates the degree of confidence we have on the perceived offsets between components, as well as the uncertainty of the macroscopic model, excluding systematic errors. This does not include the positional uncertainty as defined by $\sigma_\theta = 0.5\,\mathrm{FWHM/(S/N)}$, which is ~ 20 mas for both radio maps. This positional uncertainty will have a larger effect on the magnification of the smaller 8 GHz component.

Note that the best fit model arc-to-counter-image flux ratios in all cases are significantly different from the true magnification derived by calculating the image-to-source plane flux ratio. This difference (~2-3) shows that the arc-to-counter-image ratio is an invalid approximation of the true magnification, despite its extensive use in previous work on IRAS 10214.

3.1.5 Susceptibility to Imprecise Astrometry

Ockham's razor would suggest that the two radio components modelled here are most likely to be co-spatial, given the low S/N of the data. In §2 we discuss the significant care we have put into demonstrating that astrometric accuracy is maximised and how Lawrence et al. (1993) find 1.4 and 8 GHz offsets consistent with ours. However, despite these two points, a natural question arises as to the sensitivity of the configuration in Fig. 5.3 to small shifts in astrometry.

A relevant qualitative test is to determine if the two radio components could be co-spatial, given a reasonably large systematic offset in the appropriate direction. This is achieved by shifting the 8 GHz map south-east by 0.1 arcsec which is a relatively large astrometric error for 8 GHz *VLA* observations in A-array. The shifted map is then run in precisely the same MCMC routine as previously. The result is a similarly sized source plane radius ($r_s \sim 30$ mas) and source configuration, however with positional uncertainties that are consistent with the *HST* F814W source plane component. Therefore, if two independent 8 GHz *VLA* observations separated by 4 years both suffered the same astrometric error then the 8 GHz component could be co-spatial with the *HST* F814W component.

An additional test was to enforce co-spatial source plane centroids for two or all three of the respective maps. Each trial image-plane map was generated, the χ^2_ν calculated and then combined to determine the next MCMC step. This approach did not yield any meaningful results since no useful constraints could be made on a plausible source model with a common centroid (i.e. the data preferred no model at all since the output individual χ_ν^2 values worked antagonistically.

We do not include positional uncertainties in our lens modelling. As calculated before, the *VLA* 8 GHz and *MERLIN* 1.7 GHz position uncertainties are $\Delta\theta \lesssim 20$ mas. We constrain the added magnification uncertainty contribution from these random positional uncertainties by adding a 20 mas position dispersion in trial models prior to ray-tracing. This lowers the 8 GHz magnification by $\sim$10%, and broadens the magnification uncertainty to 26% ($\mu_{8\mathrm{GHz}} = 16.1 \pm 4.7$), however the effect is significantly less on the 1.7 GHz component which retains its mean magnification with a minor broadening of the uncertainty ($\mu_{\mathrm{lobe}} = 16 \pm 2.0$).

3.2 Current View

Our source plane reconstruction (Fig. 5.3) places strong constraints on the positions and radii of the three emission regions. These properties, and the inferred magnification, yield important information about the intrinsic nature of IRAS 10214. As discussed in §1, the balance of the bolometric output has been the pertinent question in the case of IRAS 10214 since its discovery. Workers have invoked preferential lensing magnifications to explain some of the peculiar features of this galaxy. Through our lens modelling we find evidence of a slight preferential magnification of the NLR (and, by proxy, the AGN) when compared with the radio lobe. The scale of preferential lensing will be more accentuated when compared to larger scale emission regions like star formation. For example, a co-spatial 3 kpc Gaussian component undergoes a magnification μ = 7 (assuming the *HST* F814W or 1.7 GHz centroids). This demonstrates a factor $\gtrsim 3$ preferentially magnified AGN/NLR component.

This preferential magnification of the AGN and NLR can qualitatively explain a range of mid-infrared features. Firstly, dust continuum models of IRAS 10214 have difficulty in reproducing the higher temperature dust ($T_{\mathrm{dust}} > 80$ K) implied by the flux levels in this spectral range ($\lambda_{\mathrm{rest}} < 40\,\mu$m, Efstathiou 2006). Secondly, the *Spitzer* mid-infrared spectrum did not reveal PAH features which are expected to be strong given the substantial molecular gas mass ($M_{\mathrm{H}_2} \sim 10^{11}\,\mu^{-1}\,\mathrm{M}_\odot$), extremely large far-infrared luminosity, and the detection of heavy molecules/atoms (e.g. HCN (1-0), Vanden Bout et al. 2004; C I, Ao et al. 2008). Teplitz et al. 2006 suggest that preferential magnification of the AGN at a level of $\sim$ 3 could suppress these PAH features, in line with the factor we determine here. It does not, however, explain the silicate emission feature revealed by this same *Spitzer* spectrum. One possible scenario that would explain the silicate emission observed towards IRAS 10214 would require it's hot, silicate emitting clouds to preferentially lensed, but not obscuring the central AGN. Alternatively, special sight-lines can be invoked, that place a toroidal structure to be suitably inclined as to obscure the AGN but still exhibit silicate in emission (see Efstathiou, 2006).

3.3 Conclusions

We have performed high resolution radio observations of a gravitationally lensed, starburst/AGN at $z = 2.3$. We have developed a Bayesian MCMC algorithm that performs forward ray-tracing on extended source models to constrain the lens model. Equipped with this model and the extensive multi-wavelength coverage, we investigate the source plane properties of our two resolved radio maps and the *HST* rest-frame ultraviolet image and make the following conclusions.

1. From the nature of this galaxy and its global spectral energy distribution we argue that the *MERLIN* 1.7 GHz and *HST* F814W maps are dominated by the radio lobe and scattered quasar emission respectively. The nature of the 8 GHz emission is likely a combination of supernovae and radio core/jet emission, which is explored in more detail in combination with VLBI observations presented in Chapter 5.
2. We find a 30% preferentially lensed NLR over the radio lobe component owing to their different scales and proximity to the caustic. The NLR/AGN is a factor $\gtrsim$3 preferentially lensed over a co-located, 3 kpc radius emission component. This could explain some of the observed peculiarities in IRAS 10214 since it would mask the expected PAH features in the spectrum and would also contribute towards the measured mid-IR ‘excess’ (Efstathiou, 2006).
3. This demonstration of preferential lensing shows that the brightest lenses may be the most affected since the survey selection band is likely to be the very wavelength that is preferentially magnified. This is true in the case in IRAS 10214 which was originally selected at rest-frame $\lambda_{\rm rest} \sim 18$ and 30 μm, which is dominated by preferentially magnified, AGN-heated, hot dust. This will be an interesting point of comparison once similar studies are performed on the 500 μm selected *Herschel* lenses (Negrello et al., 2010).

4. We have demonstrated that the arc-to-counter-image flux density ratio is not an accurate estimate of magnification in this system, as has been used previously. It is incorrect by a factor $\gtrsim 2$.

5. There is some evidence for a gravitational potential centroid offset from the baryon centroid of the main lens (component 2). This increases the systematics substantially ($\sim 40\%$), a source of uncertainty not usually considered in strong lensing analyses. This value may be an over-estimate however, since the χ^2_ν value is 30% lower in Lens Model B, so we are not comparing equivalent models. Despite the large systematics, the overall source plane configuration and global picture of a preferentially magnified NLR/AGN remains consistent.

This chapter has described methods to quantify the relative magnification factors of different emission regions. What seems clear however, is that the radio maps presented here are not unambiguous tracers of physical components (i.e. star formation, jets, the active nucleus). As a result, we have undertaken observations that are clearer proxies of these components. We present spatially-resolved CO $(1\rightarrow0)$ and 1.7 GHz VLBI imaging in Chapters 4&5 respectively.

CHAPTER 4

RESOLVED COLD MOLECULAR GAS

R.P. Deane, I. Heywood, S. Rawlings, P.J. Marshall

"The preferentially magnified active nucleus in IRAS F10214+47: II. Spatially resolved cold molecular gas"

MNRAS, submitted

This chapter presents *Jansky Very Large Array (JVLA)* observations of the cold (CO (1→0)) molecular gas in IRAS FSC10214+4724, a lensed Ultra-Luminous InfraRed Galaxy (ULIRG) at $z = 2.3$ with an obscured active nucleus. The galaxy is spatially and spectrally well-resolved in the CO (1→0) emission line. This enables a number of lines of enquiry not available to unresolved detections and illustrates the unique ability of radio telescopes to spatially resolve cold gas at high-redshift. The total intensity and velocity map reveal a reasonably ordered system, however there is some evidence for minor merger activity. A CO (1→0) counter-image is detected at the 3-σ level. Five of the 42 km s^{-1} channels (with >5-σ detections) are mapped back into the source plane and their total magnification posterior probability distribution functions (PDFs) are sampled. This reveals a roughly linear arrangement, tentatively a rotating disk. We derive a molecular gas mass of $M_{\rm gas}$ = 1.2 ±0.4 × 10^{10} M$_\odot$, assuming a ULIRG CO-to-H$_2$ conversion ratio of $\alpha = 0.8$ M$_\odot$ (K km s^{-1} pc^2)$^{-1}$ that agrees well with the derived range of $\alpha = 0.3 - 1.3$ (K km s^{-1} pc^2)$^{-1}$ for separate dynamical mass estimates at assumed inclinations of $i = 90° - 30°$. The lens modelling and CO (1→0) spectrum asymmetry suggest that there may be substantial (factor $\sim$2) preferential lensing of certain individual channels, however the CO (1$\rightarrow$0) channel flux uncertainties limit the significance of this result. We predict a distortion of the CO line Spectral Energy Distribution (SED) where higher order J lines that are partially excited by AGN heating will be preferentially lensed owing to their smaller solid angles and closer proximity to the AGN, and therefore the cusp of the caustic. Comparison with previous results shows that the AGN and narrow line region in IRAS 10214 are preferentially lensed by a factor > 3 which distorts the global continuum emission SED and raises caution in unsophisticated uses of IRAS 10214 as an archetype high-redshift ULIRG. We show evidence of an extended low-excitation gas reservoir that either contains half the total gas mass or has a different CO-to-H_2 conversion ratio.

In this chapter we explore the cold gas properties as probed by the CO (1$\rightarrow$0) emission line. The *Jansky VLA* and the *IRAM Plateau de Bure Interferometer* have undergone a remarkable improvement in sensitivity at millimetre and centimetre wavelengths. This combined with the larger bandwidths has enabled more efficient, dedicated studies of high-redshift galaxies though the various transitions of the CO ladder (e.g. Carilli et al., 2010; Greve et al., 2005; Daddi et al., 2010). IRAS 10214 itself was the first high-redshift galaxy detected in CO (Brown & Vanden Bout, 1991; Solomon et al., 1992a), however, this and most other high-redshift detections that followed were made in the mid- to high-J lines, primarily due to the receiver sensitivity and available atmospheric windows. Relative to the rest of the CO ladder, the J 1$\rightarrow$0 line is a less-biased tracer of the total molecular mass, since higher rotational lines require higher temperatures and densities for excitation. Some observations have shown evidence for extended gas reservoirs at low excitation temperatures (see Riechers et al., 2011b; Ivison et al., 2011), suggesting that the mid-to-high-J lines were biased tracers of the total molecular gas content in higher redshift galaxies. However, Riechers et al. (2011a) performed a CO (1$\rightarrow$0) analysis of five high-redshift lensed quasars (including IRAS 10214) and found no evidence for gas reservoirs untraced by the previously observed higher-J CO lines. However, this analysis was based on unresolved (or barely resolved) CO (1$\rightarrow$0) imaging and the assumption that all physical components undergo the same magnification boost. Here we wish to address the following question: do the AGN and star forming components undergo significantly different magnification boosts in IRAS 10214, by virtue of their different size and centroid positions?

4.1 Observations

We observed the CO (1→0) rotational line, redshifted to $\nu_{\rm obs}$ = 35.08376 GHz, toward IRAS 10214 using the *JVLA* (C configuration) in October 2010. Total on-source integration time was 3 h. The WIDAR correlator was used in OSRO-2 spectral line mode, employing 128 MHz of bandwidth per polarisation, split into 256 channels. After applying a natural weighting scheme to the uv-data, a 500 kHz channel sensitivity of $\sim$500 μJy beam^{-1} is achieved. Absolute flux calibration was performed with the quasar J0713+4349 – an *JVLA* recommended choice at this observing frequency. Phase and bandpass calibration were carried out with the nearby ($\Delta\theta = 1^{\circ}$) *VLBA* calibrator, J1027+4803. The target was observed for 2.3 minutes in each 3 minute phase-target cycle to track the rapid phase variations at this frequency.

All data reduction was performed using standard reduction techniques in *AIPS*, however, phase delay corrections were required and were calculated with the `FRING` task. Additional data inspection was performed with CASA. Data were edited in the full spectral and temporal resolution of 500 kHz and 1 second respectively. After phase calibration, the data were averaged into 5 MHz (ΔV = 42 km s^{-1}) channels for imaging. All maps were generated with natural weighting yielding a synthesised beam size $\theta_{\rm syn} \sim 0.82 \times 0.62$ arcsec^2.

4.2 Results

In Fig. 4.2 we show twelve 42 km s^{-1} channel maps of IRAS 10214, each with a noise level of $\sigma_{\rm N} \sim$ 170 μJy beam^{-1}. There is clear emission above 3-σ significance associated with the *HST* F814W maps (rest-frame UV; red contours) for a velocity range of $\sim$340 km s^{-1}. These channels are entirely independent (i.e. no Hanning smoothing is applied after channel averaging).

The integrated intensity map (Fig. 4.1) was generated by clipping all emission below 2-σ in individual channels, before their summation. The map reveals a clearly extended morphology, particularly in the east-west direction which spans $\sim$ 3.5 arcsec. An 'arc-like' structure is observed, and this is clearer still in a few of the channel maps. The peak of the CO (1→0) total intensity map is co-spatial with the *Hubble Space Telescope (HST)* rest-frame UV map. Accounting for the lower spatial resolution of this map, the source is significantly more extended in CO (1→0) than the optical, near-infrared and radio components presented in

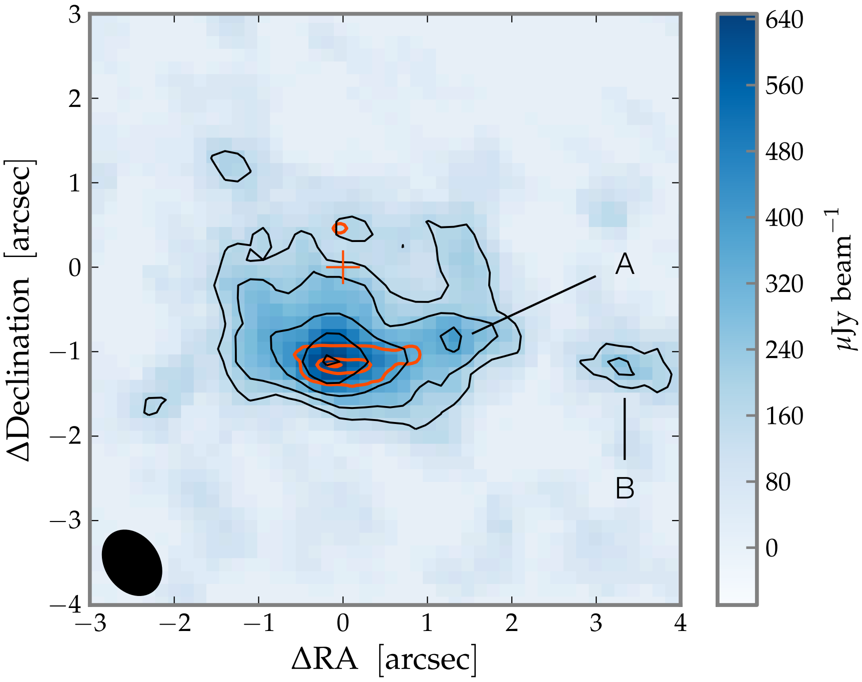

Figure 4.1: CO (1→0) intensity map of IRAS 10214 integrated over eight 42 km s^{-1} channels. *HST* rest-frame ultraviolet contours are overlaid in red and the centroid of the lens galaxy is indicated with a red cross. The CO (1→0) contours (black) are at 2-σ intervals and start at -3, 3-σ where σ = 60 μJy beam^{-1}. The synthesised beam of 0.82×0.62 arcsec^2 is shown in the bottom left corner.

Chapter 3. There is a second peak toward the west (labelled A in Fig. 4.1), either suggestive of very clumpy structure or of minor merger activity not seen in other observed parts of the spectrum (which are spatially resolved). There is an additional component (labelled B) ∼ 3.5 arcsec west of the CO peak. This appears to be real feature as it is discernible at the 2-3-σ level in three of the 42 km s^{-1} channels. More tentative is an apparent 3-σ detection of the CO counter-image, roughly co-spatial with the *HST* F814W counter-image. Although highly uncertain, a naive arc-to-counter-image flux ratio $\breve{\mu} = 7\pm^{6}_{2}$ is calculated. This is done by fitting a point spread function (PSF) to the counter-image and an elongated 2D Gaussian to the arc. The quoted uncertainty is the quadrature sum of the fitting error and flux uncertainty. As we will derive in §4.3, the most probable model (generated with the mean of each parameter's PDF) has a counter-image that is co-spatial with the *HST* F814W counter-image and not slightly west-ward as seen in the CO (1→0) total intensity map. However, this ∼100 mas offset is within the positional uncertainty of the counter-image ($\sigma_\theta = 0.5\,\mathrm{FWHM}/S/N \sim 130$ mas).

The integrated spectrum shown in Fig. 4.3 has a Gaussian-fitted mean redshift of $z = 2.28555 \pm 0.00005$

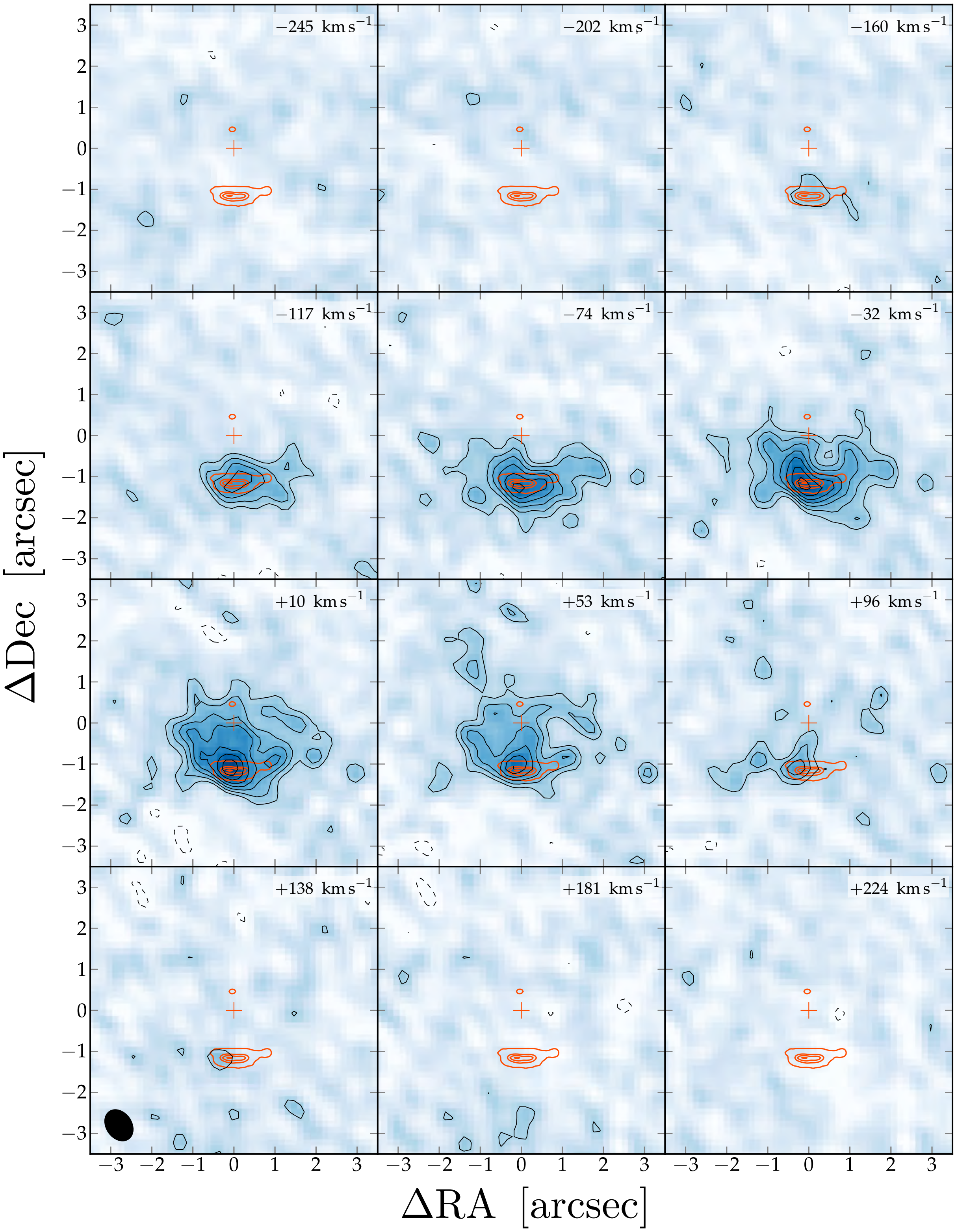

Figure 4.2: CO (1→0) channel maps of IRAS 10214. Contours are at 1-σ intervals and start at -2.5, 2.5-σ where σ = 0.17 mJy beam^{-1}. *HST* rest-frame ultraviolet contours are overlaid in red and the centroid of the lens galaxy is indicated with a red cross. The synthesised beam of 0.82×0.62 arcsec^2 is shown in the bottom left corner. Note that these channels are entirely independent (i.e. no form of Hanning smoothing was applied). The separate core we propose in §4.3.6 is most evident at velocities $V = +10$ and $+53\,\mathrm{km\,s^{-1}}$, therefore spanning $\gtrsim 80\,\mathrm{km\,s^{-1}}$.

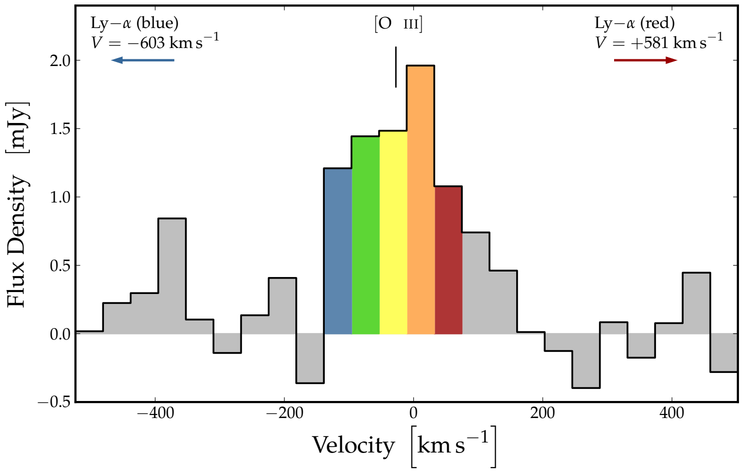

Figure 4.3: Spectrum of IRAS 10214 showing 24 × 42 km s^{-1} channels covering ∼1000 km s^{-1}. The asymmetric profile is also seen in the CO (3→2) and C I spectra reported in Ao et al. (2008). A more detailed discussion of the *Ly-α* and other spectral line velocity offsets is presented in §4.4.2 and summarised in Table 4.1.

(this excludes the Doppler tracking systematic uncertainty). We use a Markov Chain Monte Carlo (MCMC) algorithm to fit a Gaussian to the integrated spectrum in order to determine a realistic estimate of the uncertainty, and propagate these to any derived physical properties. The result is a peak intensity $S_\nu = 1.73 \pm 0.28$ mJy; velocity FWHM $V_{\mathrm{FWHM}} = 194 \pm 31$ km s^{-1}; and mean velocity $V_{\mathrm{mean}} = -14 \pm 13$ km s^{-1}. The mean velocity assumes the systemic redshift is $z = 2.2856$. If the mean velocity is fixed to zero, then there is a negligible change ($< 1\%$) to S_ν and V_{FWHM}. The velocity integrated CO (1→0) flux density is $I_{\mathrm{CO(1-0)}} = 358 \pm 80$ mJy km s^{-1}, where the uncertainty is the quadrature sum of the MCMC-derived Gaussian amplitude and FWHM uncertainty. The peak flux density S_ν and velocity FWHM V_{FWHM} are consistent with the Riechers et al. (2011a) *GBT* observation ($S_{\nu,\mathrm{GBT}} = 1.73 \pm 0.22$ mJy; $V_{\mathrm{FWHM}} = 184 \pm 29$ km s^{-1}). Our values imply $L'_{\mathrm{CO}} = 9.2 \pm 2.0 \times 10^{10}$ K km s^{-1} $\mu^{-1}_{\mathrm{CO(1-0)}}$, where $\mu^{-1}_{\mathrm{CO(1-0)}}$ is the magnification of the CO (1→0) emitting gas. The spectrum is asymmetric with a more prominent blue-wing (negative velocities). This is consistent with Ao et al. (2008) who report a similar asymmetry in the C I and CO (3→2) integrated spectra, but not in the higher-order CO lines. We do not detect any continuum emission to a 3-σ level of 90 μJy beam^{-1}. We select channels that are above 5-σ to perform a lensing analysis, which results in a total of 5 channels to investigate in the source plane.

The intensity-weighted mean, image-plane velocity map is shown in Fig. 4.4. This map was is generated

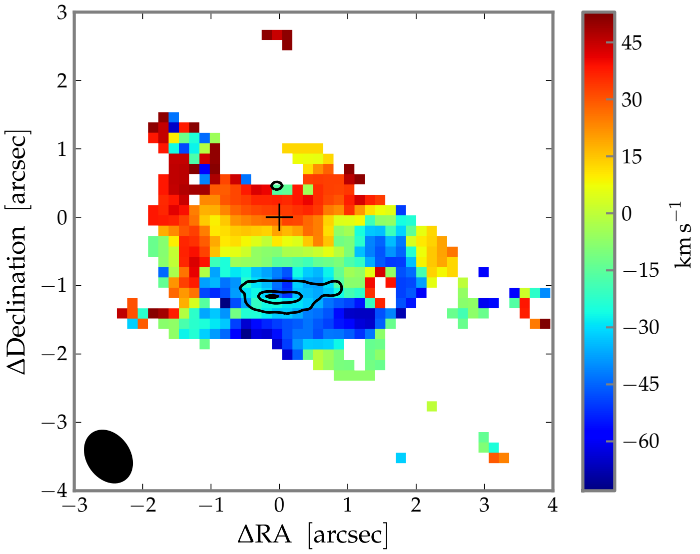

Figure 4.4: CO (1→0) intensity weighted velocity map of IRAS 10214, revealing a North-South velocity gradient. White pixels represent values outside the range shown by the colourbar. The white pixels within the velocity field in the south-west are roughly co-spatial with the secondary peak (labelled *A* in Fig. 4.1) and at a velocity of $V \sim 100$ km s^{-1}, however are not included here to better illustrate the velocity field. *HST* rest-frame ultraviolet contours are overlaid in black and the centroid of the lens galaxy is indicated with a cross.

by applying a 2-σ clip to the four channels with highest flux density in the integrated spectrum (Fig 4.3). The velocity field spans a range $\Delta V = 168$ km s^{-1} and reveals a clear North-South gradient (or NNE-SSW). Velocities outside this range are clipped and shown in white. Ao et al. (2008) mapped the CO (3→2) line towards IRAS 10214 and found a NE-SW velocity gradient. The same authors find an East-West velocity gradient C I ($^3P_2 \rightarrow {}^3P_1$), however IRAS 10214 was not resolved in the North-South direction making a direct comparison difficult. Moreover, their velocity range covered ~ 90 km s^{-1}, half of what is traced by our CO (1→0) map. Finally, the apparent second CO (1→0) peak appears to be at a higher recession velocity, as seen in the channel maps.

4.3 Source Plane Inversion

We estimate the magnification of the CO $(1\rightarrow0)$ channel maps and total intensity map using a Bayesian MCMC algorithm, previously presented in Chapter 2. For the purposes of this work, we fix the lens model parameters to those defined in Lens Model A in Chapter 2, which was derived using a deep, rest-frame ultraviolet *HST* map (F814W filter). We derive the source-plane CO $(1\rightarrow0)$ properties, given the data which are the individual channel map pixel values presented in Fig. 4.2. We include channels which have an integrated flux density with >5-σ significance. The PSF, which is well-defined in radio interferometric observations, has major and minor axis FWHM of 0.82×0.62 arcsec^2 at a position angle of 34.3° east of north. We assume spherically symmetric, Gaussian components for the CO $(1\rightarrow0)$ source model. A Gaussian profile is a highly simplified representation of high-redshift gas morphology, which observations and simulations show to be dominated by large star-forming clumps. However, this simplification has two clear advantages: (1) the lensing inversion computational requirements are drastically decreased; (2) the resultant models allow a uniform comparison (specifically of the centroid and radius uncertainties) with other CO $(1\rightarrow0)$ channels as well as the source-plane properties of other radio and optical maps reported in Chapter 3. We make the simplification that the CO $(1\rightarrow0)$ channel map noise properties are uncorrelated which is untrue. However, this is unlikely to make a large impact since each channel map has its dominant peak and arc structure reasonably reproduced, with residuals that appear to be dominated by the simplification in source-plane structure. Proper treatment of the correlated noise would be important in a pixel-by-pixel reproduction of the source-plane map, however at this low S/N the benefits of such an approach are not immediately clear. A good example of an alternative approach is that performed in Riechers et al. (2008), who model 7 independent CO (J 2-1) channel maps of the molecular Einstein ring in PSS J2322+1944 using a pixel-based source-plane reconstruction. The results do not allow the the source-plane structure uncertainties to be easily described, however it does reproduce the image-plane structure very well.

With the lens model fixed, we vary the source-plane scale radius and source centroid which are all assigned uniform priors. MCMC chains are run in the same manner as described in Chapter 2: a Metropolis-Hastings algorithm (with a Gaussian proposal distribution) is tuned to have an acceptance rate of 20%. We find convergence occurs after $\sim10^5$ iterations, however this is significantly shortened if the eigenvectors and eigenvalues are estimated (from a $> 10^5$ iteration run) and used to transform the parameter vector into

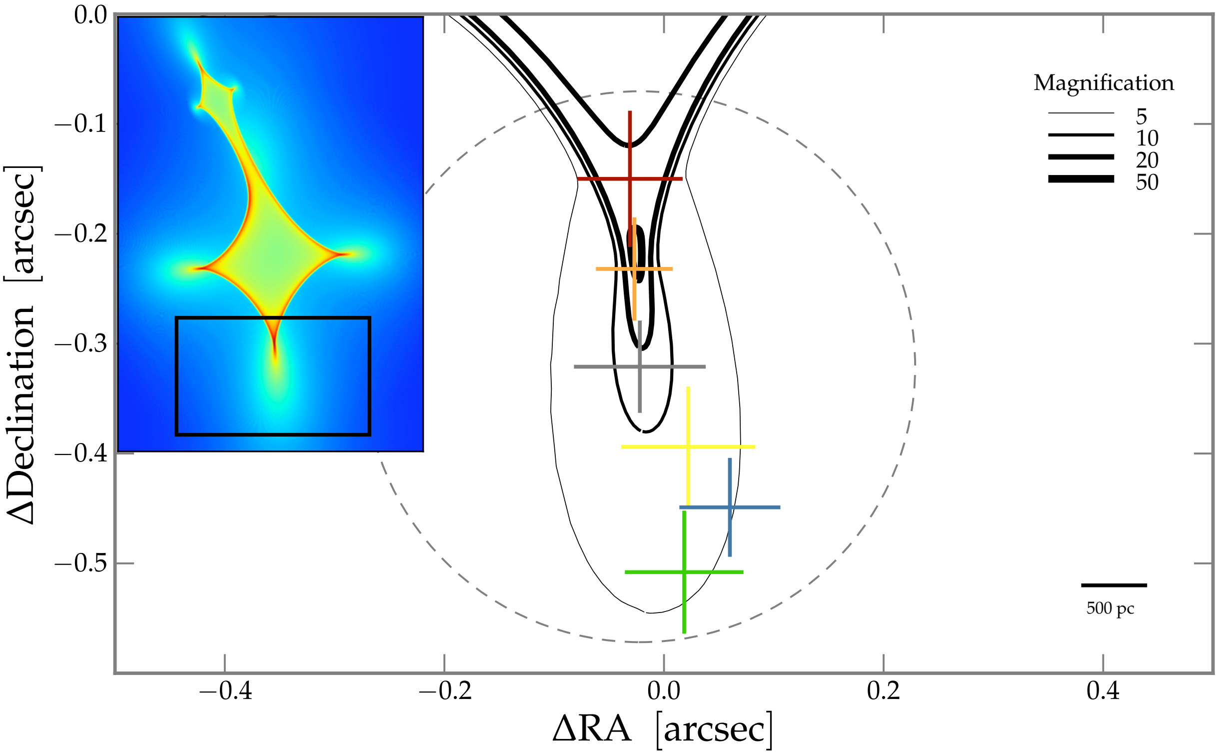

Figure 4.5: Source plane reconstruction showing the centroids of individual channel maps that have an integrated flux density >5-σ ($\sim$1 mJy beam^{-1} in a 42 km s^{-1} channel). The cross sizes indicate the MCMC-derived 68% confidence level of the source-plane centroids. The crosses are colour-coded by velocity: blue representing the most blue-shifted channel ($V = -117$ km s^{-1}) and increasing in steps of $\Delta V = 42$ km s^{-1}. The grey cross and corresponding grey dashed circle represent the best-fit model to the total intensity map (Fig 4.1), where the scale radius is $r_s = 5.8\pm^{0.9}_{0.7}$ kpc. The black lines represent contours of magnification, based on the lens model derived in Chapter 2.

uncorrelated space where proposal distributions are more efficient in achieving convergence. Our MCMC algorithm samples the unnormalised posterior PDF of the centroid RA, Dec and scale radius r_s, quantifying in the level of uncertainty of each free parameter.

4.3.1 Channel Centroid Positions

In Fig. 4.5 we plot the resultant centroid estimates of the lens inversion process. The black lines represent contours of magnification around the caustic (see legend, top right). The coloured crosses represent the mean of the centroid posterior PDF, with 68% confidence level indicated by the cross length. The colour is coded by recession velocity, starting with the most blue-shifted channel ($V = -117$ km s^{-1}) and increasing in steps of $\Delta V = 42$ km s^{-1}. This reveals a roughly linear source-plane structure, suggesting regular rotation in the disk, partially reinforced by the velocity field in Fig. 4.4. We note that these two observational results are consistent with, but not evidence for, a regularly rotating molecular gas disk. A straight line fit to the channel source-plane centroids results in a vector with a position angle $PA_{\mathrm{CO,vel}} = 16^\circ \pm 7^\circ$ east of north. We also plot the total intensity map source-plane centroid with a black cross. The dashed black circle represents the scale radius posterior PDF mean ($r_s = 5.8\pm^{0.9}_{0.7}$ kpc). This compares very well the the intrinsic size of PSS J2322+1944 (r_{eff} 5 kpc which has a similar gas mass ($M_{\mathrm{gas}} \sim 2 \times 10^{10}$ M$_\odot$) and shows evidence for a regularly rotating disk (Riechers et al., 2008).

4.3.2 Magnification

The magnification posterior PDF is sampled by computing the total magnification for each iteration of the MCMC chain. This is calculated by taking the ratio of image to source plane flux. The procedure is repeated for each channel map with an integrated spectrum flux greater than 5-σ ($\sim$1 mJy beam^{-1}), as well as the total intensity map.

In Fig. 4.6 we show the MCMC-derived magnification posterior PDFs of each of the 5 channels and the total intensity map. The latter has a mean magnification of $\mu_{\mathrm{CO}(1-0)} = 6 \pm 1.5$, which is very similar to the total magnification found for the molecular Einstein ring PSS J2322+1944 ($\mu = 5.34 \pm 0.34$), where the lensing galaxy has a slightly lower Einstein radius ($\theta_{\mathrm{E}} = 0.745'' \pm 0.024''$) than in the case of IRAS 10214's main lens. The level of preferential magnification shown here is enough to distort the integrated CO (1→0) spectrum and create the observed asymmetry. Ao et al. (2008) suggest this asymmetry is caused by a differential opacity effects for the low vs. high-J lines due to the presence of cold foreground material. We have shown in Fig. 4.5 that the red-ward channel centroids are closer to the cusp, and therefore undergo a larger magnification boost. This will contribute towards the observed asymmetry, however a differential opacity function is plausible given the expected edge-on orientation of the galaxy.

4.3.3 Gas Mass

With the magnification estimated we can now calculate the intrinsic properties of IRAS 10214. We calculate a lensing-corrected CO (1→0) luminosity of $L_{CO(1-0)} = 1.5 \pm 0.3 \times 10^{10}$ K km s^{-1} pc^2 with our derived

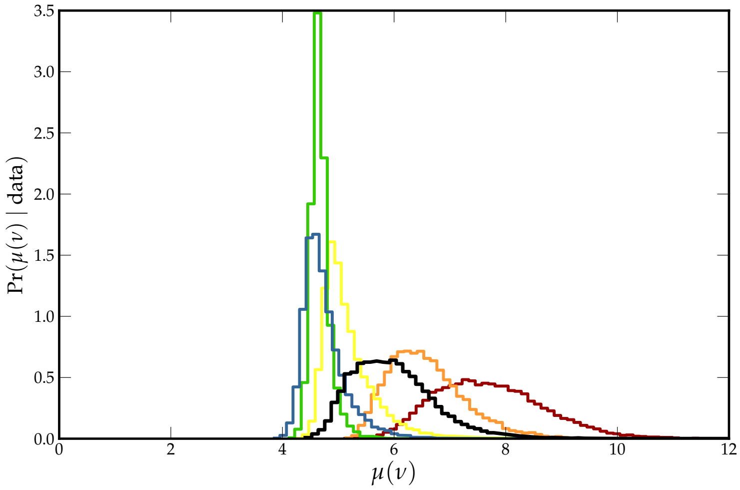

Figure 4.6: Posterior PDFs of individual channel map magnifications (colours). The posterior PDFs are colour-coded by recession velocity, starting with the most blue-shifted channel ($V = -117$ km s^{-1}) and increasing in steps of $\Delta V = 42$ km s^{-1}. The black curve represents the total intensity map magnification posterior PDF.

average magnification $\mu_{CO(1-0)} = 6 \pm 1.5$. The CO line luminosity $L'_{\rm CO}$ is directly proportional to the total gas mass through

$$M_{\rm gas}({\rm M}_\odot) \quad = \quad \alpha L'_{\rm CO}({\rm L}_\odot). \tag{4.1}$$

The conversion factor α has been determined through dynamical mass measurements in molecular cloud complexes within our Galaxy and external galaxies. The value typically ranges between $\alpha \sim 0.8 - 4.6$ ${\rm M}_\odot$ (K km s^{-1} pc^2)$^{-1}$ depending on environment. Measurements in the Galaxy are typically close to the upper bound, while a value of $\alpha \sim 0.8$ is found in ULIRGs. We adopt the latter given the infrared luminosity of IRAS 10214 ($L_{\rm FIR} \sim 10^{13}$ ${\rm L}_\odot$). This results in a gas mass $M_{\rm gas} = 1.2 \pm 0.4 \times 10^{10}$ ${\rm M}_\odot$ and implies a 65:1 gas-to-dust ratio based on the dust mass $M_{\rm dust} = 1.1 \times 10^9 \mu^{-1}$ ${\rm M}_\odot$ derived by Ao et al. (2008) and assuming equal magnifications for the both components. As we discuss later, the dust component is likely to be more compact than the total gas reservoir. As a result, emission from dust will undergo a larger magnification according to our lens model and would increase the gas-to-dust ratio by $\lesssim 100\%$. If we assume an effective radius of $r_{\rm eff} = 4$ kpc ($r_{\rm eff} \sim 0.7\, r_{\rm s}$) as derived from the lens inversion, then a gas projected surface density of $\Sigma_{\rm gas} = 240 \pm 80$ ${\rm M}_\odot$ pc^{-2} is calculated.

4.3.4 Dynamical Mass

With spatially resolved kinematics and evidence for some form of regularly rotating gas, we can make a tentative estimate of the dynamical mass. The virial theorem states that the dynamical mass $M_{\rm dyn} = V^2\, r/(\mathrm{G}\, \sin^2 i)$, where G is the gravitational constant, i is the disc inclination, V^2 is the gas velocity and r is the radius at which that velocity is measured. Caution must be stressed in this section however, since the uncertainties are large and are built on a number of assumptions. We discuss these and derive a dynamical mass inside the effective radius, $M_{\rm dyn}(r < r_{\rm eff})$, based on two methods.

Integrated Spectrum $\mathbf{V}_{\rm FWHM}$ Method

This method is based on the posterior PDFs of the measured $V_{\rm FWHM}$ of the integrated CO $(1\rightarrow0)$ spectrum; and the derived CO $(1\rightarrow0)$ effective radius based on our source plane inversion of the CO $(1\rightarrow0)$ total intensity map. We follow Daddi et al. (2010) and apply a simulation-derived correction factor that increases the dynamical mass $M_{\rm dyn}$ by 30%. This factor results from a number of both negative and positive effects including flattening of the baryonic disk, projection angle bias, non-circular gas orbits (see Daddi et al. 2010 for more detail). Like these authors, we calculate dynamical mass $M_{\rm dyn}$ inside the effective radius $r_{\rm eff}$ ($\sim 0.7\, r_{\rm s}$),

$$M_{\rm dyn}(r_{\rm eff}) \quad = \quad 1.3\, \frac{(V_{\rm FWHM}/2)^2\, r_{\rm eff}}{\mathrm{G}\, \sin^2 \mathrm{i}}. \tag{4.2}$$

We set the disk inclination $i = 90°$ for the moment, but consider a range of inclinations later. We calculate the dynamical mass, $\log(M_{\rm dyn}(r < r_{\rm e})/\mathrm{M}_{\odot}) = 10.06 \pm 0.19$ by combining the $V_{\rm FWHM}$ and $r_{\rm eff}$ posterior PDFs (i.e. $M_{\rm dyn}$ is calculated for each sample in the respective MCMC chains). Although the statistical uncertainty above is large, the systematic uncertainty is likely to dominate the error budget. We have assumed that the gas is arranged in a disk and velocities are representative of circular rotation. Furthermore, our inferred radial posterior PDF and the associated magnification (and hence radius) include significant systematics from assumptions such as a singular isothermal ellipsoid potential and the co-location of stellar and dark matter potential centroids (see Chapter 2 for a full description).

Position-Velocity Fit Method

Our second method follows the typical technique used in optical analyses of kinematics in intermediate to high-redshift galaxies (e.g. Miller et al., 2011; Swinbank et al., 2006). This collapses the map into a single spatial dimension by assuming the major axis orientation. We determine a best-fit major axis with a straight line fit to the source plane CO (1→0) channel centroids shown in Fig. 4.5. These centroids are then used to fit the position-velocity space function,

$$V = V_0 + \frac{2}{\pi} V_{\rm asyp} \arctan\left(\frac{r - r_0}{r_{\rm t}}\right), \tag{4.3}$$

where V_0 is the systemic velocity, $V_{\rm asyp}$ is the asymptotic velocity, r_0 is the dynamical centre, $r_{\rm t}$ is the turn-over radius (where the second derivative of $V(r)$ is zero). Again, we set disk inclination $i = 90^\circ$ for the moment and return to this at the end of this section. We explore the allowable parameter space with an MCMC algorithm to robustly quantify the uncertainty. We assign uniform priors to all parameters, apart from the systemic velocity for which we employ a Gaussian prior centered on $V_{\rm sys} = -14 \pm 13$ km s^{-1}, which is based on the integrated spectrum fit.

In Fig. 4.7 we show the position-velocity plot with the five source plane inverted CO (1→0) channels which are colour-coded by velocity. The uncertainties of these five points reflect the channel velocity width ($\Delta V = 42$ km s^{-1}); and the MCMC derived positional uncertainties rotated through the fitted major axis angle. Since the systemic velocity is a free parameter in the fit, we define the origin of the x-ordinate as the linearly interpolated position where velocity (relative to $z = 2.2856$) is zero. Therefore, there are no models with counter-rotation implied by Fig 4.7, it simply illustrates the range of models explored during the MCMC fitting procedure.

The black line is an *arctan* model derived from the mean of each parameter's posterior PDF. As can be seen in Fig. 4.7, we cannot make any constraints on the asymptotic velocity above $V \sim 200$ km s^{-1}, reflected in an almost uniform posterior PDF. However, some useful constraints can be made on the dynamical mass *within the effective radius*, where $r_{\rm eff} = 4.0$ kpc or 0.48 arcsec, which defines the x-ordinate limits in Fig. 4.7. We also have poor constraints on the turn-over radius but find a value $r_{\rm t} = 0.6 \pm 0.2$ arcsec (5.0±1.7 kpc) which is in the centre of the distribution of a sample of $z = 0.2 - 1.3$ star forming disk galaxies (S.H. Miller, private comm.), showing it is a plausible value given this scenario, and that the algorithm is returning sensible results despite very few data points.

Through this MCMC algorithm we are able to sample the $M_{\mathrm{dyn}}(r < r_{\mathrm{e}})$ posterior PDF by calculating the rotational velocity at the effective radius for each MCMC sample. The result has large uncertainty, however it does provide a consistency check with the Integrated Spectrum V_{FWHM} Method (§4.3.4). In Fig 4.8 we plot the dynamical mass posterior PDFs of both methods described here. The *arctan* method results in a dynamical mass $\log(M_{\mathrm{dyn}}(r < r_{\mathrm{e}})/\mathrm{M}_{\odot}) = 10.28 \pm^{0.16}_{0.48}$. The plot shows these are consistent values, albeit with considerable uncertainty.

The effect of inclination has not been included in the values quoted above. This increases the dynamical masses by a factor $1/\sin^2(i)$, so here we consider the values for $i = 90°, 60°$, and $30°$. The latter two inclinations will increase the dynamical mass by factors of 1.3 and 4 respectively. We include these possibilities in our estimation of the CO-to-M_{gas} conversion factor α in the next section. Lawrence et al. (1993) discuss limits on the disk inclination angle based on polarisation arguments which we briefly summarise here. In the case of optically thin electron scattering, they follow Brown & McLean (1977) and Miller & Goodrich (1990) and show that the observed optical/UV polarisation fraction of $> 20\%$ requires a disk inclination angle $> 40°$. In principle, optically thin electron scattering can have a polarisation fraction of 100% at a 90° inclination angle. However, dust scattering has a maximal polarisation fraction of $\sim 35\%$ according to Scarrott et al. (1990). The high optical polarisation fraction in IRAS 10214 of 28% suggests that the disk has a large inclination, however we consider inclinations of $30° - 90°$ for the remainder of the chapter.

4.3.5 Independent L_{CO}-to-M_{gas} Conversion Estimate

Since we have a dynamical mass estimate, we can estimate a range of the L_{CO}-to-M_{gas} conversion factor (α) in IRAS 10214. This is of interest since, as previously stated, this value varies by a factor ~ 6 depending on environment: $\alpha = 4.6$ in our Galaxy, while the conversion factor has been measured to be $\alpha = 0.8$ in ULIRGs. The latter is used in our gas mass estimate in §4.3.3, however if we assume a $M_{\mathrm{gas}}/M_{\mathrm{dyn}}$ fraction, we can derive an independent α estimate. We assume a dark matter fraction of 25% within the CO $(1\rightarrow0)$ effective radius (Daddi et al., 2010, and reference therein). This sub-dominance of dark matter within the

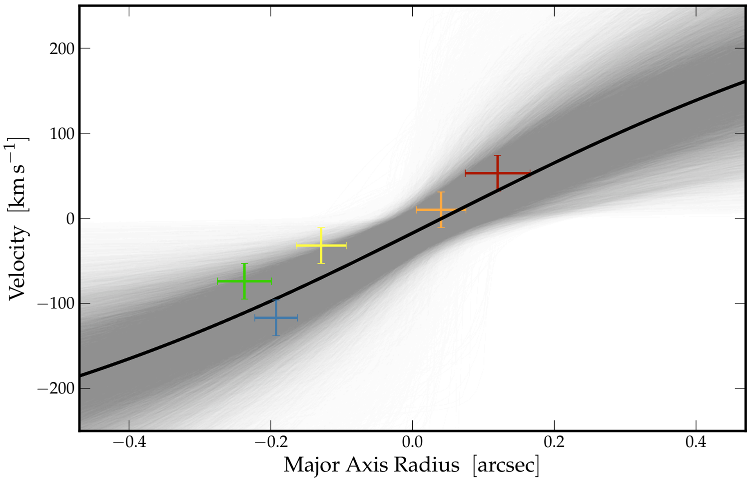

Figure 4.7: Position-velocity plot of the five channels inverted into the source plane. The data points are coloured by velocity as before. The major axis is derived from a straight line fit the source plane channel centroids plotted in Fig. 4.5 and the origin is a linear interpolation to zero velocity ($z = 2.2856$). These data are fit to the *arctan* function in Eq. 4.3. Every 50th model is over-plotted with low opacity so density is a proxy for probability and the range of models explored in the MCMC process is also captured in the plot. Note that both the dynamical centre and central velocity are varied in this MCMC algorithm, (i.e. no models with counter-rotation are implied by the figure). The velocity uncertainties represent the channel widths ($\Delta V = 42$ km s^{-1}) while the major axis uncertainties are MCMC-derived from the lensing-inversion algorithm, rotated through the major-axis position angle. The red line corresponds to the model with the mean posterior PDF of each parameter and is virtually unchanged for $V_{\rm asymp} \gtrsim 200$ km s^{-1}. See further details in text.

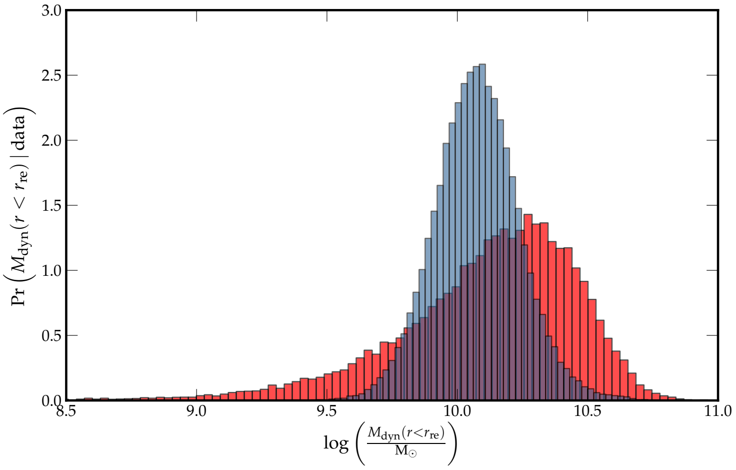

Figure 4.8: Posterior PDFs of the dynamical mass $M_{\rm dyn}(r < r_{\rm e})$ inside the effective radius as estimated by the $V_{\rm FWHM}$ fit to the integrated CO (1→0) spectrum (blue; see §4.3.4) and the *arctan* model (red; see §4.3.4).

effective radius of galaxies, particularly massive disk galaxies, is well-supported by galaxy rotation curves and strong-lensing results (Rubin et al., 1980; Treu & Koopmans, 2004). An estimate of the stellar mass is more challenging, largely due to the lack of a reliable magnification of the evolved stellar component. Lacy et al. (1998) showed evidence for a Balmer break at 4000 Å in their near-infrared spectrum, demonstrating that the host galaxy stellar light is significant at rest-frame *B*-band, however it seems clear that the near-ultraviolet is dominated by scattered quasar light based on the strong polarisation and the effect of preferential lensing. Ideally, we would make a mass estimate in the NIR, however the lens galaxy makes a substantial, yet unconstrained, contribution at this wavelength (Verma et al., 2012, in prep.). The complexities require careful, multi-component modelling that is not included this thesis. Therefore, we adopt the Daddi et al. (2010) average gas fraction ($f_{\rm gas} = M_{\rm gas}/(M_{\rm gas} + M_{\rm stellar})$) within the effective radius, measured in their sample of six non-lensed $z \sim 1.5$ disk galaxies. Their sample ranges between $f_{\rm gas} = 51 - 66\%$ with an average of $\langle f_{\rm gas} \rangle = 57\%$. Here $M_{\rm gas}$ is entirely molecular and assumes that the neutral hydrogen mass ($M_{\rm HI}$) can be neglected within the CO (1→0) effective radius(Obreschkow & Rawlings, 2009).

Following these assumptions, we calculate a gas mass in the range $M_{\rm gas,kin} = 5 - 20 \times 10^9$ $\rm M_\odot$ within the effective radius, leading to a range of $\alpha = 0.3 - 1.3$ for inclinations of $i = 90° - 30°$. This straddles the empirically derived value for ULIRGs, providing evidence that this is an appropriate conversion factor for IRAS 10214.

4.3.6 Evidence for an Extended Gas Reservoir?

As discussed earlier, observations of molecular gas in high-redshift galaxies have primarily targeted the mid- to high-*J* CO lines due to instrumentation and atmospheric window limits. At low redshift, comparisons between low and high-*J* lines have been limited for similar reasons, with high-*J* lines being the more challenging to observe in the nearby Universe. As a result, definitive comparisons have been difficult to perform which has raised concern about accurate gas mass estimation from the high-*J* line velocity-integrated intensities. This is rooted in the plausible scenario where two gas phases dominate the galaxy: (1) a higher kinetic temperature phase in the molecular cores and circumnuclear environment where the most intense star formation occurs and AGN heating takes place; (2) a lower kinetic temperature gas in the more quiescent parts of the molecular disk. Since the high-*J* lines would not be sensitive to the latter component, there could exist a large, undetected, reservoir of low-excitation molecular gas if the lowest J line luminosities are not measured. This was particularly true of IRAS 10214 given that the CO (3→2) was the lowest rotational line detected, and given the higher dust and gas temperatures in this system (e.g. Ao et al., 2008), suggesting that the mid-J lines would be heated predominantly by the AGN and most intense star formation.

The CO (1→0) detection in Riechers et al. (2011a) demonstrated that there was no *prima facie* evidence for a large gas reservoir in IRAS 10214. Our observations here spatially resolve the fundamental CO (1→0) line, providing a direct estimate of the apparent solid angle ($\Omega_{\rm app}$). This breaks the degeneracy between hydrogen column density ($n(\rm H_2)$) and kinetic temperature ($T_{\rm kin}$); and allows direct comparison with the best fitted solid angle in Linear Velocity Gradient (LVG) models (Goldreich & Kwan, 1974). In the LVG modelling, the data are the CO flux densities for different rotational quantum numbers, which provide constraints on the average gas properties of individual velocity components (i.e. the line-widths are assumed to be the result of large-scale, systematic motions, beyond plausible thermal velocities within a molecular cloud). We use the LVG modelling software developed by Christian Henkel, which is detailed in several papers (e.g. Weiß et al., 2007). We assume a single, spherically symmetric large velocity component; collision rates from Flower & Pineau des Forêts (2001) with an ortho-to-para $\rm H_2$ ratio 3:1; and a CO abundance per velocity gradient of $[\rm CO]/(dv\, dr) = 10^{-5}\,\rm pc\,(km\,s^{-1})^{-1}$. This software generates a library of line brightness temperatures for a given $\rm H_2$ density ($n(\rm H_2)$) and gas kinetic temperature ($T_{\rm kin}$). These brightness temperatures are converted to a corresponding CO line intensity (velocity integrated flux density) through the relation

$$S_{\rm CO} \;=\; \frac{2k}{c^2}\, T_{\rm b}\, \Omega_{\rm app}\, \nu_{\rm obs}^2\, (1+z)^{-1}, \qquad (4.4)$$

where $T_{\rm b}$ is the line brightness temperature, $\Omega_{\rm app}$ is the apparent (i.e. magnified) solid angle of the source and k is Boltzman's constant. Weiß et al. (2007) defined the equivalent radius r_0 assuming a uniform, face-on disk. To facilitate comparison with our source plane and image plane radii, both of which are assumed to have Gaussian profiles, we use the effective radius. Since the latter is defined as the radius within which half the total light is contained, we perform our LVG modelling by dividing the model intensities by a factor 2. The derived solid angle is then converted into an effective radius by assuming circular symmetry. We can therefore directly compare LVG output radii with the MCMC-derived CO (1→0) source-plane effective radius $r_{\rm eff}$ as well as the deconvolved image-plane effective radius $r_{\rm eff,app}$.

Equipped with the radiative transfer code; the spatially resolved CO (1→0) map; the CO ladder intensities for rotational transitions with $J_{\rm upper}$ = 1, 3, 4, 6, 7; as well as the independently derived C I and dust temperatures, we wish to ask the question: is there significant evidence for an extended halo of low excitation molecular gas? If so, can we quantify the potential total mass in this extended reservoir? We do not have sufficient constraints to fit a two-component temperature model to the CO line SED, however, we do have direct evidence that the CO (1→0) map can be broadly disentangled into two components: (1) a central, unresolved 'core' of emission which contains roughly 50% of the total CO (1→0) flux; and (2) an extended CO (1→0) emission with angular displacement greater than the CO (1→0) PSF FWHM ($\Delta\theta \gtrsim 0.7''$). The direct evidence for this is made clear through inspection and PSF fitting of the individual channel maps (Fig. 4.2).

We perform two tests to investigate if the CO (1→0) gas can be simplified in this way. In Model A we fit the CO line SED with a single temperature and find $T_{\rm kin}$ and $n({\rm H_2})$ posterior PDFs that peak at the values quoted in previous work ($T_{\rm kin} \sim 60$ K, $n({\rm H_2}) \sim 10^{3.8}$ cm^{-2}; see Ao et al. 2008; Riechers et al. 2011a). This results in an apparent effective radius $r^{\rm LVG}_{\rm eff,app} \sim 2.3$ kpc (∼0.28 arcsec), which is consistent with the constraint of the centrally concentrated CO (1→0) peak ($r_{\rm PSF} \sim 2.9$ kpc at $z = 2.3$), however it is considerably smaller than the observed CO (1→0) extent. Using the *AIPS* task `JMFIT`, we determine the deconvolved, image plane plane major and minor axes $\theta_{\rm maj}, \theta_{\rm min} = 2.7$ by 2.1 arcsec ($r_{\rm e,app} \sim 1.2$ arcsec). The approximation of the CO (1→0) map to a 2D Gaussian is likely to underestimate the complex morphology seen in Fig. 4.1, particularly since the source is dominated by the central component which is co-spatial with the most magnified region in the image plane (see Chapter 3). Even so, this is roughly a factor $5\times$ greater than the LVG derived effective radius, and therefore a factor $\sim 25\times$ greater in solid angle. Clearly the observations are inconsistent with the modelled radius.

This inconsistency, coupled with our argument that the CO (1→0) map can be decomposed into two components, motivates our second test. Model B is an exact repeat of the Model A LVG modelling, however the CO (1→0) intensity data point is halved. We argue that this will better model the most magnified region from which most of the high-*J* line emission originates. The resultant posterior PDFs of $T_{\rm kin}$, $n({\rm H_2})$, and $r_{\rm eff,app}$ for both tests are shown in Fig. 4.9. The most dramatic change here is in the inferred kinetic temperature of the single large velocity component. The constraints on this parameter drop dramatically, but now peak at 250-300 K, which is similar to the $\sim$ 200 K dust component fitted to the IR spectrum. This second dust component has substantial luminosity, comprising of 50% of the total IR luminosity (Teplitz et al., 2006; Efstathiou, 2006) which is similar to our (lensed) cold-to-warm gas ratio of 50% implied here. Note that the generated LVG library is limited to temperatures $<$ 400 K to achieve reasonable computational overheads. So the posterior probability of the second model (half CO (1$\rightarrow$0) flux density) are likely to be even lower.

In Fig. 4.10 we plot the two CO spectral line model fits, with the data points stemming from the superior higher-J observations from Ao et al. (2008) and the combined CO (1$\rightarrow$0) intensity from this work as well as the Riechers et al. (2011a) unresolved *GBT* and *JVLA* spectra. The resultant fit of the two tests can be compared in two ways: the minimum reduced-χ^2 or the MCMC chain average reduced-χ^2, where the χ^2 is generated from the residuals of the data-model comparison for all observed CO rotational lines. Model A results in a minimum reduced-χ^2 that is 50% of that achieved in Model B. However, if the average reduced-χ^2 is considered, then Model B has a 20% lower value than Test A. Ockham's Razor does not support the significance of the *minimum* reduced-χ^2, since both values (Model A and B) are well below 1 ($\chi^2_{\nu,min} \sim$ 0.1 and 0.2 respectively) showing that the data are being over-fitted. The average reduced-χ^2 values are $\chi^2_{\nu,min} \sim$ 1.7 and 1.4 respectively, suggesting that in a probabilistic sense, Model B is more consistent with the data. Note, however, that the evidence for an extended reservoir comes from the spatial information and not the quality of the LVG fit.

Given that the CO (1$\rightarrow$0) line luminosity is directly proportional to the gas mass, we can argue that roughly half the total gas mass is in the extended ($r_{\mathrm{eff,app}} \sim$ 10 kpc) emission detected in the CO (1$\rightarrow$0) total intensity map. The fraction of mass in this extended component could be even larger, since it undergoes a lower magnification boost (by a factor $\sim$2) than the compact CO (1$\rightarrow$0) core. Alternatively, the conversion factor α, of luminosity to gas mass ratio could be different in these two environments.

A more quiescent, cold gas reservoir is consistent with the C I derived gas temperature $T_{\mathrm{kin,CI}} = 45$ K, which is expected to be co-spatial with CO (1$\rightarrow$0), as has been been demonstrated in the Galactic centre and a number of nearby galaxies (e.g. Schneider et al., 2003; Israel & Baas, 2002). The co-location C I and CO (1$\rightarrow$0) in IRAS 10214 is supported by their similar line-widths, however this should be interpreted with caution given that C I is optically thin. The temperature inferred from the ratio of the two C I hyper-fine transition line luminosities is free of lensing distortions and so provides a robust estimate of the quiescent gas temperature. This is significantly lower the CO line SED fit of $T_{\mathrm{kin,CO}} \sim 60$ K and the dust temperature which is $T_{\mathrm{dust}} = 80 \pm 10$ K when fitted with a single grey-body component between 60-3000 μm (Ao et al., 2008).

So the overall picture suggests there is an extended reservoir not captured by modelling the CO line SED when just a single gas phase is considered. This decoupling of the gas into a preferentially magnified 'high-*J*' region and an extended disk of more quiescent gas is consistent with the multiple component infrared models, the C I temperature and, more generally, the recent *JVLA* observations of submillimetre galaxies (SMGs). The latter were originally thought to be intense, compact ($r_{\mathrm{eff}} \lesssim 2$ kpc) starbursts, but deep *JVLA* observations have revealed extended CO $(1\rightarrow0)$ emission (Ivison et al., 2011), just as we see in IRAS 10214. As discussed in Obreschkow et al. (2009), the ability of LVG models to model CO line SEDs with success can largely be attributed to the fact that most CO SEDs are dominated by a single gas phase. Indeed, the example of M 82 shows that different gas phases dominate in different regions in the galaxy (Weiß et al., 2005). Since IRAS 10214 shows both AGN and starburst traits at most observing frequencies it is not unexpected that the CO SED should be fitted with more than a single component. It appears that the preferentially lensed AGN region gives the higher excitation gas phase a magnification boost of order 2-3× over the lower excitation gas. Hence, we would likely fit a lower single phase gas temperature if the CO line SED were correctly de-lensed, which is consistent with the lensing independent C I temperature of $T_{\mathrm{k,CI}} = 45$ K.

These results also show how important accurate low-*J* line fluxes are in LVG modelling. In addition, they show how preferential lensing of one part of the CO line SED can dramatically change the inferred properties. This raises some concern given that most LVG modelling of high-redshift sources has been performed on lensed objects. Accurate lens models are essential to tackle these large systematic uncertainties.

A starting point to separate the effect of preferential lensing and its distortion to CO line SEDs is provided in Obreschkow et al. (2009, Sec. 3). These authors apply prescriptions of AGN and starburst heating to the excitation temperature based on semi-empirical results. This type of framework would allow the results of lensing analysis and resolved spatial information to be incorporated into LVG models.

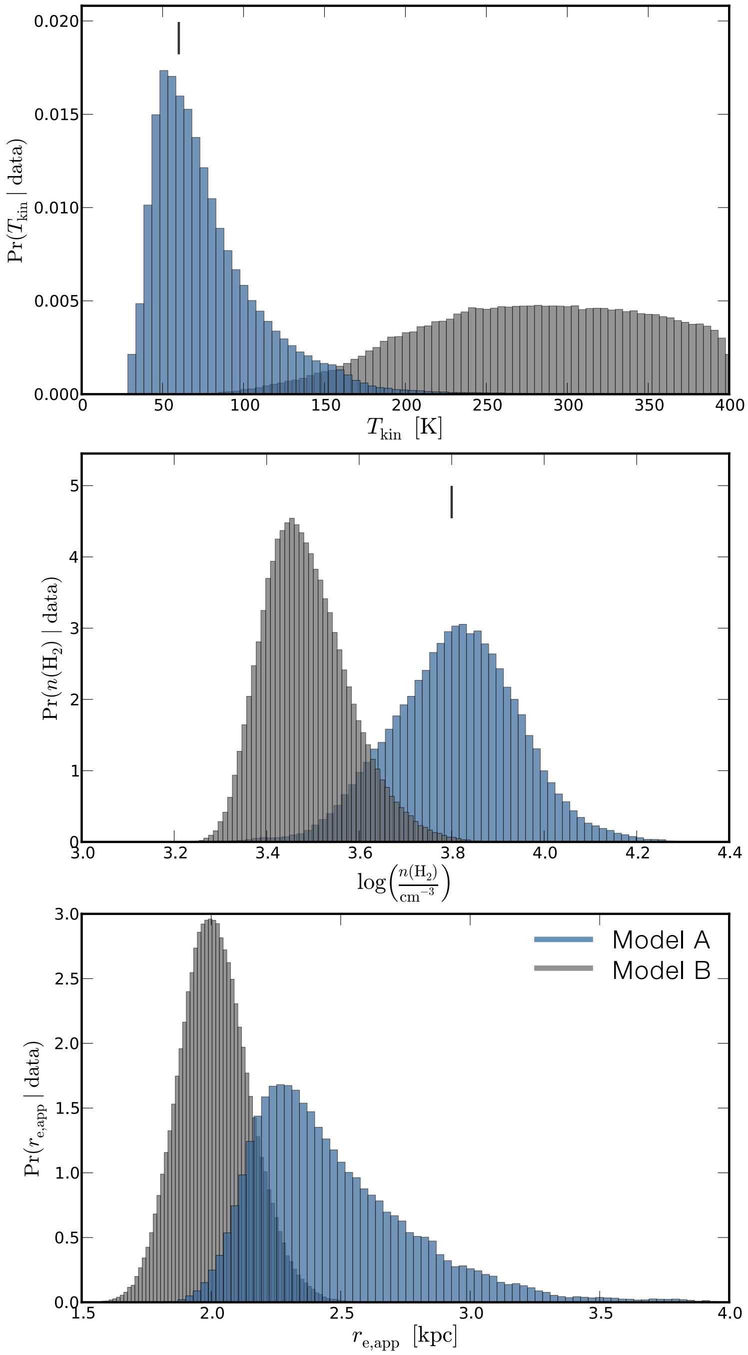

Figure 4.9: Posterior PDFs of the derived parameters from the LVG modelling for two cases. The blue PDF corresponds to the single temperature LVG model that assumes all CO (1→0) flux density is co-located with the high-*J* lines. The grey PDF assumes *half* the CO (1→0) flux density is co-located with the high-*J* lines, as evidenced by our spatially resolved CO (1→0) *JVLA* map. This results in a gas temperature for the high-*J* line gas component of $\gtrsim$250 K, consistent with the dominant hot dust component fitted in the IRAS 10214 IR spectrum (Teplitz et al., 2006; Efstathiou, 2006). The short black vertical lines indicate the quoted best-fit values for $T_{\rm kin}$ and $n({\rm H_2})$ in Ao et al. (2008) and Riechers et al. (2011a).

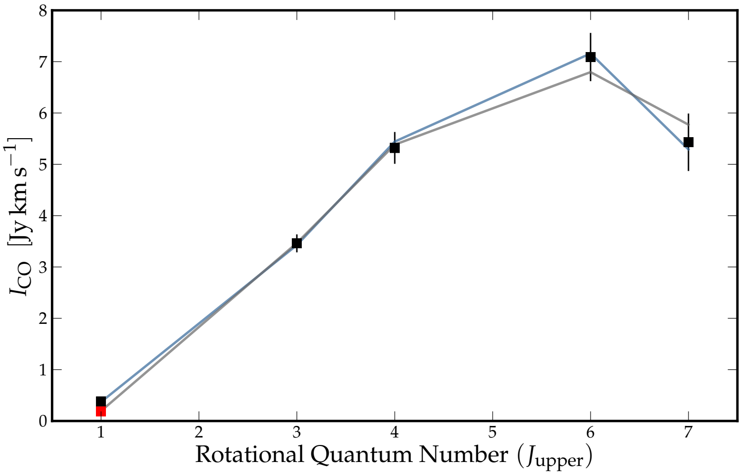

Figure 4.10: CO spectral line SED fits from LVG Model A and B (blue and grey respectively). The blue curve corresponds to the single temperature LVG model that assumes all CO (1→0) flux density is co-located with the high-*J* lines. The grey curve assumes *half* the CO (1→0) flux density is co-located with the high-*J* lines (see resultant red CO (1→0) data point), as evidenced by our spatially resolved CO (1→0) *JVLA* map. This small change demonstrates the importance of accurate low-*J* intensity measurements as shown in Fig. 4.9.

4.4 Discussion

4.4.1 General

This resolved CO (1→0) map contributes significantly to the overall understanding of IRAS 10214. The total intensity and velocity field maps reveal some evidence for ordered rotation on a ∼5 kpc scale. These two maps simultaneously show evidence for some merger activity based on the secondary CO (1→0) components (*A* and *B* in Fig. 4.1) and the higher velocity associated with component *A* in the velocity field (Fig. 4.4). Merger traits are typical of high-redshift ULIRGs, however no other wavelength has provided direct evidence of merger activity in IRAS 10214 to date.

A source-plane reconstruction of five individual channel maps reveals a relatively linear orientation of their true centroid positions, consistent with the suggested regular rotation from the velocity field. The previously derived positions of the AGN core and NLR lie in the centre of this CO (1→0) source plane structure (Fig. 4.5). The magnification posterior PDFs show appreciable (factor ∼2) preferential magnification of certain individual channels with respect to each other. The overall CO (1→0) magnification indicates the starburst in this galaxy is significantly less magnified than the AGN and narrow-line region as probed by the *HST* and radio maps in Chapter 3. This preferential magnification is greater than a factor 3 in the case of the narrow line region where we expect hot dust $T_{\rm dust} \sim 200-600$ K to be located. This is the likely explanation of the lack of PAH features in the mid-IR *Spitzer* spectrum, which would be dominated by hot dust continuum emission under our preferential lensing scenario. Teplitz et al. (2006) suggest that preferential magnification of the AGN by a factor $\sim 3\times$ could suppress these PAH features, in line with the level we determine here.

The integrated CO (1→0) spectrum is asymmetric with a more prominent blue-wing as seen in the CO (3→2) and C I spectra, but not in the higher-J CO lines. This could be as a result the preferentially lensed red-ward channels. If one assumes a mean redshift from the NLR, then there is some evidence here for direct shadowing of the lower-J CO lines. Shadowing is the direct overlap in space and velocity of individual molecular clumps of scale $r_{\rm clump} \sim 1$ pc (see e.g. Bally et al., 1987). Indeed, the reason that CO luminosity is used as a linear tracer of the total gas mass, despite the fact that it is optically thick, is because these individual molecular clumps are assumed not to overlap based on Galactic and nearby galaxy observations (Genzel & Stutzki, 1989). The higher densities observed in high-redshift galaxies will result in larger shadowing of individual clumps as discussed in Obreschkow et al. (2009), particularly if the molecular gas is oriented in an inclined disk, as is quite likely the case in IRAS 10214. It could be argued that if the individual clumps are simplistically split into 'cold' and 'warm' clumps, corresponding to low- and high-J dominated clumps, then the shadowing for low-J emission is likely to be larger given that high-J clumps would be more clustered around the AGN and the putative circumnuclear starburst. Again, the asymmetric integrated spectra of the CO lines from $J_{\rm upper} = 1$ to 7 are consistent with this assertion, however, it is contaminated by the preferentially lensed red-wing and limited by poor signal-to-noise.

Despite all of the above uncertainties, our derived estimate of the CO luminosity to gas mass ratio has a mean consistent with the value derived for nearby ULIRGs of $\alpha \sim 0.8$. This builds a picture of consistency amongst high-redshift ULIRGs as well as a vote of confidence in the source-plane reconstruction.

4.4.2 Redshifts

In Table 4.1 we collate a number of redshifts from the literature. We select the highest S/N detections of lines that can be approximated to trace specific physical components. It appears that the canonical redshift of $z = 2.2856$ is the most accurate and least biased measurement. This is based on the averaged CO spectrum which is consistent with all the molecular line redshifts and the NLR tracers which have blueshifts. The [O III] line is centered at $V_c = -36$ km s^{-1}, while the blue- and redshifted *Ly-α* components are symmetric around the molecular gas at velocities of $V_{Ly-\alpha,\mathrm{blue}} = -603$ km s^{-1} and $V_{Ly-\alpha,\mathrm{red}} = +581$ km s^{-1} respectively. The two *Ly-α* components have comparable flux (the blue component is fractionally greater), suggesting that these are mirrored components of a resonantly scattered *Ly-α* line centered at $z = 2.2856$. At face value, this is supported by a 1:1 [O VI] doublet ratio, however, it implies exceptionally large densities that are only found in the broad-line region. The most probable explanation for the unlikely [O VI] doublet ratio is significant contamination by *Ly--β* absorption as discussed in Chapter 3 and detailed in Serjeant et al. (1998). If these are indeed the resonantly scattered *Ly-α* wings, we can estimate the hydrogen column density (N_H) required to create the observed velocity offset of each peak through Neufeld & McKee (1988, Eq. 1),

$$\left(\frac{V_\mathrm{d}}{\mathrm{km\,s^{-1}}}\right) = 195\left(\frac{N_\mathrm{H}}{10^{20}\,\mathrm{cm^{-2}}}\right)^{\frac{1}{3}}\left(\frac{T}{10^4\,\mathrm{K}}\right)^{-\frac{1}{6}} \tag{4.5}$$

where V_d is the observed velocity offset of a *Ly-α* peak, T is the gas temperature, which we assign the average kinetic temperature $T_\mathrm{kin,CO} = 60$ K, determined by the CO line SED (this work and Ao et al. 2008). This results in a hydrogen column density $N_\mathrm{H} = 4 \times 10^{22}$ cm^{-2}. This can be considered a rough lower limit given the weak dependence on gas temperature and considering that the emergent *Ly-α* emission is likely to be anisotropic with greater prominence along the jet axis. As a result, the measured velocity peak position may have an inclination dependence. This does not imply that $N_\mathrm{H} \propto \sin^3(i)$, however it does suggest that the inferred hydrogen column density should increase if any anisotropy exists.

The line-width of the higher-*J* CO (7→6) line is larger than the lower-*J* CO (1→0) and CO (3→2) lines. Naively, we might expect the opposite if AGN heating contributed to the higher-*J* line flux densities. Moreover, in a system not entirely disrupted by a major merger, we would expect the most dense star-forming regions to be concentrated in the galaxy centre. These two effects would lead to larger line-widths for the more extended, colder gas since our dynamical modelling shows that the CO (1→0) effective radius is well within the radius at which the rotation velocity flattens. However, this is subject to opacity of the

Component	**Tracer**	**Redshift**	**Uncertainty**	**Velocity**† km s^{-1}	V_{FWHM} km s^{-1}	**Reference**
BLR	C IV (polarised)	2.2790	-	-603	6000	Goodrich et al. (1996)
BLR	C IV	2.2833	-	-210	1100	Goodrich et al. (1996)
NLR	[O III]λ5007	2.2853	0.0001	-36	1040	Lacy et al. (1998)
NLR (?)	*Ly*-α (blue-wing)	2.2790	0.001	-603	0-900	Lacy et al. (1998) (double Gaussian)
	Ly-α (red-wing)	2.2920	0.001	+581	0-600	Lacy et al. (1998) (poor fit)
Dense Gas	HCN (1→0)	2.2858	0.0002	+18	140±30	Vanden Bout et al. (2004)
	C I ($^3P_2 \rightarrow {}^3P_1$)	2.2854	0.0001	-18	182±30	Ao et al. (2008)
	C I ($^3P_1 \rightarrow {}^3P_0$)	2.2854	0.0001	-18	160±30	Weiß et al. (2005)
Warm Gas	CO (7-6)	2.28534	0.00005	-24	248±30	Ao et al. (2008)
	CO (3-2)	2.28535	0.00005	-23	199±13	Ao et al. (2008)
Cold Gas	CO (1→0)	2.28554	0.00005	-14	194±31	this work
	CO (1→0)	2.2856	0.0001	0	184±29	Riechers et al. (2011a) (*GBT* values)
Average CO	⟨CO (7-6,6-5,4-3,3-2)⟩	2.28562	0.00004	0	246±10	Ao et al. (2008)

Table 4.1: Redshifts of Physical Components in IRAS 10214.
†Relative to the systemic velocity assumed here, $z_{\mathrm{sys}} = 2.2856$, derived from the average integrated CO spectrum in Ao et al. (2008) which has the lowest uncertainty of all redshift determinations, however does not include Doppler tracking uncertainties.

respective CO lines as well as the fact that line-widths are potentially influenced by the more complex conditions found at higher densities and temperatures near the active core. This is particularly true if jet outflows are present, evidence of which was presented in Chapter 3.

The two hyperfine C I lines have velocity widths more consistent with the lower-J lines, suggesting these trace similar physical regions. This is supported by the integrated spectrum asymmetry seen in the CO (1→0) , CO (3→2) and C I ($^3P_2 \rightarrow {}^3P_1$) lines, but not in the higher-J lines. This assumes that the emission from all CO lines is optically thin which is not true, however the emission can be treated as such since there is minimal overlap (i.e. shadowing) of individual molecular clouds (Obreschkow et al., 2009). It is somewhat speculative to go into further detail since the effect may be a signal-to-noise artifact since the higher-J lines have significantly higher flux densities. Higher sensitivity, spatially-resolved observations are required – a realm for next-generation facilities such as the *Atacama Large Millimetre/Submillimetre Array (ALMA)*, and the *Square Kilometre Array (SKA)*.

4.4.3 IRAS 10214 as an Archetype ULIRG

The source plane structure shows that if higher-J CO lines are confined to smaller solid angles around the AGN core (as we would expect since the high temperatures require AGN heating) then the CO line spectral energy distribution will be significantly distorted, with higher-J lines undergoing magnifications that are 2-3× larger than the CO (1→0) by virtue of their size and proximity to the caustic. Further indirect evidence for preferentially lensed high-*J* lines and dust are the differences in dust and gas temperatures measured in Ao et al. (2008), which are plausible if these regions are confined to smaller solid angles in close (<1 kpc) proximity to the AGN. The same authors also find that the 1.3 mm continuum emission region is smaller in size than the CO (3→2) , suggesting some AGN heating contribution.

Since IRAS 10214 is frequently used an archetype ULIRG for comparisons of mid-IR spectra, CO line SEDs and infrared luminosities, we argue this is not a sound choice until the function $\mu(\nu)$[1] has been defined for each wavelength of interest. This strongly motivates detailed comparison analyses of non-lensed objects (e.g. Schumacher et al., 2012) in parallel with the sensitivity-enhanced observations that strongly-lensed systems offer. *ALMA* will be an essential tool in high resolution mapping of higher-*J* lines in both lensed (and non-lensed) high-redshift galaxies, and so probe the magnification distortion of the CO spectral line SED. This is particularly relevant to the recently discovered *Herschel* lenses (Negrello et al., 2010) which were FIR-selected and expected to be dominated by starbursts. Disentangling the AGN from these objects is a clear niche for *e-MERLIN*, *ALMA* and the *JVLA* as we enter in an era where we are able to spatially separate the AGN and star formation components in large samples of high-redshift galaxies – a crucial probe of the interaction of these two components at cosmologically significant epochs. However, competitive angular resolution and sensitivity to observe the fundamental CO (1→0) line at high redshift may eventually need the *SKA* (Obreschkow et al., 2011).

4.5 Conclusions

We have performed deep *JVLA* *Ka*-band observations centered on the CO (1→0) line towards IRAS 10214, a $z = 2.3$, gravitationally lensed ULIRG harbouring a hidden quasar. We spatially and spectrally resolve the CO (1→0) emission in IRAS 10214 and use our previously derived lens model to invert five CO (1→0) channels into the source plane. We make the following conclusions.

1. Our CO (1→0) map reveals a clear arc-like structure that is co-spatial, but considerably larger than the *HST* -traced emission (in all optical/near-infrared filters).

---

[1] Lensing is effectively chromatic, since different emission components dominate different regions of global SED, and these components have differing positions and sizes. The function $\mu(\nu)$ is essentially the mean magnification of the dominant emission components at a given frequency.

2. We measure a lensing corrected CO (1→0) luminosity of $L'_{\rm CO} = 1.5 \pm 0.3 \times 10^{10}$ K km s^{-1} pc^2 which implies a total gas mass $M_{\rm gas} = 1.2 \pm 0.4 \times 10^{10}$ M$_\odot$, if we assume the standard CO luminosity to gas mass conversion factor in ULIRGs ($\alpha \sim 0.8$).

3. There is a 3-σ CO (1→0) counter-image detection that is co-spatial with counter-images seen through the same *HST* filters. This leads to a CO (1→0) arc to counter-image flux ratio of $\breve{\mu} \sim 7 \pm^{6}_{2}$.

4. The intensity weighted mean velocity field reveals some order, suggestive of regularly rotating gas with a FWHM ~190 km s^{-1}. However, the total intensity map does suggest minor merging activity may be present or a complex morphology. This is in contrast to the to major mergers observed in other high-redshift ULIRGs as evidenced by chaotic *HST* morphologies and CO velocity widths of 500-1000 km s^{-1} (e.g. Frayer et al., 2000; Greve et al., 2005; Le Fèvre et al., 2000).

5. Based on our source plane inversion of 5 channels, we estimate a dynamical mass range within the CO (1→0) effective radius. Our independent estimate of the CO luminosity to gas mass conversion factor α gives a range $\alpha = 0.3 - 1.3$ for inclinations of $i = 90° - 30°$, straddling the typical ULIRG value of $\alpha = 0.8$.

6. We find considerable (~2×) preferential lensing between certain individual CO (1→0) channels, a possible source of the integrated spectrum asymmetry also seen in the CO (3→2) and C I integrated spectra. This asymmetry is not seen in the higher order CO rotational lines. This could arise if the higher-*J* lines have very similar magnifications across their velocity range or if there is a differential opacity between different CO lines.

7. The CO (1→0) map is a factor 3 less magnified than NLR component as presented in Chapter 3. This suggests that alongside large distortions to the global SED, there is also a likely distortion to the CO spectral line SED. Since IRAS 10214 is often used as an archetype ULIRG, we suggest that it can not be treated as such until the spectral distortion (i.e. the function $\mu(v)$) has been fully characterised.

8. The CO (1→0) emission can plausibly be divided into two components: a compact ($r_{\rm eff,app} < 3$ kpc) component associated with the higher-*J* lines based on the LVG modelling; and an extended, lower temperature component co-spatial with the C I emission. This second component either houses ~50% of the total gas mass; has a very low filling factor ($\lesssim$0.1); or has a different CO-to-H_2 conversion ratio.

Strong gravitational lensing provides us with our deepest views in galaxy structure and evolution. However, there are clearly still some challenges associated with using these cosmic telescopes. The combination of *ALMA*, the *JVLA* and *e-MERLIN* will play an invaluable role in investigating the distorted continuum and spectral line SEDs in high-redshift lensed galaxies, in particular the FIR-selected sample discovered by the *Herschel Space Observatory* (Negrello et al., 2010). These are essential steps in our understanding of the high-redshift Universe and in particular the co-evolution accreting super-massive black holes with galaxy wide star formation.

CHAPTER 5

VLBI OBSERVATIONS OF THE RADIO CORE

R.P. Deane, S. Rawlings, M.A. Garrett, I. Heywood, M.J. Jarvis, H.-R. Klöckner, P.J. Marshall, J.P. McKean
"The preferentially magnified active nucleus in IRAS F10214+47: III. VLBI observations of the radio core"
MNRAS, submitted

This chapter reports 1.7 GHz Very Long Baseline Interferometry (VLBI) observations of IRAS FSC10214+4724, a lensed $z = 2.3$ obscured quasar with prodigious star formation. We detect what we argue to be the obscured active nucleus with an effective angular resolution of < 50 pc at $z = 2.3$. The $S_{1.7} = 210\,\mu$Jy (9-σ) detection of this unresolved source is located within the *HST* rest-frame ultraviolet/optical arc, however, $\gtrsim$100 milli-arcseconds northward of the arc centre of curvature. This leads to a source plane inversion that places the *EVN* detection to within milli-arcseconds of the modelled cusp caustic, resulting in a very large magnification (μ $\sim$70), over an order of magnitude larger than the CO (1$\rightarrow$0) derived magnification of spatially resolved *JVLA* map, using the same lens model. We show that apart from the counter-image, there are unlikely to be additional images of the *EVN* detection (to 4.5-σ significance). This rules out previous suggestions that the *HST* arcs are merged images and supports the view that the observed structure along the *HST* arcs is intrinsic and *not* induced by the lensing optics. This observation therefore corroborates our previously derived lens

> model that found an arc/counter-arc to be the most probable image-plane lensing configuration. We estimate quasar bolometric luminosity from a number of independent techniques and with our X-ray modelling we find evidence that the AGN may be Compton thick, with an intrinsic bolometric luminosity $\log_{10}(\langle L_{\mathrm{bol,QSO}}\rangle/\mathrm{L}_{\odot}) = 11.34 \pm 0.27$ dex. We make the first black hole mass estimate of IRAS 10214 and find $\log_{10}(M_{\mathrm{BH}}/\mathrm{M}_{\odot}) = 8.36 \pm 0.56$ which suggests a low black hole accretion rate ($\lambda = \dot{M}/\dot{M}_{\mathrm{Edd}} \sim 3\,\pm^{7}_{2}\,\%$). We find evidence for a $M_{\mathrm{BH}}/M_{\mathrm{stellar}}$ ratio that is 1-2 orders of magnitude larger than that of submillimetre galaxies (SMGs) at $z \sim 2$. At face value, this suggests IRAS 10214 has undergone a different evolutionary path compared to SMGs at the same epoch. A primary result of this work is the demonstration that emission regions of differing size and position can undergo significantly different magnification boosts (> 1 dex) and therefore distort our view of high-redshift, gravitationally lensed galaxies.

High resolution radio imaging provides a direct method of disentangling the AGN and star formation components through the measurement of brightness temperature and the radio spectral index. This was demonstrated by Klöckner et al. (2009) who showed a sample of eleven $z \gtrsim 2$ obscured quasars to be radio intermediate luminosity quasars ($L_{5\mathrm{GHz}} = 10^{23-24}\,\mathrm{W\,Hz^{-1}\,sr^{-1}}$), a challenging observation for VLBI arrays. Until mid-way through the last decade, VLBI was an observational technique used exclusively to detect bright (> 10 mJy) radio sources which could be self-calibrated to improve the image quality and dynamic range. However, due to a confluence of factors - technical and scientific - VLBI has entered the sub-mJy domain.

In this chapter, we exploit the unique advantage of VLBI observations to filter the high brightness temperature emission at milli-arcsecond scales and constrain the active core flux and position in a high-redshift, gravitationally lensed obscured quasar. An essential ingredient in galaxy evolution theory is the role of black hole activity in regulating star formation processes (e.g. Hopkins et al., 2006). While large-scale VLBI surveys will only be possible with the full *Square Kilometre Array (SKA)*, current studies of individual systems (particularly lensed systems) provide a preview of the type of science that will be possible with a large sample size in a decade. A larger sample of unlensed systems from the *Herschel ATLAS* catalogue (Eales et al., 2010) are midway through dual-frequency observations (Virdee 2012, in prep.). This latter study is important since it is free from any magnification bias and preferential magnification effects.

In this chapter we focus on the AGN properties of IRAS 10214. Previous observations have provided strong evidence for an obscured quasar, including polarised broad emission lines and highly polarised UV/optical continuum emission (e.g. Lawrence et al., 1993; Goodrich et al., 1996; Nguyen et al., 1999). However, the obscured nature of this quasar makes it challenging to disentangle its emission from that of the host galaxy, and reliably correct for extinction. Nguyen et al. (1999) have arguably provided the best localisation of the AGN in IRAS 10214 through their spatially-resolved *HST* polarimetry. Based on the smooth polarisation position angle variation along the ultraviolet arc, and the larger arc-to-counter-image flux ratio (and magnification by proxy), they constrained the distance to the source of UV photons to be $<$160 pc, assuming a range of magnifications from μ = 250 to 45, and therefore scattering source sizes of D = 40 to 100 pc[1] They predicted the AGN was north-west of the ultraviolet source based on the distance argument and the flux-weighted mean polarisation angle. X-ray observations did not confirm the X-ray luminosity expected in IRAS 10214, based on the [O III]5007λ luminosity (Alexander et al., 2005; Iwasawa et al., 2010). These authors concluded that the X-ray emission associated with IRAS 10214 was either dominated by an dust-enshrouded starburst or that the active nucleus was Compton thick ($\sigma_{\mathrm{T}} \gtrsim 10^{24}$ cm^{-2}). In light of these challenges, we carried out VLBI observations which are unaffected by dust extinction and able to isolate high brightness temperature emission originating from an active radio core. Building on the previous multi-wavelength work and incorporating the unique characteristics of VLBI observations, the aims of this chapter are threefold:

1. Detect the obscured active nucleus in a $z \sim 2$ radio quiet quasar and hence estimate its contribution to the total radio flux.
2. Use the position to determine the AGN core magnification. This is part of a wider case study of this high-redshift galaxy which also aims to quantify the scale of preferential lensing in this system. That is to say, the level of distortion in the spectral energy distribution (SED) that occurs due to different physical emission regions undergoing different magnification boosts. This is important in demonstrating the level of effective 'chromacity' in strong gravitational lensing which affects inferred physical interpretations of these systems.
3. VLBI imaging has the potential to solve a question that arose following the high resolution *HST*

---

[1] We repeat these calculations in §5.3 with our updated magnifications derived from Lens Model A.

imaging (Eisenhardt et al., 1996; Nguyen et al., 1999; Evans et al., 1999): is the UV/optical/NIR arc in this system a single image, or three images that are unresolved by the *HST* spatial resolution. The root cause of this debate stems from the two apparent peaks along the *HST* F814W and *HST* F437M arcs which could be intrinsic source structure (i.e. clumpy UV emission as is typically observed in high-redshift galaxies), or multiple, partially resolved images.

5.1 Observations

5.1.1 EVN 1.7 GHz

Observations of IRAS 10214 were made with the *EVN* at 1.66 GHz on 2 and 3 November 2010. Stations that were used in these observations included Jodrell Bank (76-metre), Westerbork Radio Synthesis Array (WRST, phased array), Effelsberg, Onsala (26-metre), Medicina, Torun, Cambridge, Knockin, as well as the three Russian out-stations: Svetloe, Zelenchuk and Badary. This resulted in a baseline coverage of roughly 100 km to 5000 km, corresponding to an angular scale range of 500 mas to 10 mas at an observing frequency of 1.66 GHz. It is for this reason that VLBI observations apply a brightness temperature filter which enables the unambiguous determination of the active core radio flux - one of the primary aims of this work. Observations were carried out with a 1024 Mbit/s recording rate in the standard continuum observing mode, employing eight 16 MHz sub-bands in each hand of polarisation with 2-bit sampling. The total bandwidth of 128 MHz was centred on 1.65899 GHz. Each sub-band was split into 32 channels of 500 kHz width. The integration period was set to 4 seconds. This results in a time- and bandwidth-smearing limited field-of-view of 0.24 and 0.34 arcmin^2 respectively. This is based on a metric that measures the angular displacement from the pointing centre at which a 10% loss in the response to a point source is measured. These effective fields of view are larger than the optical/IR and molecular extent of IRAS 10214 by two orders of magnitude.

The total duration of the observations was 18 h, of which roughly 70% was spent on the target. The observations were split into two 9 hr runs that were performed on consecutive days. Given the IRAS 10214 1.7 GHz flux density of $S_{1.7} \sim 1$ mJy, as measured in Chapter 3, the phase referencing technique was required. Through a separate *EVN* calibrator search (described below) we selected the $S_{1.7} \sim 70$ mJy source $J1027{+}474$ as the best possible phase calibrator for IRAS 10214 given its small angular separation of

$\Delta\theta \sim 34$ arcmin. IRAS 10214 was observed for 8 min every 10 min, alternating with the phase calibrator. There was an additional cycle where the standard *VLBA* phase calibrator (*J* 1027+4803) was observed for 4 min every hour. This was done to monitor the applied phase corrections and to check the resultant astrometric accuracy. 4C39.25 was observed as a fringe-finder. Since the observation was split into 2×9 hr tracks; and the *EVN* has limited north-south coverage; the resulting beam pattern has a large ripple in the North-South direction (evident in Fig. 5.1).

Preliminary calibration of the *uv*-data set was carried out with the *EVN* automatic pipeline. This pipeline is written in Parseltongue (Kettenis et al., 2006), a high-level environment/interface for *AIPS*, and performs initial fringe-fitting (calibration of delays, rates and phase), and phase and amplitude calibration. The latter are derived from system temperature measurements at individual stations. Following this preliminary calibration, a more detailed, manual calibration is performed in *AIPS*. This was performed in a cyclic process with detailed data editing, refined delay and rate calibration, as well as phase and amplitude self-calibration on the phase reference sources. Unfortunately, the majority of the observation on the second day was lost due to a combination of circumstances including strong winds, radio frequency interference (RFI), as well as the lack of several stations which did not take part (Effelsberg, Torun).

All imaging was performed with the *AIPS* IMAGR task with a natural weighting scheme applied to the *uv*-data. Only after several rounds of the phase and delay calibration cycle (performed on the phase calibrator) did the noise level decrease to $\sigma \sim 23\ \mu\mathrm{Jy\,beam}^{-1}$ for a *uv*-range limited between 0 - 5 Mλ. Including longer baselines (>5 Mλ) improves the noise marginally (20%) however it results in large and small-scale features that decrease the overall fidelity of the IRAS 10214 map. The reason for this decrease in image quality is due to the fact that the phase calibrator is spatially resolved on the longest baselines, leading to poor phase solutions. For this reason we only consider baselines for which the phase calibrator is clearly unresolved (0 - 5 Mλ).

The measured absolute position of the standard *VLBA* calibrator *J* 1027+4803 is within $\Delta\theta < 0.80$ mas of its cataloged position. This was true for the preliminary pipeline calibration and for the manual delay and self-calibration performed in *AIPS*. The catalogue position uncertainties are (ΔRA = 0.28 mas, ΔDec = 0.43 mas), sourced from the International Celestial Reference Frame (ICRF-2). These two positions are consistent to within the sub-milliarcseond level, greatly exceeding the level of accuracy required in this work. The integrated flux density of *J*1027+4803 ($S_{\rm int} = 149 \pm 2$ mJy) is consistent with that derived by Helmboldt et al. (2007) with their *VLBA* 5 GHz observations ($S_{\rm int,5GHz} = 149.3 \pm 0.2$ mJy). VLBI resolution *L*-band observations of *J*1027+4803 have not been performed before prior to this work, so no direct flux density comparison is possible.

In addition, the radio coordinate reference frame must be directly compared to the optical reference frame. This has been performed by Lawrence et al. (1993) who compare the optical and radio positions of 20 compact radio sources in the region around IRAS 10214. They find no significant mean difference, however, they note the error on the mean difference is 0.2 arcsec which we take as the systematic uncertainty in the radio-optical co-ordinate system alignment. Since we use the same data, and our calibrators (as well as the 8 GHz centroids) are consistent, we assume have an equivalent astrometric matching between radio and optical reference frames.

Phase Calibrator Search

Experience has shown that successful phase referencing of very faint sources with the *EVN* requires a very nearby phase calibrator source ($\Delta\theta < 1^\circ$). To maximise our ability to monitor the phase distortions towards the target source, we performed a short (2×2 hr) phase calibrator search at 1.7 GHz and 5 GHz on 10 June 2010 and 30 March 2010, respectively. We observed nine target sources in a region within 1° of IRAS 10214. Three selection cuts were applied to select these nine potential phase calibrators. Targets required a *VLA* FIRST[2] peak flux density $S_{\rm peak} > 25$ mJy; a PSF-convolved major axis $f_{\rm maj} < 6$ arcsec from the same survey; and a radio spectral index $\alpha_{330}^{1.4} < 0.6$ between $\nu = 300 - 1400$ MHz, as derived from the FIRST flux densities at 1.4 GHz and our *GMRT* 330 MHz observation of the same field (see Chapter 3). Three of the nine targets showed compact emission above the ~ 10 mJy level required to be detected on most of the *EVN* baselines at a significance appropriate for phase referencing. Of the three sources, *J*1027+474 was deemed the most appropriate with an VLBI flux density of $S_\nu \sim 70 - 80$ mJy at 1.7 and 5 GHz; and an angular offset $\Delta\theta = 33.9$ arcmin from IRAS 10214.

---

[2] Faint Images of the Radio Sky at Twenty-cm; see http://sundog.stsci.edu

5.1.2 VLBA 330 MHz

On 12 January 2011, we observed IRAS 10214 with the *VLBA* at 330 MHz with 32 MHz bandwidth per polarisation, split into four sub-bands. Nine of the ten *VLBA* antennas were used (Mauna Kea excluded). *VLBA* observations at *P*-band are challenging due to the comparatively poor receiver sensitivity as well as differential ionospheric phase delays that have a $\Delta t \propto \lambda$ dependence where Δt is the differential time delay measured between two elements in an array. The *VLBA* has never performed a successful phase referenced observation at 330 MHz because of these challenges[3]. As a result, phase calibration has to be performed 'in-beam'. This requires a bright ($\gtrsim$ 100 mJy), compact ($<$ 30 mas) source within the 1 deg^2 field-of-view. A powerful new software correlator (Deller et al., 2011), allows the correlation of multiple phase-centres within the field for a fractional increase in computational cost. To achieve this the data are correlated with 7.8 kHz spectral and 20 ms time resolution.

We used the results of our *EVN* phase calibrator search (see §5.1.1) as well as our *GMRT* observations (with similar FoV) to select candidate in-beam sources suitable for use as a phase calibrator. Through this selection technique, we identify 15 potential calibrators, as well as two sources of interest based on previous *MERLIN* observations. We performed a correlator pass on each of the 17 sources and IRAS 10214.

Each of the resultant 18 *uv*-datasets were averaged into 250 kHz channels resulting in 32 channels in each of the four sub-bands. The data were also time-averaged with an integration time of 1.6 s. We do not detect fringes on any of these phase-centre shifted sources. The primary reason is perhaps the large distances ($>$ 30 arcmin) of most candidate phase calibrators from the pointing centre. Also, none of these candidates were strong enough sources, with detectable fringes requiring flux densities in excess of 100 mJy (Adam Deller, priv. comm.). Therefore, the observations could not be phase calibrated and no low frequency detection of IRAS 10214 could be made at VLBI resolution. Further imaging of this system with the *Low-Frequency Array (LOFAR)* may yield such a detection in the future.

5.2 Results

In Fig. 5.1 we show the *EVN* 1.66 GHz CLEANED map with a 9-σ detection. The peak flux density of the imaged data is $S_{\rm peak} = 209 \pm 23$ μJy. Fitting a Gaussian to the CLEANED map returns an integrated flux

---

[3] http://www.vlba.nrao.edu/astro/guides/novice/sched.shtml

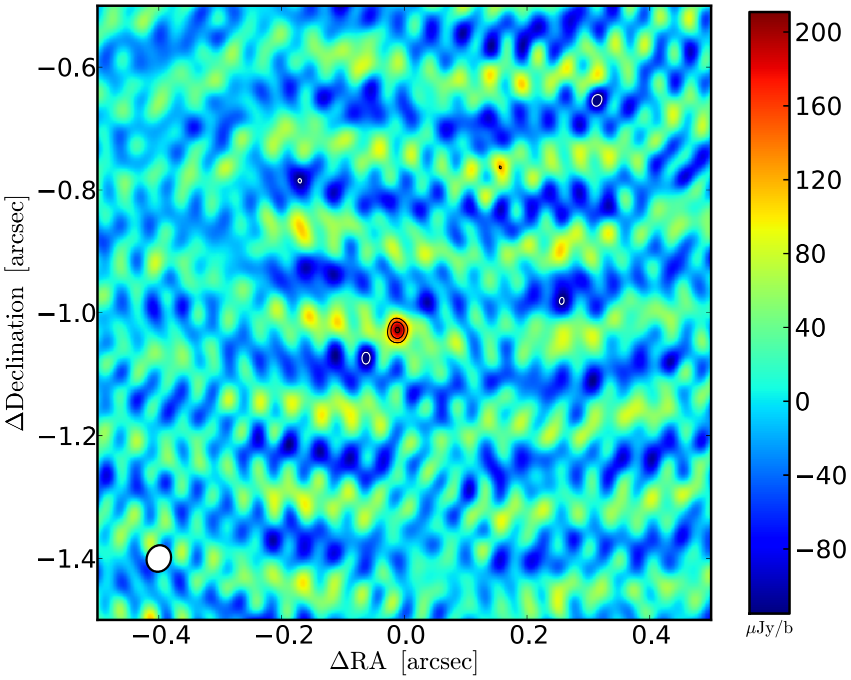

Figure 5.1: EVN 1.66 GHz continuum map of IRAS 10214. Over-plotted are contours starting from -4, 4-σ and increasing in steps of 2-σ, where σ = 23 μJy per 44 × 39 mas^2 beam (white ellipse at bottom left, position angle = - 25.1° east of north). The white contours indicate negative contours and black contours are positive. The peak and integrated flux densities are $S_{\rm peak} = 209 \pm 23$ μJy and $S_{\rm int} = 220 \pm 37$ μJy. The *uv*-data are limited to a maximum of 5 Mλ based on the quality of the phase solutions derived from the phase calibrator. The observed noise structure results from the *EVN* synthesised beam. The map co-ordinates are centred on the lensing galaxy *HST* F160W centroid (RA = 10$^{\rm h}$ 24$^{\rm m}$ 34.5622$^{\rm s}$, Dec = 47° 09' 10.809"

density $S_{\rm int}$ = 220 ± 37 μJy, which suggests that the source is unresolved. The measured flux density and position of the detection was checked for a large number of subsets of the data, including splits in frequency, time, and antenna selection. All these tests yield consistent positions and a flux density peak that ranges from $S_{\rm peak} \sim 190 - 220\,\mu$Jy. The positional uncertainty is $\sigma_\theta = 2.2$ mas, which is defined by $\sigma_\theta = 0.5\,{\rm FWHM}/({\rm S/N})$ (Condon, 1997).

As shown in Fig. 5.2, the *EVN* detection does not appear exactly co-incident with the *HST* F814W (rest-frame ultraviolet) peaks or the CO (1→0) total intensity map peak. First inspection shows that it lies roughly halfway along the main *HST* F814W arc (in RA), and > 100 mas northward of the centre of curvature. It is located ~170 mas towards the north-west of the main (eastern) *HST* F814W peak. As discussed in Chapter 3, the *HST* astrometry is in agreement with determinations from Nguyen et al. (1999); Eisenhardt et al. (1996); Evans et al. (1999) and Simpson et al. (2012, in prep.) to within $\Delta\theta < 10$ mas.

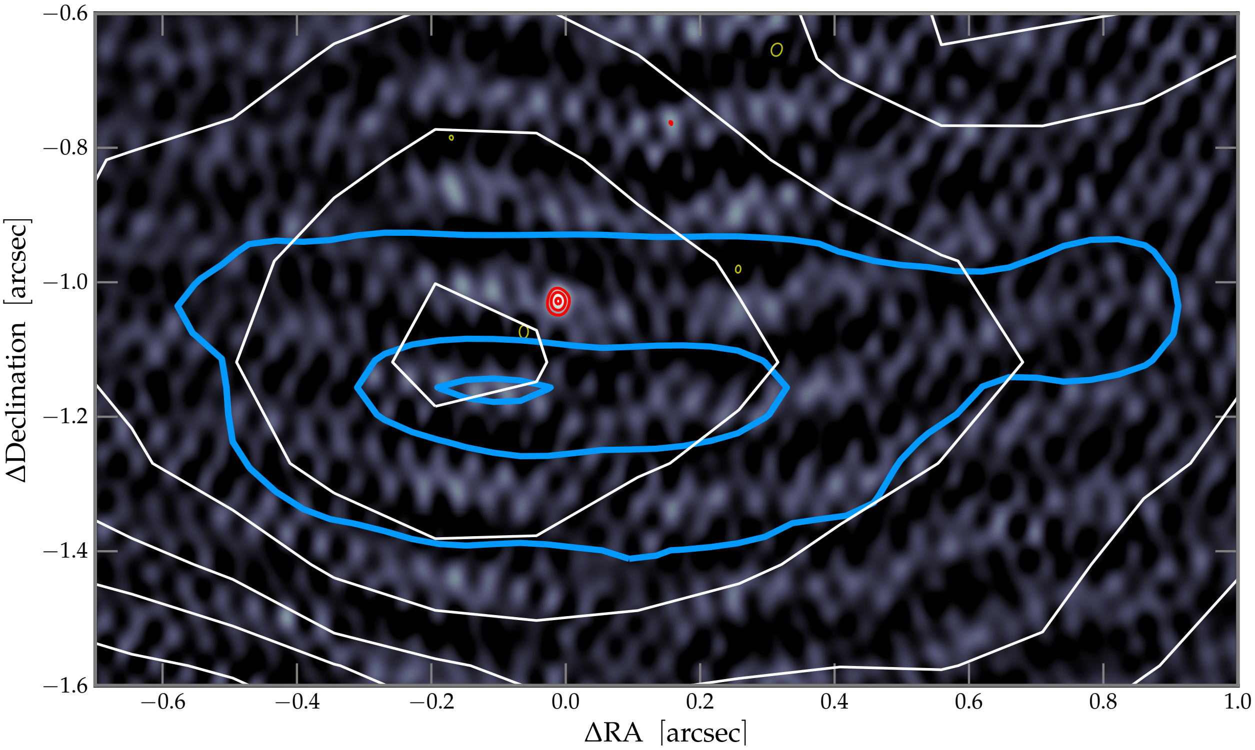

Figure 5.2: Zoomed-in view of the *EVN* 1.66 GHz continuum map from Fig. 5.1 with red *positive* contour levels at 4, 6, 8-σ and yellow *negative* contours at -4-σ. The CO (1→0) total intensity map is over-plotted in white contours with 2-σ intervals that start at -3, 3-σ ($\sigma_{\rm CO} = 60\,\mu$Jy beam^{-1}). The blue contours show the *HST* F814W (rest-frame UV) arc at 2, 50, 95% of the peak flux density. The CO (1→0) and *HST* F814W point spread functions are ~ 0.7 and 0.1 arcsec respectively.

The lensing configuration detailed in Chapter 2 and briefly reviewed in §1, includes a counter-image towards the north of the lens galaxy. Our *EVN* observations here do not detect any emission in the region of the *HST* F814W and *HST* F160W counter-images. We place a weak, 5-σ limit on the counter-image flux density of $S_{1.7,\rm min} \lesssim 100\,\mu$Jy since VLBI detections are generally only considered robust if greater than 5-σ, due to poor uv-coverage[4]. We place the same detection limit for any potential emission that is co-located with the secondary CO (1→0) peak (labelled 'A'), and for the lensing galaxies identified in Fig. 4.1. Note that these limits were obtained by shifting the phase centre to the *HST* F160W centroid in each case.

As stated in the introduction, one of the questions raised in the past is whether or not the *HST* F814W structure along the arc is intrinsic or if there are multiple images that are convolved together by the *HST* PSF. The *HST* arc would be split into three images, if the true (source-plane) source position were to move

---

[4] Since our *uv*-coverage is comparatively good for a VLBI observation, 5-σ is a relatively conservative upper limit.

northward. The relative magnification of these three split images would be defined by the cusp relation (e.g. Blandford et al., 1989; Keeton et al., 2003), which states that the flux density of the two outer images should have a sum equal to the flux density of the central image. Therefore, if two outer images were present, they should *each* have a flux density of $S_{\rm outer} \sim 105\,\mu$Jy, equivalent to a 4.5-$\sigma$ detection in the *EVN* map. No evidence of additional images is present within the extent of the *HST* optical/NIR arc. The cusp relation does assume a smooth dark matter profile, however substructure does not appear to impact image magnification ratios substantially (e.g. McKean et al., 2007; More et al., 2009).

Therefore, we assume the *EVN* image-plane is comprised of a main image (detected here at 9-σ) and an undetected counter-image that is in the vicinity of the *HST* detected counter-images.

5.3 Ultraviolet Polarisation Properties

Polarisation is a potential consistency check of a lens model, since theoretical arguments show that the polarisation angle undergoes a negligible change in galaxy-scale lensing (i.e. in the weak field limit, Dyer & Shaver, 1992). Since scattered light has a polarisation angle perpendicular to the vector between the source of the photons and the scattering clouds, we would therefore expect the vector between the AGN and scattering clouds to have a vector with position angle $\phi_{\rm pol} - 90^\circ$, where $\phi_{\rm pol}$ is the ultraviolet/optical polarisation angle.

In this section we collate previous rest-frame ultraviolet polarimetry measurements and review the spatially-resolved *HST* spectro-polarimetry reported in Nguyen et al. (1999), before comparing the polarisation with the derived source-plane properties of the *EVN* detection in §5.4. We wish to focus on three properties in particular: (1) the flux-weighted mean polarisation angle (includes spatially-unresolved UV polarisation angle determinations); (2) the median polarisation angle from spatially-resolved spectro-polarimetry; and (3) the maximum change in polarisation angle (i.e. the range).

5.3.1 Flux-weighted mean polarisation angle

A number of polarisation observations have been performed towards IRAS 10214 (e.g. Lawrence et al., 1993; Goodrich et al., 1996; Nguyen et al., 1999), all of which report high polarisation in the observed optical frame. A review of these results is summarised in Table 5.1 which shows that the shorter wavelengths

Telescope	**Bandpass** nm	**Polarisation %** percent	**Position Angle** degrees	**Reference**
Keck	412-420	26.5 ± 1.7	69.9 ± 0.2	Goodrich et al. (1996)
Keck	750-800	15.9 ± 0.4	69.9 ± 0.2	Goodrich et al. (1996)
WHT	400-1000	16.4 ± 1.8	75 ± 3	Lawrence et al. (1993)
HST	F437M	28 ± 3	62 ± 2.7	Nguyen et al. (1999)

Table 5.1: Flux-weighted mean polarisation properties of IRAS 10214 from the literature.

have higher polarisation percentages. In addition, there appears to be a discrepancy between the ground-based and *HST* polarisation position angles which Nguyen et al. (1999) suggest results from the ground based observatories' superior sensitivity to low surface brightness emission. For the remainder of the thesis, we refer to the flux-weighted mean polarisation angle ($\bar{\phi}_{\rm pol} = 68.9 \pm 1.3$), which is the weighted mean of the three independent polarisation angles listed in Table 5.1.

5.3.2 Median polarisation angle

In their spatially-resolved *HST* spectro-polarimetry of IRAS 10214, Nguyen et al. (1999) find the UV polarisation position angle varies smoothly between $\sim 65^\circ - 100^\circ$ east of north. We define the median of the measured polarisation angle range $\langle \phi_{\rm pol} \rangle = 82.5^\circ \pm 5^\circ$, where the uncertainty is that quoted in Nguyen et al. (1999). Note that this differs significantly from the flux-weighted mean, suggesting there is a polarised region smaller than the ~1 arcsec arc that dominates the polarised emission.

5.3.3 Polarisation Angle Range

The range of polarisation angles reported in Nguyen et al. (1999) is $\Delta\theta_{\rm max} \sim 35^\circ \pm 5^\circ$. A simplified argument is made in Nguyen et al. (1999) that assuming the source of the photons is a point source, and the diameter of the scattering region (D) is known, then the projected distance between the scattering clouds and the photon source can be approximated by the formula $R \approx D/\theta_{\rm max}$. They assumed magnifications of $\mu_{\rm UV}$ = 45 to 250 to derive an intrinsic UV source diameter of D = 40 to 100 pc (presumably by dividing the apparent source solid angle by $\mu_{\rm UV}$). This results in an AGN projected distance estimate of R = 160 to 65 pc. These magnification estimates were based on the constrained range of arc-to-counter-image flux ratios (and magnification by proxy). We update these estimates with the MCMC-derived *HST* F814W source-plane diameter of $D = 2\,r_s = 720 \pm 180$ pc, and find a projected distance to the AGN of $R = 505 \pm 148$ pc. This is likely to be an overestimate, as is discussed later, since the polarised emission is likely to be biased towards

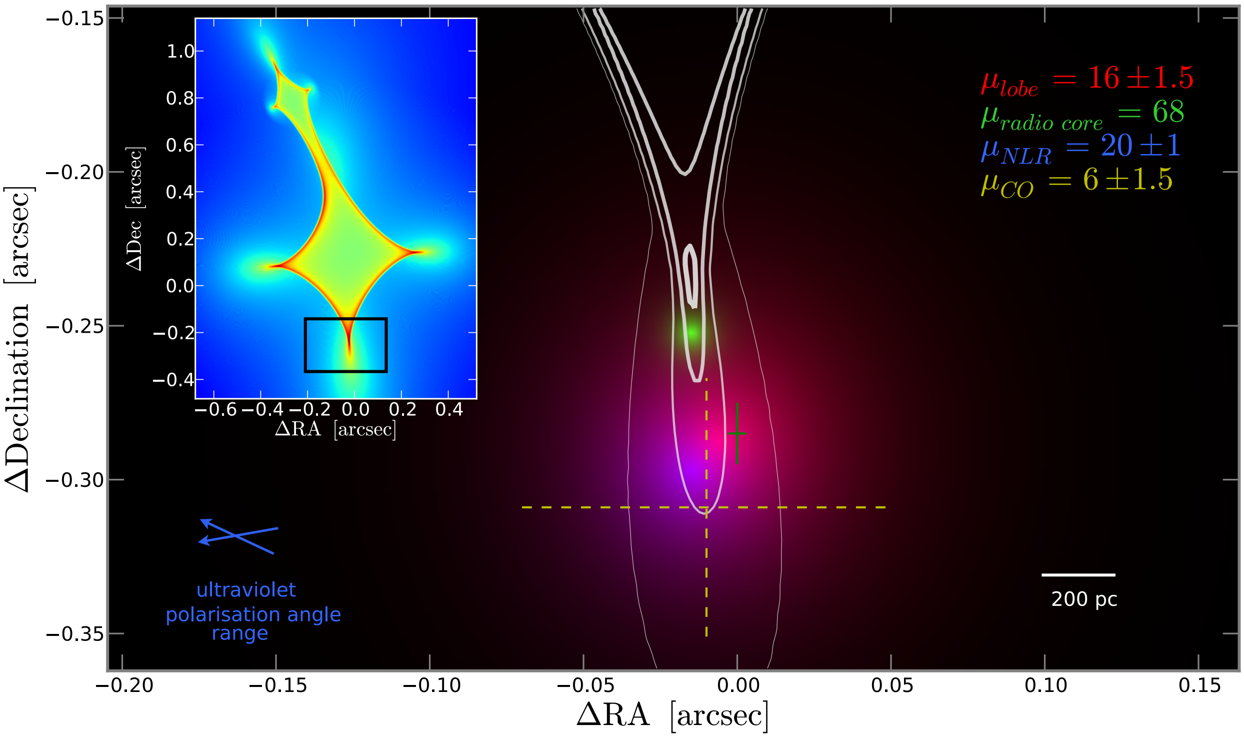

Figure 5.3: Source plane reconstruction of IRAS 10214 showing the radio core (green, *EVN* 1.7 GHz), scattered quasar light (blue, *HST* F814W) and radio lobe (red, *MERLIN* 1.7 GHz). The yellow, dashed cross shows the CO (1→0) total intensity map source-plane centroid and its uncertainty (the extent of the source-plane CO (1→0) component is beyond this entire frame). The green cross indicates the 8 GHz map source-plane centroid and its uncertainty. The white contours represent lines of equal magnification extending from the caustic at levels μ = 10, 20, 50, 100. The blue arrows (bottom left) depict the range of UV polarisation angles along the *HST* F437M arc. The inset shows the full lens caustic with colour-scale representing magnification and the black rectangle showing the borders of the enlarged region.

the brightest, and therefore more compact emission.

The polarisation angle range also provides another key piece of information. In principle, it enables a robust estimate of the ionisation cone opening angle (and hence the covering factor), assuming the incident photons originate from a point source. We use this observational constraint in our bolometric luminosity estimates in §5.5.4.

5.4 Source Plane Properties

We calculate the source plane position of the *EVN* detection using the GLAMROC[5] software. We use Lens Model A, as defined in Chapter 2. This assumes a Singular Isothermal Ellipsoid (SIE) potential for the main lens at $z = 0.893$, and a Singular Isothermal Sphere (SIS) potential for the secondary, line-of-sight galaxy at $z = 0.782$. IRAS 10214 is assumed to be a point source, which is consistent with the Gaussian fit presented in §5.2. The *EVN* source-plane co-ordinates are therefore the two remaining free parameters to solve for. We perform ray-tracing of a point source from the source plane to the image plane, and minimise the predicted image-plane position with respect to the measured *EVN* position. The resultant magnification of the best-fit point-source model is $\mu_{\rm EVN} = 68$. The magnification random error due to the ~ 2 mas *EVN* positional uncertainty is of order 5%, and therefore the systematic uncertainty of $\sim 40\%$ discussed in (Sec. 2.1.7) dominates the absolute magnification uncertainty.

Given the low probability that a small (< 50 mas) source is located within < 20 mas from the cusp of our lens model, we describe a few consistency checks on the *EVN* source-plane position, and its high magnification.

Firstly, the *EVN* source is north-ward of the *HST* arcs and as stated in §**??** does not split into 3 images (at 4.5-σ significance) and therefore is most likely to the south of (or on) the cusp of the caustic. Secondly, it is positioned roughly along the vector that extends from the centre of the lens and bisects the angle subtended by the rest-frame UV/optical arcs. This implies that the source-plane position must be very close ($<$ few milli-arcseconds) to the cusp of the caustic, since this is the region with large tangential deflection angles. The *EVN* point source is therefore essentially ‘wedged’ between the inner-caustic and the *HST* arc, which will always result in high magnifications regardless of changes in the macroscopic lens model.

Assuming the *EVN* point source is the obscured active nucleus, then its source-plane position is consistent with a number of multi-wavelength observations, which are outlined below.

1. The IRAS 10214 *HST* F437M arc centre-of-curvature is shifted northward (12±14 mas) when compared to that of the *HST* F814W arc (see Fig.1, Nguyen et al. 1999). Although the astrometric precision of this measurement is challenging (see Nguyen et al. 1999 for a discussion), the resultant interpretation is consistent with a northern AGN core and the fact that shorter wavelengths are

---

[5] Gravitational Lens Adaptive Mesh Raytracing of Catastrophes, see http://kipac.stanford.edu/collab/research/lensing/glamroc

scattered more efficiently. Therefore, the F437M filter could be dominated by scattered quasar light which is scattered closer to the source of these UV photons. The VLBI-detected core has a consistent northern offset ($\gtrsim$100 mas) from the *HST* F814W centre of curvature.

2. Simpson et al. (2012, in prep.) present two narrow band maps centred on the redshifted C IV and [O III] lines, which are typical broad-line and narrow-line region emission lines respectively. They determine the centers of curvature of both and find that the C IV arc is roughly 50 ± 20 mas northward of the [O III] centre of curvature for the highest S/N bins.

3. There are a number of qualitative and quantitative consistencies between the source-plane ultraviolet and radio core positions. The flux-weighted mean ($\bar{\phi}_{\rm pol} = 68.9 \pm 1.3$) and median ($\langle \phi_{\rm pol} \rangle = 82.5^\circ \pm 5^\circ$) ultraviolet polarisation angles are roughly perpendicular to the position angle between the vector connecting the *EVN* radio core and *HST* F814W source-plane centroids ($\phi_{\rm core,uv} \sim 0^\circ$). Moreover, the flux-weighted position angle has a lower value than the median, consistent with the fact that the brightest UV peak in the image plane is eastwards on the *HST* F814W arc. The expected intrinsic UV source size for a maximum polarisation angle change of $\Delta\theta = 35^\circ \pm 5^\circ$ is $r = 110\pm^{10}_{18}$ pc. This assumes the source plane distance between the *EVN* and *HST* F814W components of 370 pc, as derived in our independent source plane reconstruction. This is broadly consistent with our MCMC-derived, *HST* F814W source-plane radius ($r_{\rm s,814} = 360 \pm 90$ pc) of the *unpolarised* emission, given that the polarisation measurements will be biased towards the brighter, and therefore, more compact emission.

   Our result is consistent the Nguyen et al. (1999) prediction of where the active nucleus ought to be, based on the smooth polarisation variation and the more northern *HST* F437M centre of curvature. This is promising example of the potential held by high sensitivity, high resolution spectro-polarimetry with next-generation 30-40 metre optical/IR telescopes and the *JWST* in precisely locating the active nuclei in high-redshift galaxies.

In Fig. 5.3 we plot the best-fit source plane position of the *EVN* 1.7 GHz component, along with the *HST* F814W source plane position derived in Chapter 3. In Chapter 4 we argue that the IRAS 10214 CO (1→0) flux density is split roughly equally between a compact, unresolved component and a more spatially extended low excitation gas reservoir, based on the peak of the CO spectral line energy distribution, spatially-resolved CO $(1\rightarrow0)$ observations, and Large Veloicty Gradient (LVG) modelling.

We argued that the unresolved CO $(1\rightarrow0)$ 'core' component is likely to be co-spatial with the higher-J CO rotation lines which are heated by the active nucleus. Figure 5.3 shows that the AGN core is in close proximity to the unresolved CO $(1\rightarrow0)$ 'core' centroid, which is consistent with the hypothesis that the *EVN* detection is indeed a radio detection of the active nucleus. Spatially resolved observations of the high-J CO lines are required to investigate this in further detail.

The source-plane model we propose here is clearly asymmetric, as is seen in the nearby Universe with narrow-band imaging of NLR regions (e.g. Simpson et al., 1997), and inferred from correlated asymmetry as seen in radio and Seyfert galaxies (e.g. Liu & Pooley, 1991).

5.5 Discussion

5.5.1 AGN Core or Highly-Magnified Star-Formation Clump?

At first glance, the *EVN* detection is likely to be the AGN radio core, however, careful consideration is required given the close proximity of the cusp of the caustic. IRAS 10214 was discovered at $\lambda_{\rm obs} = 100\,\mu$m, a wavelength biased towards warm, partially AGN-heated ($T \sim 100$ K) dust. This is broadly consistent with its AGN features across the spectrum and so the close proximity of an AGN core to the cusp would be expected. However, the probability that such a compact point source is within a few milli-arcseconds of the cusp is low. We must consider an alternative scenario where the *EVN* detection is co-spatial with a star-forming complex with an exceptionally large magnification ($\mu > 100$). This potentially has a higher probability given the supernovae rate we expect from the prodigious star formation in IRAS 10214 ($SFR > 100\,{\rm M}_\odot\,{\rm yr}^{-1}$) and therefore the number of star-formation clumps.

We calculate the brightness temperature of the *EVN* -detected emission using Equ. 6 in Chapter 3. We assume a solid angle equal to the area of the beam effective radius (i.e. $\Omega_{\rm beam} = \pi\,\frac{1}{2}\theta_{\rm maj}\,\frac{1}{2}\theta_{\rm min}$ where $\theta_{\rm maj,min}$ are the FWHM values of the beam). The peak flux density is $S(\nu_{\rm o}) = 209\,\mu$Jy, which results in a rest-frame 5.45 GHz brightness temperature lower limit of $T_{\rm B} > 5\times10^5$ K, since the source is unresolved. Since deconvolution of this map indicates that it is unresolved, our brightness temperature lower limit is a conservative one.

The brightness temperature lower limit of $T_{\mathrm{B}} > 5 \times 10^5$ K is high, but does not completely rule out a star formation origin which appears to saturate at $T_{\mathrm{SF}}^{\mathrm{max}} \sim 10^5$ K (Muxlow et al., 1994). Note that this lower limit does not depend on magnification as the surface brightness, and hence, the brightness temperature is not affected by gravitational lensing. More distinguishing is the implied SFR density (Σ_{SFR}) if we assume that the *EVN* detected flux density is associated with star formation. Using Equ. 7 in Chapter 3, we calculate the implied SFR assuming all the emission is due to star formation. Following Condon et al. (2002) who assume a Salpeter IMF; and setting the intrinsic source size equal to the *EVN* 1.7 GHz beam, we calculate a lower limit of $\Sigma_{\mathrm{SFR}} > 8.4 \times 10^4\,\mathrm{M}_{\odot}\,\mathrm{yr}^{-1}\,\mathrm{kpc}^{-2}$, . This is significantly larger than the theoretically motivated and observationally supported value of $\Sigma_{\mathrm{SFR}}^{\mathrm{max}} \sim 1000\,\mathrm{M}_{\odot}\,\mathrm{yr}^{-1}\,\mathrm{kpc}^{-2}$ (see Elmegreen, 1999; Thompson et al., 2005; Scoville et al., 1997; Downes & Solomon, 1998).

Finally, we compute the expected the far-infrared luminosity of the *EVN* detection assuming it is a star forming clump (again, following Condon et al. 2002), and compare this with the far-infrared luminosity measured from the infrared SED. The former results in an far-infrared luminosity $L_{\mathrm{FIR,EVN}} = 6.8 \times 10^{12}\,L_{\odot}\,\mu^{-1}$, which is an order of magnitude lower than the FIR SED derived value of $L_{\mathrm{FIR}} = 7.1 \times 10^{13}\,L_{\odot}\,\mu^{-1}$ (Verma et al. 2012, in prep.).

These arguments, in additional to those presented in §5.4, appear to support that this is an AGN core, which is what we assume for the remainder of the chapter. As argued in §5.4, this is consistent with a number of multi-wavelength and polarisation properties.

5.5.2 Nature of *VLA* 8 GHz Map Peak

In Chapter 3, we suggested that the *VLA* 8 GHz map could potentially be dominated by a radio core, based on the radio spectral index behavior from 330 MHz through 16 GHz. However, the 8 GHz centroid is significantly offset ($\Delta\theta \sim 300$ mas) from the *EVN* detection presented here (see Fig. 5.5). The nature of the 8 GHz emission is puzzling, since we would expect it to be co-located with the *EVN* detection, especially since their flux densities are very similar ($S_{8\mathrm{GHz}} = 280\,\mu$Jy), assuming a flat radio spectrum. It does not seem that this discrepancy can be discarded on the basis of insufficient astrometric accuracy. This is because the 8 GHz centroid was measured for two independent observations performed in 1991 and 1995, both with the *VLA* in A-configuration and hence a resolution of $\theta_{\mathrm{syn}} \sim 0.23$ arcsec. As discussed in

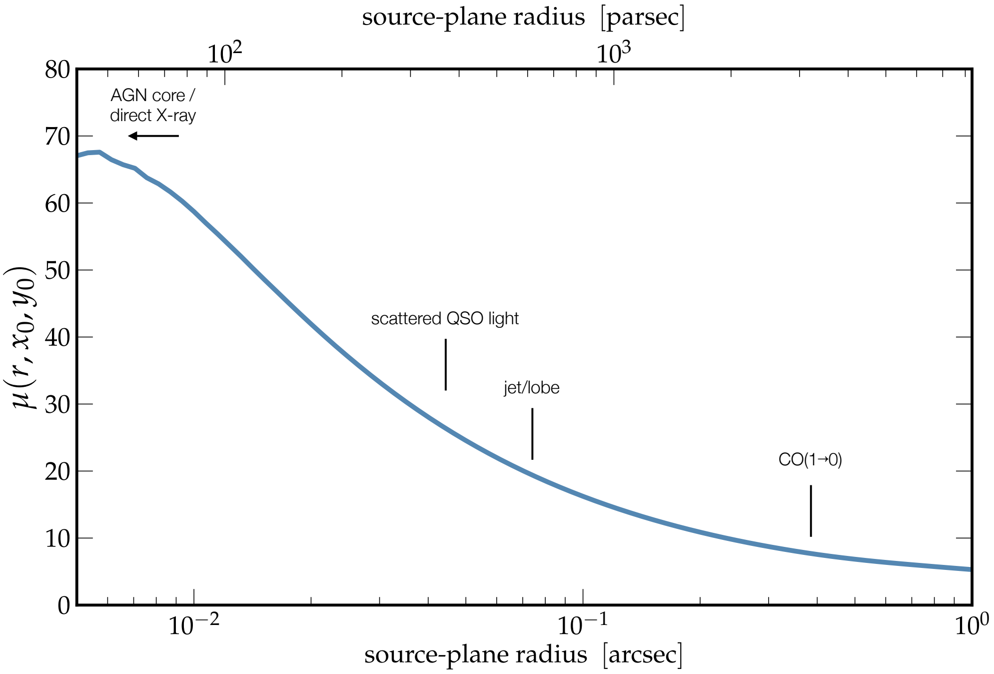

Figure 5.4: Total magnification as a function of source-plane scale radius, *assuming the EVN source-plane centroid.* The annotations serve as a rough guide of the physical sizes. The centroids of the listed components are not the same as the *EVN* component and therefore the resultant magnifications are marginally different. The point source magnification at the best-fit *EVN* position is $\mu_{\rm pt} = 68$.

§5.1.1, the astrometry of the *EVN* map appears secure to within $\lesssim 2$ mas. The true nature and extent of the 8 GHz emission will be further probed by a *C*-band *JVLA* polarisation observation of IRAS 10214 in A-configuration (~ 30 mas angular resolution) with 2 GHz bandwidth. With the *EVN* map we can estimate a 5-σ limit on the spectral index of the 8 GHz peak of $\alpha < -0.54$, assuming it is a point source and defining $\alpha \equiv -\log(S_1/S_2)/\log(\nu_1/\nu_2)$.

5.5.3 Resolved Out Radio Emission

The radio core flux is ~20% of the total flux in the 1.7 GHz *MERLIN* map presented in Chapter 3. If we assume the remaining flux is associated with star formation, the implied star formation rate is $SFR \sim 3.2 \times 10^4 \mu^{-1} \mathrm{M}_\odot\,\mathrm{yr}^{-1}$ following Equ. 7 in Chapter 3. If the *MERLIN* 1.7 GHz magnification ($\mu_{1.7} = 16 \pm 1.5$) derived in Chapter 3 is assumed to be equivalent to the star formation magnification, then this results in an intrinsic star formation rate of $SFR \sim 2 \times 10^3 \mathrm{M}_\odot\,\mathrm{yr}^{-1}$. This is an exceptional star formation rate, which suggests that there may be significant flux in radio jet/lobe components that are resolved out by the *EVN*

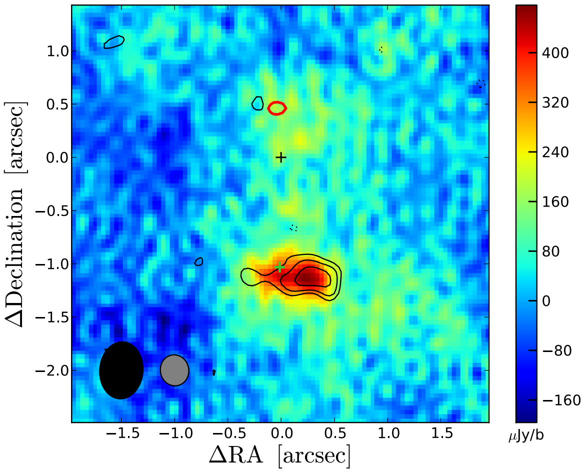

Figure 5.5: *MERLIN* 1.7 GHz map shown in colour-scale with $\sigma \sim 46$ μJy per 405 × 349 mas^2 beam (position angle = -4.35°). Over-plotted in black contours is the 8 GHz *VLA* map with $\sigma \sim 11$ μJy per 292 × 267 mas^2 beam (position angle = -79.64°). Contours are at $\pm 3\sigma$ and increase by a factor of $\sqrt{2}$. Dashed lines represent the negative contours. The green cross indicates the location of the *EVN* detected radio core, where the cross length is a factor $\gtrsim 10$ larger than the *EVN* positional uncertainty.

observations. It is unlikely that the total magnification boost of the star formation emission region is higher, since any disk with a reasonable star formation size ($\gtrsim 1$ kpc) undergoes a magnification boost of $\mu \lesssim 10$.

5.5.4 Quasar Bolometric Luminosity

Having detected the radio core and made an estimate of its magnification, we now wish to use these results to estimate the quasar bolometric luminosity in IRAS 10214. The bolometric luminosity of high redshift, obscured quasars like IRAS 10214 must be estimated with care. Significant uncertainty stems from the intrinsic dust obscuration, electron and photon scattering; as well as the magnification for a lensed source. We derive the *quasar*[6] bolometric luminosity using five methods in the X-ray, ultraviolet and mid-infrared. Where applicable, we estimate intrinsic specific luminosities and compare these to an Elvis et al. (1994) average quasar spectrum to determine the corresponding bolometric luminosity. We believe the five selected methods to be least sensitive to the factors described above (amongst the techniques we have at our disposal).

---

[6] This ignores the star formation contributions which appear to dominate the combined starburst/quasar bolometric luminosity as demonstrated in previous work.

[O III] Equivalent Width $L_{\rm bol}$ Estimate

The first method uses the equivalent width (EW) of the forbidden [O III]λ5007 line to measure the 'missing' optical continuum flux as a result of the obscuring geometry (Miller et al., 1992). Their method measures the average [O III] equivalent width of 76 type-I quasars from the Bright Quasar Survey (BQS), which provides a method to estimate the obscured AGN continuum flux, and hence the extinction. The idea is that the narrow-line-region flux will be largely unaffected by the orientation of the quasar since it is above and beyond the putative torus, whereas the central AGN continuum would be obscured under the unified quasar model (Antonucci, 1993). Since the equivalent width measures the fraction of energy of a spectral line relative to the underlying continuum, the greater the central AGN obscuration, the more exaggerated the equivalent width of a narrow line like [O III] will be from its intrinsic value.

Miller et al. (1992) measure an average rest-frame [O III] equivalent width $\langle EW \rangle_{\rm OIII}$ = $24\pm^{25}_{12}$ Åfor their BQS survey sample. Serjeant et al. (1998) measure the [O III] rest-frame EW of IRAS 10214 to be $EW_{\rm OIII}$ = 580 $(1+z)^{-1}$ = 176 Å. Two approaches can now be followed to estimate the bolometric luminosity. The first simply assumes that given a measurement of the [O III] line flux density, one can estimate the bolometric luminosity with the relation

$$L_{\rm bol} \; = \; L_{\rm OIII}\, \mu_{\rm NLR}^{-1}\, BC, \tag{5.1}$$

where $L_{\rm OIII} = 2.05 \times 10^{37}$ W (Serjeant et al., 1998; Lacy et al., 1998) and BC is a bolometric correction factor calculated from the average quasar [O III] equivalent width (Miller et al., 1992) and a correction factor to convert the specific luminosity at 5100 Åto a bolometric luminosity (Elvis et al., 1994). This results in a bolometric luminosity estimate of $L_{\rm bol} = 2.4 \pm 0.6 \times 10^{11}$ $L_{\odot}$.

The second $L_{\rm bol,OIII}$ estimate is less direct. It extrapolates an optical continuum flux based on a dust-reddened quasar SED fit to the ultraviolet photometry. Scattered QSO light is presumed to dominate the latter. By comparison of the observed IRAS 10214 and average quasar [O III] equivalent widths, the argument can be made that only $13.6 \pm^{14}_{6.8}$ % of the AGN core continuum emission is observed at 5100 Å. Therefore, we can estimate the true specific luminosity at 5100 Åas follows:

$$\begin{aligned} L_{5100,\mathrm{true}} &= L'_{5100,\mathrm{obs}} \frac{EW'_{\mathrm{OIII}}}{\langle EW \rangle_{\mathrm{OIII}}} \\ &= L_{5100,\mathrm{obs}}\, \mu_{5100}^{-1} \frac{EW_{\mathrm{OIII}}}{\langle EW \rangle_{\mathrm{OIII}}} \frac{\mu_{5100}}{\mu_{NLR}}, \end{aligned} \tag{5.2}$$

where EW_{OIII} is the measured [O III] equivalent width; $\langle EW \rangle_{\mathrm{OIII}}$ is the average [O III] equivalent width (Miller et al., 1992); $L'_{5100,\mathrm{obs}}$ is inferred from the lensed, host-galaxy-reddened *quasar* flux density at 5100 Å, $S_{5100,\mathrm{obs}}$ = 1.52 $\times 10^{-5}\,\mu_{5100}^{-1}$ Jy; and μ_{5100}/μ_{NLR} accounts for the difference in magnification between the narrow-line region and the AGN nucleus. Note that $\mu_{5100} = \mu_{\mathrm{AGN}}$ since we are interested in the specific luminosity of the quasar at 5100 Å.

To calculate $L'_{5100,\mathrm{obs}}$, we fit the average quasar spectrum (Elvis et al., 1994) to the 11 UV photometric points between rest-frame 1000 – 2750 Åand interpolate to 5100 Åsince this wavelength is dominated by stellar emission as discussed earlier. This includes the *HST* F814W photometric point and is therefore assumed to be scattered quasar emission given the high degree of polarisation. The UV photometric points are reddened by a range of dust models from Pei (1992) to account for *host galaxy* extinction, since this is scattered QSO light. The fit results in a best-fit visual extinction A_v = 0.18 (SMC dust grain model), with a χ^2_v = 1.3. The extinction is comparable to the $A_V \sim 0.3$ from Lacy et al. (1998) toward the NLR based on the He II 468.6 / 164.0 ratio of 4.3). The best fit extinction, bolometric luminosity, and χ^2_v have very little variance with subsets of the UV photometric points (from 4 to 11), however the goodness-of-fit begins to decrease substantially once the optical photometry is included, as one would expect with a significant stellar component. The full resolution UV spectrum from which these photometry points originate from, has a continuum baseline that Rowan-Robinson et al. (1993) fit with two linear models which meet at $\lambda_{\mathrm{rest}} \sim 2600$ Å. This supports our selection of fitting boundaries, as well as the goodness of fit behaviour as this boundary is extended into optical wavelengths. The reddened quasar fit to the observed ultraviolet spectrum is plotted in Fig. 5.8.

This implies a bolometric luminosity $L_{\mathrm{bol,OIII}} = 1.9\pm^{2.0}_{1.0} \times 10^{39}\,\mu_{5100}^{-1}\,\mu_{5100}/\mu_{\mathrm{NLR}}$ W. Assuming our previously derived magnification factors, this leads to a $L_{\mathrm{bol,OIII}}$ = 2.8 $\pm^{2.8}_{1.4} \times 10^{11}\,\mathrm{L}_{\odot}$, which is 16% greater than the first $L_{\mathrm{bol,OIII}}$ method. At face value, this is tentative evidence that our ultraviolet SED fit includes a small (<20%) stellar contribution. We adopt the average of the two and assign an uncertainty based on the $\langle EW \rangle_{\rm OIII}$ scatter, which dominates the uncertainties. The result is $L_{\rm bol,OIII} = 2.6 \pm^{2.6}_{1.3} \times 10^{11}\,{\rm L}_\odot$.

Ultraviolet $L_{\rm bol}$ Estimate

The scattered quasar light we observe is of course a fraction of the total quasar light. If we can determine covering factor and appropriate magnification, then we can determine the intrinsic quasar bolometric luminosity. The magnification is reasonably assumed to be $\mu = 20$ since the *HST* F814W observation directly probes the emission assumed to be dominated by the scattered quasar light. The covering factor (CF = 0.195) is approximated by the maximum change in polarisation angle ($\theta_{\rm max}$) of the scattered ultraviolet light as discussed in §5.3. The measured luminosity at 2400 Å(rest-frame *HST* F814W) is $\nu L_{2400} = 5 \times 10^{11}{\rm L}_\odot$. We also account for host galaxy extinction (A_V = 0.18) based on the modeling described in §5.5.4. This leads to a UV bolometric luminosity estimate of $L_{\rm bol,UV} = 2.7 \pm 1.1 \times 10^{11}\,{\rm L}_\odot\, f_{\rm scatt}^{-1}$. The scattering fraction $f_{\rm scatt}$ will increase the derived value if much smaller than unity. The resonant [O VI] 1032, 1036 Å doublet are in an optically thick (1:1) ratio (Serjeant et al., 1998) suggesting they are in thermal equilibrium, providing evidence for a large opacity ($\tau > 1$) in the NLR (i.e. $f_{\rm scatt} \sim 1$). However, the same authors find that this implies densities that are only found in the broad-line region. They argue that Ly-β resonant absorption could distort the intrinsic doublet line ratio, if the [O VI] doublet lies inside the saturated Ly-β damping wings. A lower opacity $\tau < 1$ is also supported by the double-peaked Ly-α emission (which are both red- and blue-shifted). In summary, this shows that we are fairly ignorant of the true $f_{\rm scatt}$ value, however would expect that it is not at the extrema of the allowed values.

A method to estimate the scattering fraction $f_{\rm scatt}$ is to compare the observed ultraviolet specific luminosity (assumed to be dominated by scattered QSO light) with the predicted value based on the independently derived bolometric luminosity from the reddened quasar fit in §5.5.4. Performing this at 1350 Åthe ratio is

$$\begin{aligned} f_{\rm scatt} &= L_{\rm 1350,obs}\; 2.5\log(A_{\rm UV})\; \mu_{\rm UV}^{-1} \;/\; \langle L_{1350} \rangle \\ &= 55\% \end{aligned}$$

where $A_{\rm UV}$ and $\langle L_{1350} \rangle$ are derived from a reddened Elvis quasar model as described in §5.5.4, assuming the

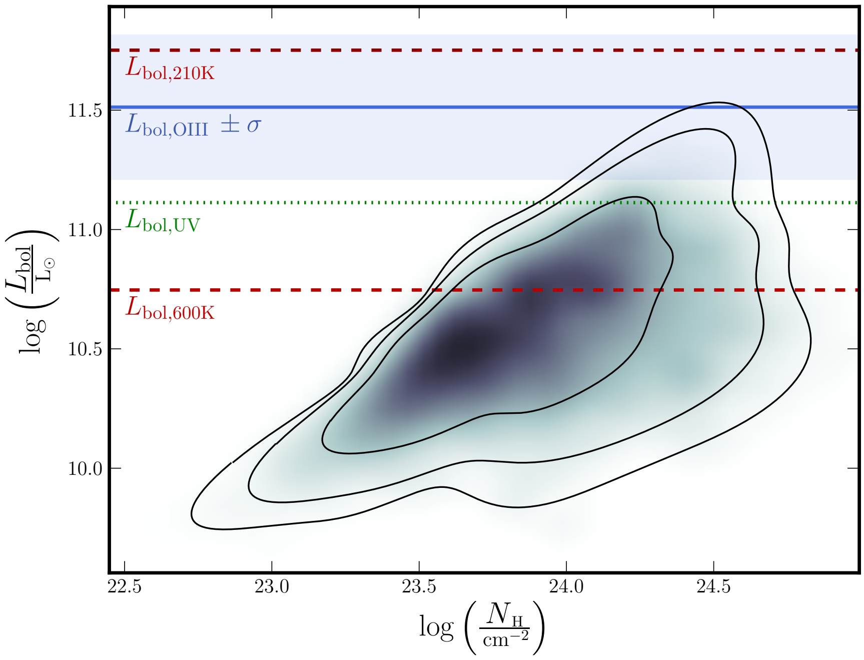

Figure 5.6: Two dimensional posterior PDF assuming the Wilman & Fabian (1999) X-ray model spectra. The contours correspond to 68%, 95% and 99% confidence levels. The blue line indicates the bolometric luminosity as derived from the [O III] equivalent width and the blue shaded horizontal band corresponds to the associated 1-σ uncertainty. The two dashed red lines indicate the two dust bolometric luminosity estimates, while the green dotted line is the ultraviolet $L_{\rm bol}$ estimate. Note that the Compton limit is $\sim 10^{24}$ cm^{-2}. For clarity, we have not included the $L_{\rm bol,UV}$,$L_{\rm bol,210K}$ and $L_{\rm bol,600K}$ uncertainties. They are dominated by the quadrature sum of the covering factor and magnification uncertainties and are of order 0.3-0.5 dex.

weighted mean quasar bolometric luminosity calculated at the end of this section.

The derived UV scattering fraction $f_{\rm scatt}$ is in the region we expect ($f_{\rm scatt} \lesssim 1$) based on the above arguments. We plot the $L_{\rm bol,UV}$ estimate in Fig. 5.6 (green line) assuming an $f_{\rm scatt}$ = 100% and note that a value of $f_{\rm scatt}$ = 55% would increase this estimate by a factor of 1.8.

Mid-Infrared $L_{\rm bol}$ Estimates

Spitzer mid-infrared spectroscopy has proved a powerful technique to probe the heart of quasar host galaxies through dust heating and spectral features. In the case of IRAS 10214, the mid-IR spectrum is best fit with three components: (1) a typical star-forming dust temperature of 50 K; (2) a warm 210 K component; (3) a hot 600 K component (see Teplitz et al., 2006; Efstathiou, 2006). We motivate appropriate covering factors and magnifications for the latter two components which we expect are predominately heated by the central

AGN. This will allow additional estimates of the intrinsic bolometric luminosity.

600 K Dust

Efstathiou (2006) fit a 600 K component to the mid-IR spectrum that has an apparent bolometric luminosity $L_{\rm bol,600K} = 7.4 \times 10^{11}\,{\rm L}_\odot\ CF^{-1}_{\rm 600K}\ \mu^{-1}_{\rm 600K}$. The covering factor ($CF_{\rm 600K}$) and magnification ($\mu^{-1}_{\rm 600K}$) at this temperature do not represent that of a distinct physical component, but rather a representative average of the hot dust component. We contend that this 'component' is associated within ~50 pc of the radio core and therefore has a mean magnification of $\mu_{\rm 600K} \sim 68$, as inferred from Fig. 5.4. The distance limit is based on MIR interferometric (using VLTI) size limits from nearby Seyfert galaxies (Tristram et al., 2009; Tristram & Schartmann, 2011). These authors find a size-luminosity relation $s = pL^{0.5}$, where $p = 1.8 \pm 0.3 \times 10^{-18}$ [pc W$^{-0.5}$]. This implies a torus size of order s = 40±6 pc for IRAS 10214. The covering factor for this component is set to the value derived in Mor et al. (2009), who model the mid-IR spectra of 26 luminous QSOs with 3 dust components: (1) a clumpy torus; (2) a dusty narrow line region; (3) a hot blackbody representing the hottest dust around the nucleus. A 600 K dust component would clearly be associated with the last of these three components, for which the authors find a mean covering factor $\langle CF \rangle$ = 0.23. This covering factor compares well with our adopted value CF = 0.195 which is based on the maximum change in polarisation angle. Based on this covering factor and magnification we estimate a bolometric luminosity $L_{\rm bol,600K} = 4.8 \pm^{5}_{2.2} \times 10^{10}\,{\rm L}_\odot$. The uncertainty on this estimate is dominated by the CF scatter which is estimated to be ~0.1 from Mor et al. (2009, see Fig. 11).

210 K Dust

This bolometric luminosity estimate follows the same reasoning as the 600 K component, however the average distance of clouds contributing to this temperature is greater than that of the hotter, 600 K dust and therefore likely to undergo a different amplification boost. The peak rest wavelength of this component is 14 μm, just longward of the 10 μm silicate feature. Based on mounting evidence from silicate *emission* in type II Seyferts (e.g. Sturm et al., 2006; Shi et al., 2006), as well as resolved silicate imaging on ~100 pc scales (Schweitzer et al., 2007), it appears that the ~10 μm emission may be dominated by a combination of outer torus and NLR dust cloud emission. Following the NLR modelling of Mor et al. (2009), we estimate a NLR distance of $r_{\rm NLR} = 125\pm^{35}_{25}$ pc.

Based on the greatly simplified scenario above, we estimate the bolometric luminosity of the 210 K component is dominated by NLR dust clouds with a radius of 125 pc. We therefore make the simplified argument that the 210 K component has a 125 pc radius; the same covering factor as derived before ($CF = 0.195$); and is centred on the *EVN* point source which results in a magnification $\mu_{210\rm K} \sim 50$ (from Figure 5.4). Efstathiou (2006) and Teplitz et al. (2006) find a 210 K component bolometric luminosity of roughly $L_{\rm bol,210K} = 5.5 \times 10^{12}\,{\rm L}_{\odot}\; CF^{-1}_{210\rm K}\; \mu^{-1}_{210\rm K}$. We therefore find $L_{\rm bol,210K} = 5.6 \pm 3 \times 10^{11}\,{\rm L}_{\odot}$ from the assumptions above. This is higher than the other bolometric estimates, especially that based on the 600 K dust. This could be expected since some, potentially large, fraction of the 210 K dust heating will arise from the prodigious star formation in IRAS 10214. An estimate of this contribution is the fraction of luminosity a 80 K greybody (i.e. dust primarily heated by star formation; and roughly where the IRAS 10214 mid-IR spectrum peaks) contributes at $\lambda = 14\ \mu$m, the wavelength that corresponds to the peak of a 210 K greybody. The former contributes 1.5% assuming equal amplitudes. Previous work has shown that the star formation dominates the bolometric luminosity of IRAS 10214 at the >90% level. If we assume a star formation to quasar $L_{\rm bol}$ ratio in the 90-95% range, then an 80 K greybody contributes ~15-30% to the flux at 14 μm (210 K peak wavelength). This suggests the $L_{\rm bol,210K}$ estimate is significantly contaminated by star formation.

X-ray $L_{\rm bol}$ Estimate

This method uses an X-ray spectrum fit employing the models of Wilman & Fabian (1999) to find the best fit column density of intervening hydrogen ($N_{\rm H}$). The X-ray models are Monte Carlo derived and assume an intrinsic unobscured type-I quasar X-ray spectrum of the form $L_{\nu} \propto \nu^{-0.9} e^{-\nu/\nu_{\rm c}}$ (where h$\nu_{\rm c}$ = 360 keV) as described in Madau et al. (1994). Wilman & Fabian (1999) generate a library of models with a range of hydrogen column densities ($N_{\rm H}$), assuming 5 × solar metallicity as they find this provides a superior fit to the hard X-ray background which peaks at ~30 keV. For simplicity, we do not use their models that include a reflection component off an accretion disk subtending 2π steradian and placed at a fixed inclination of 60°. The models further assume a 2% flux component that is scattered off the central ionized medium. In our MCMC routine we include a scatter on the scattered percentage with FWHM = 10% (with range 0 – 100

%). The resulting models are compared to the X-ray observations of IRAS 10214 with both Chandra and XMM-Newton Space Telescopes (which have consistent, albeit low S/N, results). Samples of the posterior PDF of the hydrogen column density $N_{\rm H}$ and bolometric luminosity $L_{\rm bol}$ are drawn in a MCMC algorithm similar to that described in Chapter 3. Fitting a library of X-ray models to the three X-ray data points is a weakly-constrained problem, and so an important caveat to these results is that we assume a hydrogen column density prior $N_{\rm H}$ with a mean of $10^{24}\,{\rm cm}^{-2}$ and a logarithmic FWHM of 2 dex. This is based on the evidence presented by Alexander et al. (2005) that IRAS 10214's nucleus must be Compton-thick given the [O III] line strength and the 1-2 dex deviation from the [O III]- $L_{\rm X}$ correlation. If the obscuring gas column density is significantly larger than $N_{\rm H} \sim 10^{25}$ cm^{-2} then our assumption breaks down and the bolometric luminosity derived here is likely to be too low. If one assumes the X-ray luminosity is dominated by the AGN and not star formation then the $L_{\rm OIII}$ shows that the hydrogen column density cannot be significantly higher (i.e. $>> 10^{25}$ cm^{-2}).

Under these assumptions, we find $\log{(N_{\rm H})}\ =\ 23.5{\pm}^{0.4}_{0.2}{\rm cm}^{-2}$. By comparison with the model type-I X-ray spectrum we can estimate the intrinsic X-ray luminosity of IRAS 10214 and therefore the intrinsic bolometric luminosity. We find $L_{\rm bol,Xray}\ =\ 1.3\ {\pm}^{1.2}_{0.7} \times 10^{39}\,\mu_{\rm X}^{-1}$ W ($3.4\ \times\ 10^{12}\,\mu_{\rm X}^{-1}$ L$_{\odot}$), where $\mu_{\rm X}$ is the magnification of the X-rays emanating from the AGN core. We do not have a strong constraint on the magnification of this unresolved X-ray detection, however, as an indicative estimate, we assume that $\mu_{\rm X}$ = $\mu_{\rm EVN}$, which yields an intrinsic bolometric estimate $L_{\rm bol,X} = 5.3\ {\pm}^{5.1}_{3.0} \times\ 10^{10}$ L$_{\odot}$. We emphasise that this X-ray magnification could vary substantially from the assumed magnification since micro-lensing is observed in X-ray emitting regions of AGN (e.g. Pooley et al., 2007; Chen et al., 2012), but not frequently in the radio emitting region (e.g. Koopmans et al., 2003), suggesting that the former are constrained to smaller regions than the latter. However, co-spatial regions smaller than the VLBI core will tend to a magnification of $\mu \sim 68$.

The 20-30 ks observations here combined with the magnification ($\mu \sim 68$) make this almost equivalent to the most sensitive X-ray field ever observed (Chandra Deep Field South, 4 Ms), however the lack of spectral resolution results in large degeneracies (particularly due to the scattering fraction) which are overcome to some extent with our assumed priors. Further progress will only be achieved with greater depth and spectral coverage/resolution.

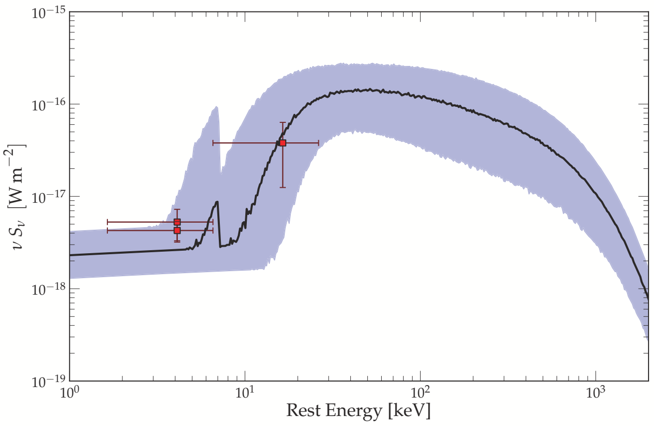

Figure 5.7: Best-fit X-ray model spectrum to the Chandra and XMM-Newton space telescopes. The shaded region corresponds the 68% confidence levels of the hydrogen column density ($N_{\rm H}$) and quasar bolometric luminosity ($L_{\rm bol}$). The bands correspond to 0.5-2 keV and 2-8 keV.

In Fig. 5.6 we show the 2D posterior PDF of the X-ray derived hydrogen column density ($N_{\rm H}$) and bolometric luminosity, which illustrates the degeneracy between these two parameters (below the Compton Limit). Over-plotted are two dashed red lines that indicate the two dust bolometric luminosity estimates. The blue horizontal line and shading indicate the [O III] $L_{\rm bol}$ estimate along with its 68% confidence levels. Finally, the green dashed line shows the estimate based on the scattered quasar light. While the uncertainty is large in all of the above methods ($\sim 0.3-0.5$ dex), they all show a reasonably consistent picture of a hidden quasar with intermediate luminosity. Furthermore, our two highest estimates are the luminosities we expect to be most contaminated by star formation (i.e. the 210 K dust and $L_{\rm OIII}$ bolometric luminosity estimates).

The five methods here are based on high-exposure space telescope observations and so it is challenging to see where we will make substantial progress in determining the bolometric luminosity of obscured quasars like IRAS 10214 before the next generation of telescopes or extended, dedicated programmes with current facilities. We adopt a quasar bolometric luminosity that is the weighted mean of the five methods presented here, which results in a value of $\log_{10}(\langle L_{\rm bol,QSO}\rangle/{\rm L}_\odot) = 11.34 \pm 0.27$, however, we stress the myriad systematic uncertainties associated with each method.

5.5.5 Black Hole Mass

As discussed in Chapter 3 and §1, Goodrich et al. (1996) found IRAS 10214 to have polarised broad emission lines (C III, C IV, Ly-α/N V) with Keck spectroscopy. Under the standard quasar unification model (Antonucci, 1993), this is consistent with a dusty toroidal structure obscuring a direct view of the AGN core and its associated broad-line region. A fraction of BLR emission is however, scattered off dust and electrons into the observer's line of sight. This polarises the radiation providing a very useful tool in the dissection of AGN. Dust of course reddens the scattered radiation, whereas electrons do not alter the spectrum of the incident radiation with any wavelength dependence. Discerning the nature of the scatterers is possible in principle, however not at present in the case of IRAS 10214 due to the low S/N polarised spectrum.

Goodrich et al. (1996) measured a polarised C IV line-width of $\Delta \mathrm{v}_{\mathrm{CIV}} \sim 6000\ \mathrm{km\,s^{-1}}$. Following the Vestergaard & Peterson (2006) calibration, the black hole mass can be estimated from the C IV velocity width via:

$$\begin{aligned} \log\left(M_{\mathrm{BH}}(\mathrm{CIV})\right) &= \log\left(\left[\frac{\Delta V_{\mathrm{CIV}}}{1000\ \mathrm{km\,s^{-1}}}\right]^2 \left[\frac{\lambda L_\lambda(1350)}{10^{44}\ \mathrm{ergs\,s^{-1}}}\right]^{0.53}\right) \\ &\quad + (6.66 \pm 0.01) \end{aligned} \tag{5.3}$$

We determine the value $\nu L_{1350} = 7.3 \times 10^{37}$ W based on the quasar bolometric luminosity derived in §5.5.4 and an average quasar spectrum (Elvis et al., 1994). This yields a black hole mass of $\log_{10}(M_{\mathrm{BH}}/\mathrm{M}_\odot) = 8.36 \pm 0.56$. Even with this large uncertainty, this places the black hole mass two orders of magnitude above the 'knee' (M^* value) of the $z = 0$ black hole mass function, however it is certainly not amongst the most massive black holes ($> 10^9\ \mathrm{M}_\odot$) observed at this epoch and earlier (e.g. Kurk et al., 2007). Based on this black hole mass and the mean quasar bolometric luminosity derived in § 5.5.4, we can estimate the Eddington Ratio,

$$\begin{aligned} \eta &= \langle L_{\mathrm{bol}} \rangle / L_{\mathrm{Edd}} \qquad (5.4) \\ &= 2.2 \times 10^{11}\ \mathrm{L}_\odot / 7.4 \times 10^{12}\ \mathrm{L}_\odot \\ &= 3^{+7}_{-2}\ \text{percent.} \end{aligned}$$

This indicates (even with the large uncertainty) that the accretion is well below the typical 10% level for actively accreting, radio-loud quasars.

While there is some contention on the validity on the use of the C IV FWHM as a black hole estimator (e.g. Baskin & Laor, 2005; Shen et al., 2008; Croom, 2011), the polarised C IV line is perhaps the most accurate black hole mass estimator we have at our disposal for this obscured quasar. We emphasise the large uncertainty of 0.56 dex as well as the caution raised by Baskin & Laor (2005) regarding the use of the C IV FWHM in black hole mass estimates. Included in this uncertainty is the inclination dependency, since the broad-line region has been shown to be more disc-like rather than spherical (see discussion in Jarvis & McLure, 2002, 2006, and references therein). This is the first estimate of the black hole mass in IRAS 10214 and is arguably the most accurate possible with the available data.

As a consistency check, we estimate the black hole mass, using a second, significantly less secure method based on the rest-frame 5 GHz luminosity and Eddington rate ($L/L_{\rm Edd}$, Lacy et al. 2001), based on their derived correlation between black hole mass and radio luminosity in the analysis of 60 quasars selected from the FIRST[7] Bright Quasar Survey (FBQS; Gregg et al., 1996; White et al., 2000). Their correlation is re-arranged as follows:

$$\log_{10}(M_{\rm BH}) \quad = \quad \frac{\log_{10}(L_{\rm 5GHz}) - 1.0\log_{10}(L/L_{\rm Edd}) - 7.9)}{1.9}, \tag{5.5}$$

where $M_{\rm BH}$ is in units of $M_\odot$ and $L_{\rm 5GHz}$ is in units of $\rm W\,Hz^{-1}\,sr^{-1}$. The scatter in this relation is very large (1.1 dex), since a number of important physical effects are neglected such as black hole spin and Doppler-brightening (Jarvis & McLure, 2002). Nonetheless, Equ. 5.5 does provide an indicative black hole mass, which we calculate to be $\log_{10}(M_{\rm BH,5GHz}/M_\odot) = 8.5 \pm 1.1$, assuming the *EVN* 1.66 GHz (rest-frame 5.5 GHz) flux density of $S_{\rm int} = 220 \pm 37$ μJy, its derived magnification of $\mu_{EVN} = 68$, and the accretion rate $L/L_{\rm Edd} = 3\%$ as derived earlier in this section. The latter assumption is circular to a degree, since it is dependent on the C IV derived black hole mass. However, as we will show, an accretion rate of $\gtrsim$ 0.5% is still consistent with our physical conclusions at the end of this section. The good agreement is encouraging, however we use the C IV FWHM estimate for the remainder of the this thesis since this method

---

[7] Faint Images of the Radio SKy at Twenty cm, http://sundog.stsci.edu

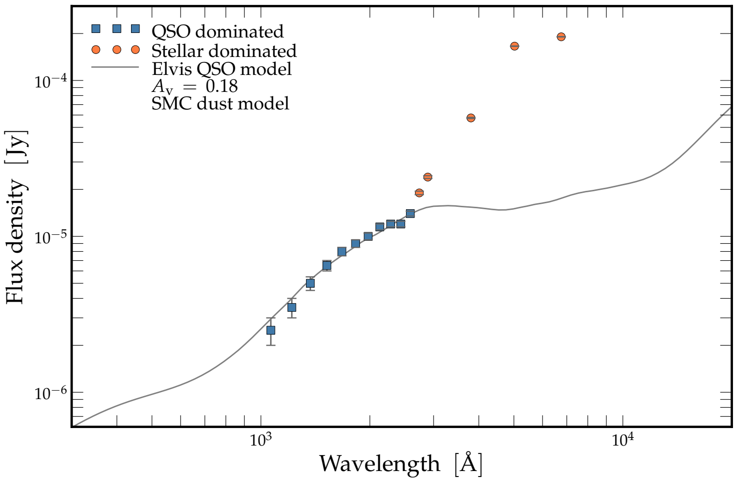

Figure 5.8: Ultraviolet fit to a reddened quasar model. The dust extinction model is from Pei (1992) and the intrinsic quasar model is an average from the sample of Elvis et al. (1994). While the Small Magellanic Cloud grain model fits best, there is little difference when compared with the other grain models. Only the blue squares are included in the fit as these are presumed to be dominated by scattered quasar light, as suggested by the high degree of polarisation. We argue that orange circles are dominated by the host galaxy's stellar component which is supported by the lower magnification seen at rest-frame optical/NIR wavelengths (as surmised from lower arc to counter-image flux ratios).

is significantly more robust.

5.6 Conclusions

We have performed a deep ($\sigma = 23\,\mu\mathrm{Jy\,beam^{-1}}$), 1.7 GHz *EVN* observation on IRAS 10214, a lensed $z = 2.3$ obscured quasar with prodigious star formation. The VLBI observation provides a brightness temperature filter and allows us to image the obscured active nucleus with an effective angular resolution of $\lesssim$ 50 pc at $z = 2.3$, after correcting for gravitational lensing. These *EVN* observations permit a number of conclusions to be drawn:

1. The AGN core as traced by the *EVN* 1.7 GHz detection has a flux density peak of $S_{\mathrm{peak}} = 209 \pm 23\,\mu\mathrm{Jy\,beam^{-1}}$ which makes up ~20% of the total 1.7 GHz flux density of a *MERLIN* map presented in Chapter 3. The *EVN* detection appears unresolved, with an integrated flux density of $S_{\mathrm{peak}} = 220 \pm 37\,\mu\mathrm{Jy}$. The remainder of the *MERLIN* 1.7 GHz flux is likely to be split between star formation and large-scale ($\gtrsim$200 pc) jets.

2. The fact that the AGN core is a single detection and is northward of the *HST* F814W arc strongly advocates that the *HST* F814W arc is not a triple-image system that is merged by the *HST* PSF. This supports the lens model derived by Chapter 3 which suggests that the *HST* F814W map is comprised of a single arc with the observed double peak coming from intrinsic structure at rest-frame ultraviolet wavelengths.

3. The AGN core is located at a position qualitatively consistent with the spatially resolved polarisation properties of the ultra-violet map reported in Nguyen et al. (1999). Moreover, it is consistent with their predication of the active nucleus' position based on the polarisation properties and the more northernly *HST* F437M centre of curvature which is explained by more efficiently scattering of ultraviolet photons and therefore a closer proximity to the quasar.

4. If the AGN core position and size is well approximated by the radio core detected in this *EVN* observation, then the AGN is preferentially magnified by over an order of magnitude when compared to a spatially resolved *JVLA* CO $(1\to0)$ map, where the latter can be used a star formation proxy. This confirms the effective 'chromacity' of this strong-lensed system, which is caused by different emission regions undergoing differing magnification boosts due to their relative size and position. This effect may be particularly relevant in the case of far-infrared (FIR) bright, strongly-lensed galaxies recently discovered by the *Herschel Space Observatory* (Negrello et al., 2010).

5. The roughly consistent positions of the CO $(1\to0)$ peak and radio core support the argument presented in Chapter 4 that the high-J CO lines emanate from a region centred on the active nucleus.

6. The configuration of the *EVN* core and *HST* ultraviolet arc support our previous claim that this is an asymmetric (or one-sided) source where we observe the line-of-sight NLR, whilst the 'counter-NLR' is obscured by a significant host dust reservoir, consistent with examples in in the nearby Universe (e.g. Liu & Pooley, 1991; Simpson et al., 1997).

7. We derive a black hole mass of $\log_{10}(M_{\rm BH}/{\rm M}_{\odot}) = 8.36 \pm 0.56$ and a bolometric luminosity $\log_{10}(\langle L_{\rm bol,QSO}\rangle/{\rm L}_{\odot}) = 11.34 \pm 0.27$ dex, which suggests a low accretion rate $\eta \sim 3^{+7}_{-2}\%$, albeit with significant uncertainty.

These results point toward a intermediate luminosity AGN, however our X-ray modelling find it to be a highly obscured nucleus (and perhaps Compton thick). The mean hydrogen column density $\overline{N_{\rm H}} \sim 10^{23.5}\,{\rm cm}^{-2}$ explains the excessive [O III]5007 luminosity in comparison with the derived X-ray luminosity (Alexander et al., 2008). This X-ray modelling predicts a strong Fe K line to be observed if the required sensitivity is achieved. The unobscured, intrinsic quasar bolometric luminosity ($2.2 \times 10^{11} L_{\odot}$) is well supported with independent bolometric luminosity estimates. Comparison of this approximate $L_{\rm bol}$ suggests inefficient, sub-Eddington accretion onto the central black hole.

This case study is not only a clear demonstration of the significant SED distortion due to preferential lensing, but also a preview of the sensitivity to be achieved with the *SKA* which will detect large samples of low-luminosity AGN ($L_{\rm 5GHz} \lesssim 10^{22}$ W Hz^{-1} sr^{-1}). These will be pivotal surveys to characterise AGN activity over cosmic time, particularly for the obscured AGN population.

CHAPTER 6

THE HOST GALAXY

In Chapters 3-5 we analysed maps that were argued to be dominated by the radio core, radio jet, scattered quasar light as well as the CO $(1\rightarrow0)$ extent. In this chapter we investigate the stellar component. We will refer to the putative developed stellar component loosely as the 'host' galaxy. Evidence for a significant host galaxy component was first provided by the 4000 Å break identified by Lacy et al. (1998). However, the relative fraction of host and AGN contributions in optical/NIR imaging is uncertain. The clear identification of the host galaxy is important for a number of reasons. It will enable a magnification estimate and therefore a tighter constraint on the intrinsic stellar mass in IRAS 10214, as well as the ratio of the black hole to stellar bulge mass (or spheroid mass as referred to by some authors). This value is typically $M_{\rm BH}/M_{\rm bulge}$ ~0.1-0.5% at $z\sim0$ (e.g. Marconi & Hunt, 2003; Häring & Rix, 2004), but found to increase at high-redshift, albeit with large uncertainty (Bennert et al., 2011). The latter result suggests that black hole growth precedes the full development of the stellar component to some degree, an important clue in the field of galaxy evolution.

The host galaxy is best targeted red-ward of the 4000 Å break and therefore long-ward of an observed wavelength $\lambda_{\rm obs} > 1.32\ \mu$m. Fortuitously, there is a deep, unpublished *HST* F160W (1.6 μm) map available in the *HST* archive. This chapter presents this observation; attempts to isolate the host galaxy to recover its source-plane properties; and in turn estimate its black hole to stellar mass ratio.

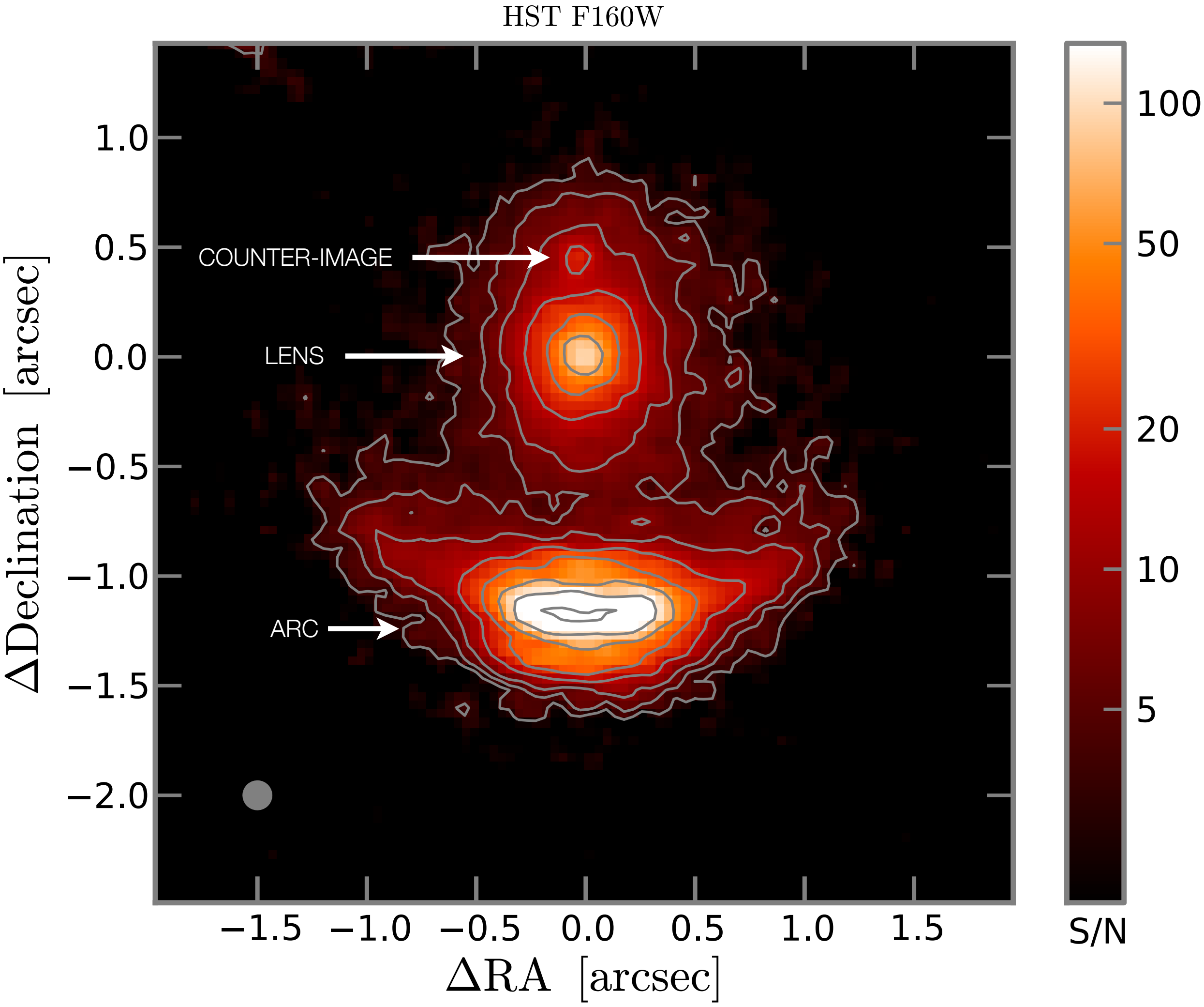

Figure 6.1: *HST* F160W map with lensing galaxy, counter-image and the arc. The integrated arc/counter-image flux density ratio is $\breve{\mu}$ ∼69 ±7. The HST PSF through this filter has a FWHM of ∼150 mas which is illustrated by the grey circle in the lower left. Note that the color-scale is logarithmic to enhance the extended low surface brightness arc.

6.1 *HST* F160W Observation

The *HST* F160W observations of IRAS 10214 were introduced in Chapter 2. Here we show an enlarged version (Fig. 6.1) which reveals an extended arc structure; the lens; as well as a counter-image to the north of the lens centroid. Comparison with the *HST* F814W map shows a higher S/N. The detection of the counter-image has higher significance than the *HST* F814W map and a arc/counter-image flux ratio of $\breve{\mu} = 69 \pm 7$, a value that is still likely to be an overestimate due to differential extinction since this is rest-frame *B*-band emission. The arc appears to have two discernible components: an extensive, faint arc, as well as second component protruding both north and south of the extended arc's centre of curvature. There appears to be some asymmetry south-east of the arc.

The exquisite detail in this deep map suggests that there is complex structure recovered with the *HST* F160W 150 mas resolution. We make the simplified assumption that the map is dominated by the host galaxy which is loosely supported by the global SED (Fig. 3.4), as well as the 4000 Å break first identified by Lacy et al. (1998). However, we note that the map is likely to include a contribution from the scattered QSO light, which we revisit upon inspection of the image-plane residuals.

6.2 Source Plane Inversion

The same lens modelling procedure performed on the two resolved radio maps, the CO $(1\to0)$ map, and the *HST* F814W map in Chapters 3 and 4 is repeated on the *HST* F160W map. The lens model is fixed to the Lens Model A values in Table 2.2. As we have argued above, the map appears to have two distinct components (extended stellar host + QSO/NLR emission). For this reason, we attempted many variations of the lens inversion in an attempt to isolate what is of particular interest in this chapter: the host galaxy. The first step was to fit a single component, spherically-symmetric, Gaussian profile for ease of comparison with the *HST* F814W and other radio maps. The spherical symmetry assumption was then relaxed, including two additional free parameters (projected source ellipticity and major axis position angle). This was followed by a number of different approaches, which included varying the Sersic index, the addition of a second Sersic component (fixed and free), and clipping of the data to fit only the extended, low surface brightness emission. These alternative approaches were met with limited success, most likely due to the simplicity of

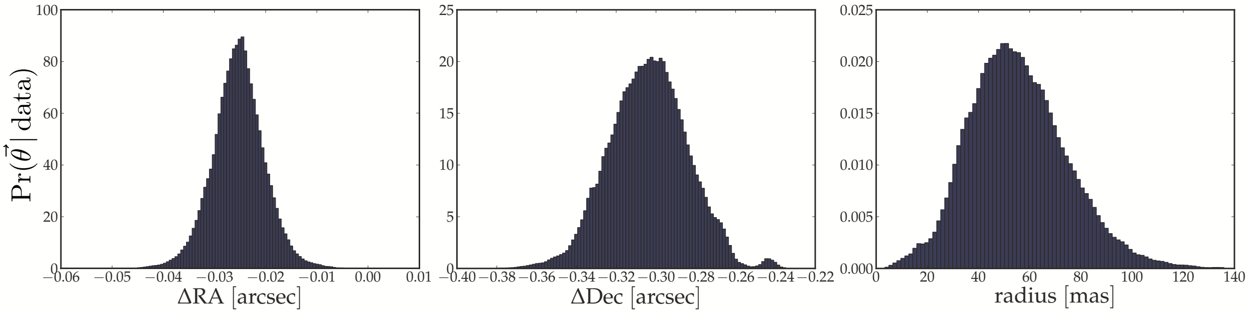

Figure 6.2: Marginalised posterior PDFs of the source plane parameters (RA, Dec, scale radius) given the *HST* F160W data and a single Gaussian source-plane model. The radius is $\sim 20\%$ larger than the *HST* F814W source-plane radius. The magnification is $\mu_{\rm F160W} = 14.0^{+2.0}_{-1.5}$.

the source profile model, given such high S/N data. Nonetheless, we present two of these attempts below as a first step towards disentangling the host galaxy in IRAS 10214, an objective that we believe will ultimately require a non-parametric lensing inversion approach.

6.2.1 Spherically-Symmetric Gaussian Component

As in Chapter 2, this model has three free parameters: the source's centroid coordinates (*RA*, *Dec*) and scale radius ($r_{\rm s}$). Uniform priors are assumed for these three parameters. Once again, we assume a Gaussian, spherically-symmetric source profile. In Fig. 6.2 we show the posterior PDFs of the source-plane model parameters. The centroid is consistent with those derived in § **??**, but the scale radius is 20% larger than the *HST* F814W source-plane component, as would be expected if this traces the stellar component in a developed bulge.

The residuals that result from this model (shown in Fig. 6.3) are reasonably poor with an average $\chi^2_\nu \sim 8.6$, suggesting that the analytic profile may not be appropriate. More specifically, the residuals have negative values east and west of the *HST* F160W peak emission; while positive residuals north and southward. The amplitude of, and symmetry in, the residuals suggests that there are multiple physical components and/or complex structure at this wavelength.

An additional MCMC run was performed with the Sersic index included as a free parameter. The result was a distribution peaked at $n = 0.5$ (Gaussian, the lowest index in the allowed parameter space), and tailed off rapidly to higher Sersic indices. This showed that under this model, a Gaussian profile is overwhelmingly favoured against higher Sersic values. Lower Sersic values were not explored since the physical motivation

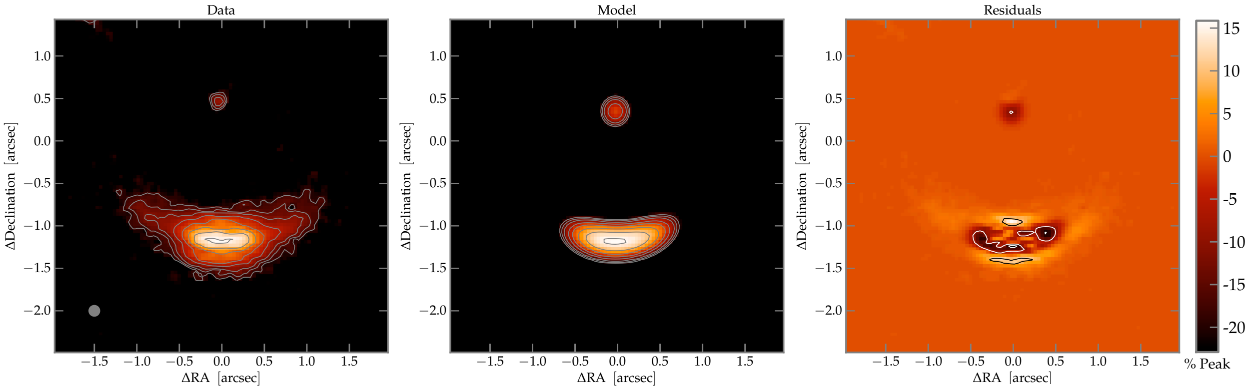

Figure 6.3: *HST* F160W data, model and residuals assuming the single Gaussian source-plane model. The data and model frames have logarithmic colour-scale to emphasise the extended emission. The residuals have a linear scale which is scaled to a percentage of the data maximum.

for this does not have strong empirical justification.

The north-south and east-west symmetry seen in residuals motivates our second test: an ellipsoidal source model.

6.2.2 Ellipsoidal Gaussian Component

This test is run in precisely the same manner as in §6.2.1, however, we assume an ellipsoidal Gaussian profile, which introduces two additional parameters: the projected source ellipticity ($\varepsilon_{\rm S}$) and semi-major axis position angle (*PA*). In Fig. 6.4 we show the posterior PDFs of the source-plane model parameters. Again, the centroid is consistent with those derived in § **??**. The values shown in the semi-major axis of the ellipsoid (Fig.6.4, top right panel) represent the scale-radius along the major axis. The position angle of the semi-major axis is $PA = 22^\circ \pm 29^\circ$ east of north, which is physically consistent with the CO (1→0) disk suggested in Chapter 4, which we argued has a semi-major axis position angle of $PA_{\rm CO} = 16^\circ \pm 7^\circ$ (east of north), yielding confidence in the result.

In Fig. 6.5 we show the *HST* F160W magnification posterior PDF, using the same method described in Chapter 3. The mean *HST* F160W magnification is $\mu_{\rm F160W} = 14.1^{+1.6}_{-1.2}$, which is ∼ 33% lower than the *HST* F814W map magnification derived in Chapter 3.

The residuals are shown in Fig. 6.6 (right panel), the model used is that which has the peak value of all posterior PDFs. The lowest χ^2_ν value is ∼ 20% lower than that of the spherically-symmetric model

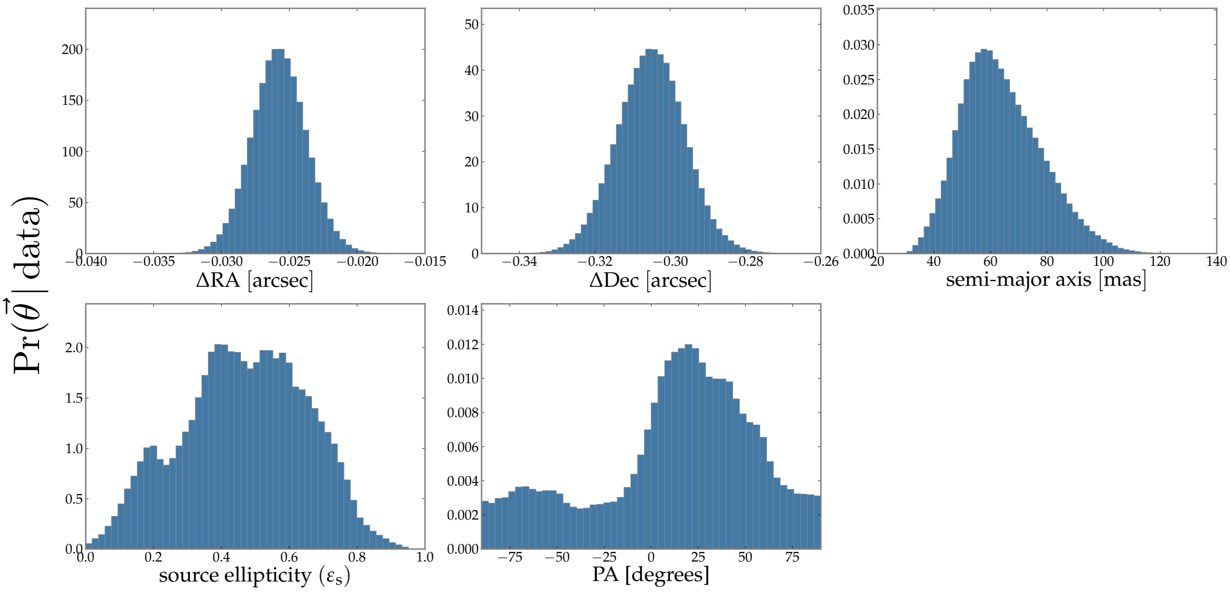

Figure 6.4: Marginalised posterior PDFs functions of the source plane parameters (RA, Dec, scale radius, projected source ellipticity, position angle), given the *HST* F160W data. This assumes an ellipsoidal, Gaussian-profile source-plane model. The mean semi-major axis has a physical scale of ∼0.5 kpc

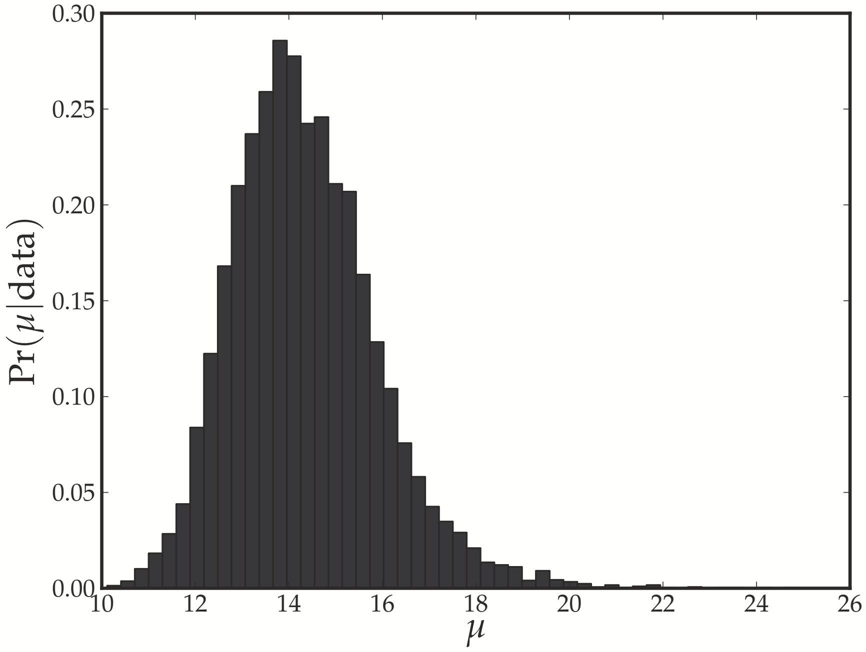

Figure 6.5: Magnification posterior PDF, given the *HST* F160W data. This PDF is generated in precisely the same manner as described in Chapter 3. The *HST* F160W map magnification PDF has a mean of $\mu_{\mathrm{F160W}} = 14.1^{+1.6}_{-1.2}$, which is 33% lower magnification than that derived for the *HST* F814W map.

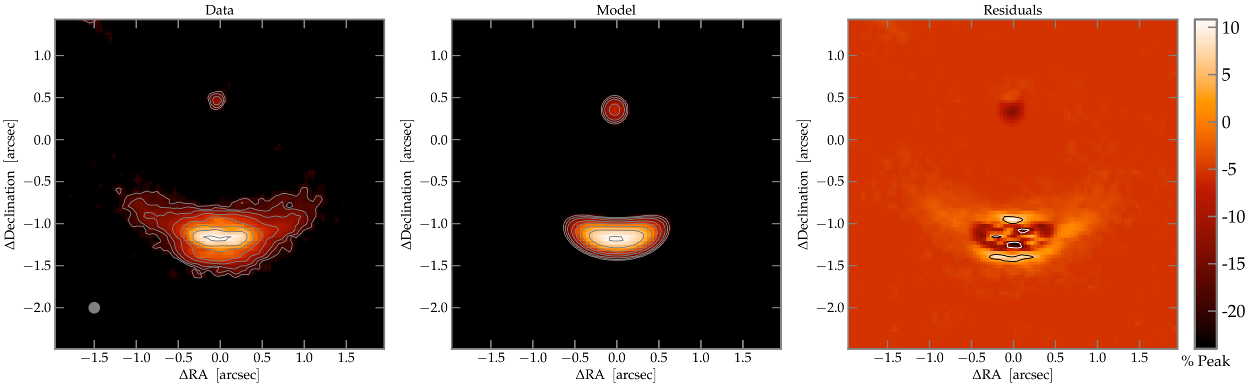

Figure 6.6: *HST* F160W data, model and residuals assuming the ellipsoidal Gaussian source-plane model. Colour-scaling is identical to Fig. 6.3.

($\chi^2_{\nu,\mathrm{min}} = 5.53$), and the average $\chi^2_\nu = 7.5$, roughly 12% lower than the spherically-symmetric model assumed previously. Qualitatively, the residuals appear more symmetric about the vector joining the centre of the arc and the counter-image. The deep, east-west negative regions seen in the spherically-symmetric model have much lower magnitude, however the north-south regions of positive emission remain virtually unchanged. Promisingly, there are two peaks along the centre of curvature of the arc which are consistent with the structure seen along the *HST* F814W arc (east/west along the centre of curvature). This is illustrated in Fig. 6.7 where we have overlaid *HST* F814W contours on the re-scaled *HST* F160W residuals. In this figure, we include a green cross that indicates the location of the *EVN* detected radio core, which was presented in Chapter 5. Note that the cross length is a factor ~ 10 larger than the *EVN* positional uncertainty. Inspection of the *HST* F164N map, a narrow band filter centred on the redshifted [O III]λ5007Å line, shows north-south components at the 10% level which are consistent with the *HST* F160W residuals (Simpson et al., 2012, in prep.).

Although the physically consistent results of the ellipsoidal model are encouraging, the residuals remain large. As discussed, we attempted many additional methods, however none achieved lower χ^2_ν values than the simple ellipsoidal Gaussian profile. We now discuss the physical interpretation of this, our most successful model, and close with an outline of more sophisticated models to be pursued in the future. We note that the magnifications of the spherically-symmetric and ellipsoidal are consistent within their uncertainties, and therefore we neglect a quantitative model selection procedure (i.e. calculate the *evidence* and Bayes' Factor of the two models) since this is computationally expensive and does not impact on the intrinsic properties.

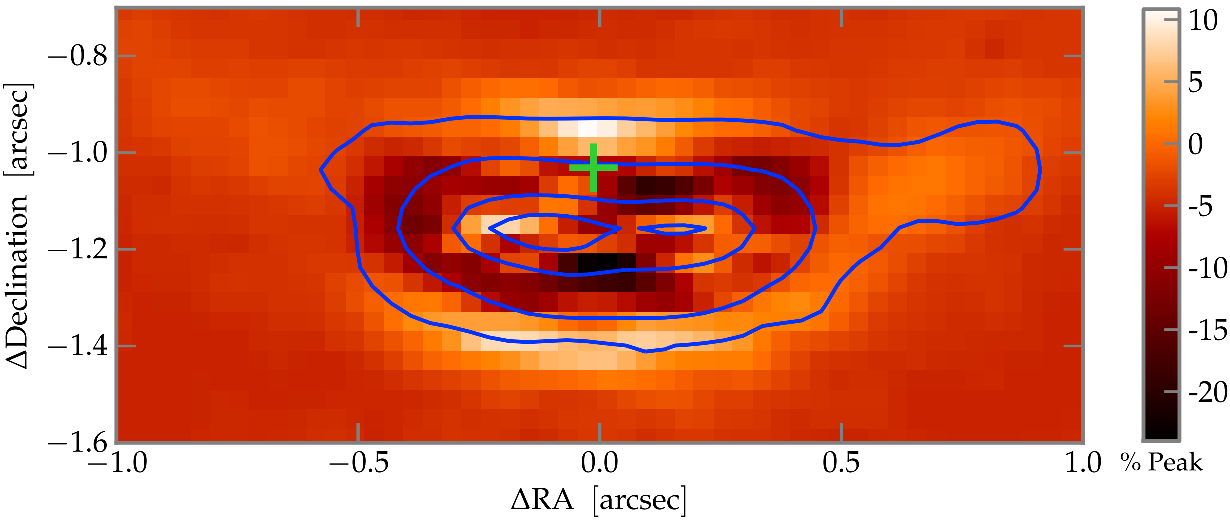

Figure 6.7: *HST* F160W residuals assuming the ellipsoidal Gaussian source-plane model, with the *HST* F814W map contours overlaid. The two peaks along the *HST* F814W centre of curvature are roughly consistent with the residual peaks. The green cross indicates the image-plane position of the *EVN* radio core presented in Chapter 5.

6.3 Tentative Einstein-Ring?

Here we investigate the more extended, lower surface brightness emission in the *HST* F160W map. In Fig. 6.8 we show the map convolved with a 2D Gaussian with FWHM = 0.5 arcsec. This map has been generated by subtracting a single Sersic component from the lens; as well as a PSF component of the residual core, both of which are discussed in §2.1.2. The map is then convolved with the 0.5 arcsec 2D Gaussian, followed by a 2-σ clip, based on the local, Gaussian-smoothed noise.

The result shows tentative evidence that a full, or at least part Einstein ring may be present in the map. We stress that the lens subtraction scheme (using GALFIT2, see §2.1.2) could artificially create such a feature, through the over-subtraction of lens galaxy flux and a subsequent positive or negative annulus centred on the lens galaxy. However, there does appear to be some, albeit tenuous, low surface brightness CO (1→0) emission evident, that corroborates the putative (part-)Einstein ring. As can been seen in the CO (1→0) channel maps (§4.2), there is arc-like emission towards the north-west of the arc (due west of the lens centroid). The rough consistency of the convolved *HST* F160W map with that seen in the CO (1→0) total intensity and channel maps suggests it is real, and likely a part of a larger, lower surface brightness Einstein ring of emission. An upcoming *JVLA* *C*-band observation at 0.3 arcsec spatial resolution will

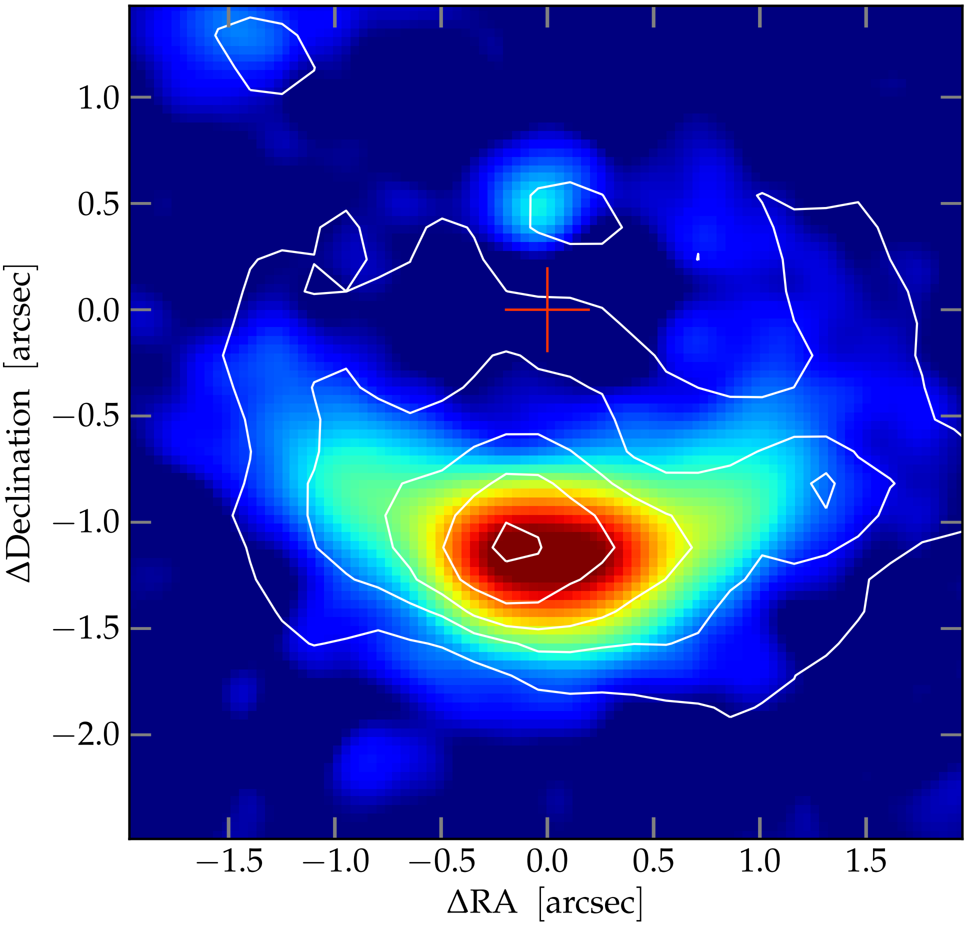

Figure 6.8: *HST* F160W map convolved with a 2D Gaussian with FWHM of 0.5 arcsec to enhance low surface brightness emission. Overlaid are the same CO (1→0) contours from Fig. 4.1. This shows some correlation between the western emission that links the arc to the counter-image. The purpose of this figure is not necessarily to suggest the molecular gas is con-spatial with the NIR imaging, but rather to probe the low surface brightness emission of two of our resolved maps which we expect to be the most extended in the source plane (and therefore are the most likely to form an Einstein ring.

be able to probe this further, however, deep, AO-assisted NIR imaging is required to exploit the lensing constraints provided by such a ring.

6.4 Black Hole-Spheroid Mass Ratio

The two black hole mass estimates are within 0.15 dex of one another, however the uncertainties are large (0.56 dex and 1.1 dex for the C IV and $L_{5\mathrm{GHz}}$ estimates respectively). Nonetheless, this allows us to calculate the BH-to-stellar mass ratio if we can put a constraint on the intrinsic stellar mass[1] in IRAS 10214.

This value is typically $M_{\rm BH}/M_{\rm spheroid}$ ~0.1-0.2% at $z \sim 0$ (e.g. Merritt & Ferrarese, 2001; Marconi & Hunt, 2003; Häring & Rix, 2004), but found to increase for high-redshift quasars, albeit with large uncertainty, by a number of authors (Peng et al., 2006; McLure et al., 2006; Treu et al., 2007; Bennert et al., 2011).

Peng et al. (2006) investigated a sample of 31 gravitationally-lensed and 20 non-lensed AGN and found that the $M_{\rm BH}/M_{\rm bulge}$ mass increased by a factor of $\gtrsim 4\pm^{2}_{1}$ for $z > 1.7$, however cautioned that it may be consistent with no evolution. McLure et al. (2006) performed a similar study with the 3CRR sample (Laing et al., 1983), a sample of 170 radio-loud, low-frequency selected AGN. They found an evolution of $M_{\rm BH}/M_{\rm spheroid} \propto (1+z)^{\alpha}$ where $\alpha = 2.07 \pm 0.76$. Treu et al. (2007) and Bennert et al. (2011) find a consistent values of $\alpha = 1.5 \pm 1.0; 1.96 \pm 0.55$ for samples with mean redshifts of $z \sim 0.36$ and $z \sim 2$ respectively. The former sample was made up of 20 Seyferts, while the latter comprised of 11 X-ray selected, broad-line AGN in a GOODS-N/S sample. There are clearly a number of independent studies that suggest quasar black hole growth precedes the full development of the stellar component to some degree, however, selection biases could yield similar results, as argued in Lauer et al. (2007).

We assume the magnification $\mu_{\rm stellar} = 14.1\pm^{1.6}_{1.2}$, derived from a deep *HST* F160W map in Deane et al. (2012d, in prep.), however, we re-emphasise the associated systematic uncertainty described in Chapter 2 which is in the range of 20-40%.

Spectrally-derived stellar mass estimates are challenging in the case of IRAS 10214 since the emission is AGN-dominated in the near-UV and the near-IR with an ill-defined transition into the stellar dominance at optical wavelengths, evidenced by the Balmer break detected in Lacy et al. (1998). Ideally, we would make a mass estimate in the NIR, however the lens galaxy makes a substantial, yet unconstrained, contribution at this wavelength (Verma et al., 2012, in prep.). A compromise is to make a coarse estimate from a single filter that we believe is dominated by stellar continuum emission. This approach leaves extinction unconstrained, however, provides an indicative stellar mass. We adopt the *HST* F212N magnitude of $m_{\rm F212N} = 19.63 \pm 0.34$ determined by Simpson et al (2012, in prep.) since this wavelength is a less biased tracer of stellar mass and it is the only *HST* filter free of line contamination (Simpson et al, 2012, in prep.).

---

[1] Since we cannot distinguish between the host and the spheroid in IRAS 10214 with reasonable confidence, we assume the spheroid mass is dominated by the stars. The source-plane scale radius of the *HST* F160W component in Deane et al. (2012d, in prep.) is $r_{\rm s} \sim 500$ pc, which is broadly consistent with this expectation.

The stellar magnification and *HST* F212N magnitude allow us to make a coarse comparison with the K-band luminosity function in Cirasuolo et al. (2010). This suggests the apparent mass of the IRAS 10214 stellar component is $M_{\rm stellar,10214} = 20.9 M^{*} \mu^{-1}$, where M^{*} is the characteristic stellar mass at $z \sim 2.3$. Assuming the *HST* F160W magnification $\mu_{\rm F160W} = 14.1 \pm^{1.6}_{1.2}$, we estimate an intrinsic stellar mass of $M_{\rm stellar} = 1.5 M^{*} = 1.5 \times 10^{10.7} = 7 \times 10^{9}$ M$_{\odot}$, where the value of $M^{*} \simeq 10^{10.7}$ M$_{\odot}$ is the characteristic stellar mass at $z \sim 2$ (e.g. Ilbert et al., 2010).

Our dynamical and gas mass estimates in Chapter 4 imply a stellar mass of $M_{\rm stellar,dyn} = 6.5 \times 10^{9}$ M$_{\odot}$, in good agreement with our *HST* F212N estimate despite the coarseness of both approaches. This rough stellar mass enables an estimate of the central super-massive black hole to stellar mass ratio, $M_{\rm BH}/M_{\rm stellar} = 0.03$. This is over an order of magnitude larger than the typical ratio found at $z \simeq 0$, however both are consistent with the suggested evolution of this relation for AGN host galaxies. For example, assuming $\alpha \sim 2 \pm 1$ (where $\alpha \propto M_{\rm BH}/M_{\rm spheroid}$), we expect an increase in the $M_{\rm BH}/M_{\rm spheroid}$ relation by a factor of $11 \pm^{25}_{8}$ at a redshift of $z = 2.3$, in agreement with the our derived values. Note that we assume the stellar mass dominates the total spheroid mass inside the $r_{\rm s} \sim 500$ pc source-plane scale radius which is significantly smaller than the CO $(1 \rightarrow 0)$ source-plane scale radius ($r_{\rm CO} = 5.7$ kpc) derived in Chapter 4.

Although the uncertainties are large, the overall picture strongly supports that the majority of the black hole growth precedes the full stellar mass assembly for this obscured quasar (assuming that IRAS 10214 will evolve to be consistent with the local $M_{\rm BH}/M_{\rm spheroid}$ relation). This is contrary to the 'under-massive' black holes masses measured in $z \sim 2$ SMGs by Alexander et al. (2008) and Biggs et al. (2010). Alexander et al. (2008) made $M_{\rm BH}$ estimates in 6 broad line SMGs using Hβ and Hα line-widths using the Greene & Ho (2005) viral estimator, and found that (a) they have black hole masses $\gtrsim 3$ times smaller than 'normal' galaxies in the local Universe of comparable mass; and (b) they have $\gtrsim 10$ times smaller than that predicted for $z \sim 2$ populations. Biggs et al. (2010) performed a VLBI survey of 6 SMGs with a mean redshift of $z \sim 2$. They calculate black hole masses (and upper limits) based on the Lacy et al. (2001) $L_{\rm 5GHz}$ method and their 1.6 GHz VLBI observations of all 6 SMGs. Although the uncertainty is very large (1.1 dex), all 6 of their objects have black hole masses (or upper limits) that are $\sim 0.2 - 1.3$ dex *below* that expected based on the Häring & Rix (2004) finding that $M_{\rm BH}/M_{\rm spheroid} = 0.0014 \pm 0.0004$ in the local Universe.

Despite the large uncertainties, there appears to be 1-2 orders of magnitude difference between the black hole to stellar mass ratio in SMGs and the obscured quasar IRAS 10214. This tentatively implies very different evolutionary paths for these two object classes, despite their apparent similarities in many parts of the global SED. However, this may be a result of the selection bias outlined in Lauer et al. (2007), particularly since we demonstrate in this work that the AGN is preferentially magnified by an order of magnitude when compared to the spatially resolved *JVLA* CO $(1 \rightarrow 0)$ map in Chapter 4. For this reason, a significantly enlarged sample size, that has a demonstrably unbiased selection, is required to investigate this further.

6.5 Conclusions and Future Work

This chapter has presented the deep exposure *HST* F160W map and argued that although it contains multiple physical components (stellar host + scattered QSO light), it is plausibly dominated by a developed stellar component, the presence of which is evidenced by a clear Balmer break (Lacy et al., 1998). We have modelled the map with a simple, spherically-symmetric, and ellipsoidal Gaussian profiles yielding a $r_s = 0.5$ kpc component with a semi-major axis position angle consistent with that of the CO $(1 \rightarrow 0)$ semi-major axis. The preferred ellipsoid source model has a projected ellipticity $\varepsilon_s = 0.47 \pm 0.19$ and a position angle of $PA = 22^\circ \pm 29^\circ$. We find this ellipsoidal model has a magnification of $\mu_{\mathrm{F160W}} = 14.1^{+1.6}_{-1.2}$.

Our crudely derived black hole to spheroid mass ratios are consistent with the suggested evolution of this parameter in AGN host galaxies (Peng et al., 2006; McLure et al., 2006; Treu et al., 2007; Bennert et al., 2011). The $M_{\mathrm{BH}}/M_{\mathrm{spheroid}}$ ratio in IRAS 10214 is 1-2 orders of magnitude larger than that of $z \sim 2$ SMGs based on optical and radio analyses (Alexander et al., 2008; Biggs et al., 2010), providing a tentative suggestion that these two object classes may follow different evolutionary paths. However, this picture is sensitive to the large black hole mass uncertainties and selection effects (e.g. Lauer et al., 2007).

Despite the apparent physical consistency of these results, the large residuals from the array of tests performed advocates a more sophisticated, non-parametric approach where individual pixel intensities are the free parameters. Although this complicates comparison of the source-plane properties of different physical components, it will accurately reproduce complex structure. This has been developed, however under the current algorithm implementation, this pixelated scheme is computationally impractical, requiring more than a few weeks of processing time on a 2.4 GHz, dual core processor. While this processing time is not entirely unreasonable, it is the tuning of proposal distributions in the MCMC algorithm that reduces its feasibility. The pixelated lens reconstruction algorithm is certainly a desirable feature of the code that will be optimised and fully implemented in the future. There is a detailed image-plane analysis currently in progress (Simpson et al, 2012, in prep.), that investigates multiple narrow and broad-band *HST* imaging products.The results from this work will be very useful as a guide of what questions to ask of a more sophisticated *HST* UV-NIR lensing analysis.

CHAPTER 7

CONCLUSIONS

The conclusions from Chapters 2-6, which are stand-alone academic journal submissions, are well summarised and not repeated here. Instead, we give a qualitative synthesis of the major results of this thesis, illustrated by the cartoon in Fig. 7.1, which is a speculative, simplistic overview of what IRAS 10214 may resemble in the source plane. Note that physical components are not to scale, but merely attempt to synthesise the interpretation of the different emission regions probed in this thesis and their subsequent lensing inversions.

Starting with the largest scales, the cartoon in Fig. 7.1 shows a regularly rotating, $r_{\rm eff} \sim$4 kpc disk of cold molecular gas at an inclination angle $\lesssim$30°. Towards the west is a clump of CO (1$\rightarrow$0) that may be evidence of a minor merger in progress or very clumpy structure. Inside the CO (1$\rightarrow$0) disk is a stellar component with $r_{\rm eff} \sim 0.5$ kpc and a very similar position angle ($\sim 20°$ east of north). This stellar disk lies within a slightly larger radio lobe which is plausibly split between supernovae and radio jet emission. In the centre is the VLBI detected radio core which traces the $\sim 10^8$ $M_\odot$ SMBH, the position of which is consistent with the *HST* C IV narrowband imaging. There are bi-conical outflows from previous and/or current jet activity, which are traced by ultraviolet scattering off the NLR clouds, evidenced by highly polarised UV emission (28%). The NLR clouds illuminated by the counter-jet are heavily obscured relative to the observer due to the significant dust mass in the disk.

Perhaps the most important result of this work is the demonstration that the properties of lensed sources can be significantly distorted by preferential lensing effects. This is likely to be exaggerated to some degree

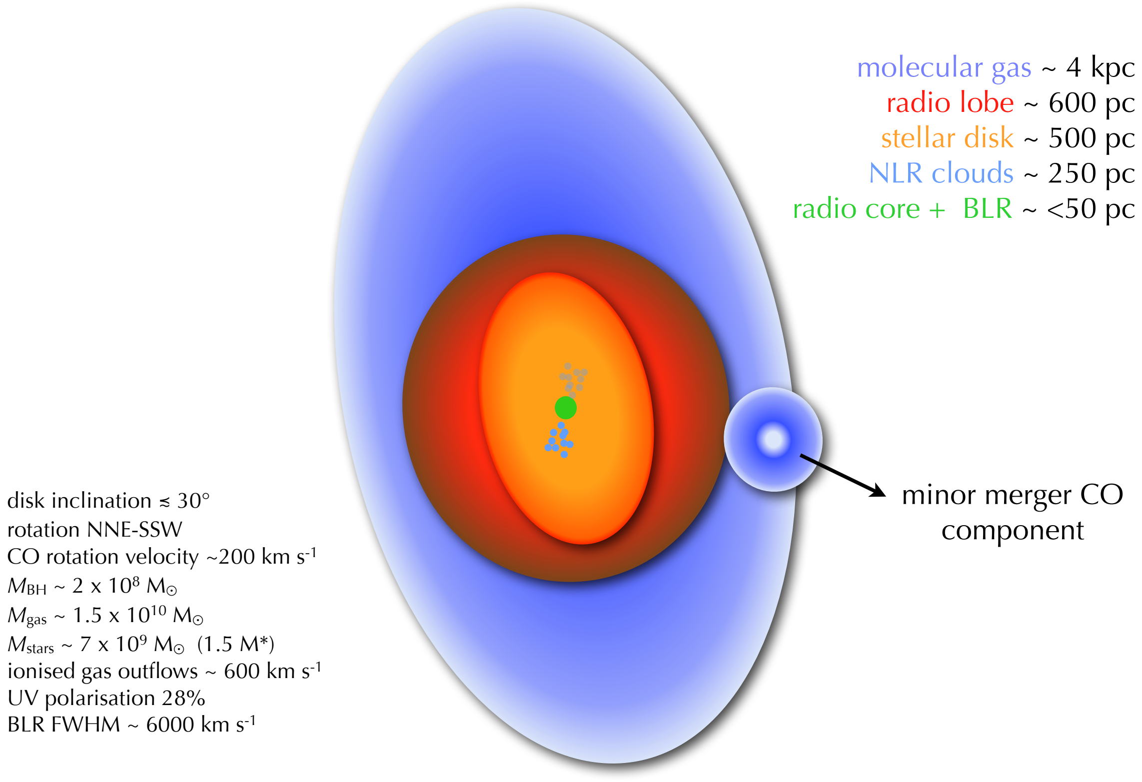

Figure 7.1: Speculative cartoon summary of the intrinsic (source-plane) structure of IRAS 10214. Note that physical components are not precisely to scale, but merely attempt to provide a qualitative overview. The quoted sizes correspond to the effective radii of the spherically symmetric source-models, except for the stellar disk which is the semi-major axis.

in IRAS 10214 since it is a cusp-caustic lens and has a selection function biased towards high-redshift AGN. Nonetheless, we have measured an apparent order of magnitude difference between the total magnification of the radio core and the cold molecular gas presumed to trace star formation. This suggests that chromatic distortions imposed by lensing, due to the differing sizes and proximity of emission regions to the caustic, is an important effect in strong-lensed systems with multiple, detectable emission components. This can only be efficiently investigated with deep, high resolution observations of a large sample of lenses with next-generation facilities.

Some of the results presented in this thesis also showed the gain in sensitivity of telescopes currently in commission / recently commissioned. The upgraded *Ka*-band receivers of the *JVLA* enabled the deep, spatially resolved CO $(1\rightarrow0)$ observation with just 3 h on-source integration time. The *EVN* observations were heavily reliant on the phase calibrator search carried by two *e-VLBI* sessions. These flexible, rapid-turnaround observations are a promising preview of the capabilities of a permanently linked *e-EVN*, and the *SKA*.

Despite the promise of next-generation facilities, many of the results here depended heavily on archival data (both published and unpublished). Most notably, the beautiful *HST* F160W map was unpublished. This is a remarkably high quality data product and was used to great effect in the lens modelling (indirectly) and in the attempt to isolate the host galaxy and estimate the black hole to stellar mass ratio. The two resolved radio maps in Chapter 3 were both observed in the early 1990s and still unpublished, but yet are competitive observations given their integration time and angular resolution. The full range of multi-wavelength results are essential to gain the broadest possible understanding of this galaxy by virtue of connecting results from different parts of the spectrum (e.g. *EVN* radio core position with spatially resolved ultraviolet polarimetry and CO $(1\rightarrow0)$ 'core' position).

Not only is the effective resolution and sensitivity of IRAS 10214 a preview of next-generation facilities, but also a preview of multi-wavelength astrophysics with the wealth of high quality data available across the electromagnetic spectrum that can be easily accessed and analysed.

Future Observations

Water masers, polarisation and the radio counter-image in IRAS 10214

We have performed a deep ($\sigma \sim 2\ \mu$Jy beam^{-1}), full stokes *C*-band *JVLA* A-configuration observation of IRAS 10214 with three primary objectives:

1. Perform a polarisation experiment to delineate jet and star formation flux, measure the radio polarisation angle in as many resolution elements as possible, and attempt a rotation measure synthesis of this high redshift galaxy.

2. Make the first detection of the radio counter-image in IRAS 10214, yielding much tighter constraints on the level of preferential lensing of different emission components in this system, as detailed in this thesis.

3. Confirm the tentative 2.5-σ *JVLA* water maser detection in this galaxy (McKean et al., 2011).

   The observation employed the flexible WIDAR correlator capability of non-uniform channel widths enabling a simultaneous deep continuum and fine spectral-line experiment. The final data volume is of order 400 GB and unfortunately full analysis was not feasible under the time-scale of this thesis. This has the potential to be a definitive observation of IRAS 12014 due the sensitivity, resolution and wide bandwidth which will contain a wealth of spectral information. If the water maser emission is confirmed, and it emanates from a disk, this will provide direct kinematic estimate of the black hole mass with VLBI followup. This would be an important calibration check of the C IV FWHM method by Vestergaard & Peterson (2006), which relies on a low luminosity AGN reverberation mapping calibration to estimate the appropriate radius of the broad-line region.

CO SED Distortion Due to Preferential Lensing

In Chapter 4 we make the prediction that the CO SED will be distorted in a manner analogous to the continuum SED distortion that we have demonstrated in this thesis. This prediction is based on the assumption that the high-*J* lines have a smaller angular extent because they are partly excited by the AGN and perhaps a compact, circumnuclear starburst. Confirming this prediction will require the superb sensitivity and angular resolution of *ALMA*, once it is near full-commission (and is has 10-15 km baselines). This assumes *ALMA* is able to observe at low ($<20^\circ$) elevation successfully. The investigation of the magnitude of this effect is important as it could bias the statistical properties of the ISM drawn from samples of high-redshift, lensed galaxies.

High CO Transitions

The position of the *EVN* radio core suggests that IRAS 10214 has an AGN that is in very close proximity (few milli-arcseconds) of the modelled cusp of the caustic. This raises the opportunity to detect highly excited molecular gas that is AGN-heated and of small angular extent ($\lesssim$ 100 mas). The redshift of IRAS 10214 places the CO (10→9) rotational line in the centre of the 350 GHz observing window which can be accessed with the *James Clark Maxwell Telescope* (*JCMT*). Ground-based detections of such high rotational lines at high-redshift is of interest to compare with the recent low redshift detections made with *Herschel* spectroscopy (e.g. M 82, Panuzzo et al. 2010; Mrk 231, van der Werf et al. 2010). The excitation of these high-*J* lines was much higher than suggested by CO SED modelling and imply the presence of significant inter-stellar turbulence and X-ray heating from the active nucleus.

Temporal Monitoring of Highly-Magnified AGN

A highly magnified AGN suggests that a temporal monitoring programme could be of interest. Any continuum variations or transient phenomena (e.g. supernovae explosions) have the potential to be magnified by over two orders of magnitude and potentially enabling a detectable signal on reasonable time-scales. The radio sensitivity and angular resolution required is still seemingly impractical and will probably have to wait for the wide-field, high-resolution *SKA*.

Spatially Resolved Dust Continuum Map

Deep millimetre continuum observations to map the dust (at two temperatures) would be of interest in comparison with the resolved CO (1→0) map and the deep *JVLA C*-band observation. The barely resolved 1.2 mm continuum emission region presented in Ao et al. (2008) suggested that it was AGN heated due to its smaller extent when compared to the CO (3→2) and CO (1→0) maps. A direct test of this, as well as a spatially resolved dust-to-gas ratio, will investigate an outstanding piece of the puzzle regarding the ISM of IRAS 10214.

Appendix A

Other Projects

A.1 A VLBI Search for Binary Super-Massive Black Holes

Numerical simulations of the large-scale structure formation of the Universe reveal a process of hierarchical galaxy merging (e.g. Springel et al., 2005). Since every galaxy is expected to host a super-massive black hole (SMBH, Kormendy & Richstone, 1995), each galaxy merger should include a merger of SMBHs. We therefore expect binary SMBHs to be common in the Universe (see Colpi & Dotti, 2009). However, our observations at present do not concur with this forecasted ubiquity. This is an important disparity to reconcile as binary SMBHs are thought to play a significant role in galaxy formation and evolution models, specifically through the impact on the central galactic environment once the binary pair reach a separation of < 1 kpc (e.g. Merritt, 2006). This is likely to impact on the remarkable correlations between black hole mass and both stellar velocity dispersion and stellar bulge mass (Ferrarese & Merritt, 2000; Magorrian et al., 1998).

I have led a VLBI followup of low redshift (z ∼0.1-0.4) binary SMBHs candidates from double-peaked [O III]λ5007Åemitters with double nuclei detected with AO-assisted 0.1 arcsec, Keck *K*-band imaging. VLBI's high angular resolution holds a unique advantage in the unambiguous identification of binary SMBHs through high brightness temperature filtering and spectral index confirmation. Two strong candidates await confirmation with *EVN* scheduled for early 2012.

A.2 High-Redshift Water Masers: Direct Kinematic Black Hole Mass Measurements

In nearby AGN, water masers have been observed to be associated with interactions of jets and molecular cloud complexes; as well as AGN accretion disks. They are found in dense ($n > 10^7\,\mathrm{cm}^{-3}$), high temperature ($T > 300$ K) gas. At present, there is one confirmed 22 GHz water maser at $z >$0.66, MG J0414+0534, which is a lensed, $z \sim$2.5 Seyfert I (Impellizzeri et al., 2008). Direct kinematic M_{BH} measurements are possible with the disk masers in AGN accretion disks. These are highly lucrative at cosmological distances as they hold the potential to determine an early Universe black hole mass to $\sim$10% accuracy and similarly accurate measurement of the Hubble Parameter (with VLBI followup) through accurate distance measurements (e.g. Herrnstein et al., 1999; Braatz et al., 2010). Maser determined black hole masses are essential to test broad line width calibrated black hole masses (e.g. C IV, Vestergaard & Peterson 2006; Mg II, McLure & Jarvis 2002). These methods are bootstrapped to reverberation measurements which are only possible at low redshift on reasonable timescales. This means that significant systematics may exist, so direct tests at higher redshifts are essential.

I am involved in three separate efforts with the *JVLA* to detect high redshift water masers in AGN. The first is a 12 hr observation of IRAS 10214 as discussed in §7, a target which has shown tentative detection before with a factor 5 less sensitive observation.

Further work includes involvement in a survey of six obscured quasars (PI: Martínez-Sansigre). Their type 2 edge-on geometry allows long maser gain path-length for amplification and are thus more promising targets. These are also unaffected by magnification bias since they are not lensed objects - an important comparison with lensed counterparts. The third effort is with a group performing a survey of 9 far-infrared selected lensed galaxies, 8 of which were discovered with the *Herschel Space Observatory*.

Appropriate detections will be followed up with VLBI to attempt measurements of black hole masses (assuming a disk maser) and the Hubble Parameter once there are accurate lens models available.

A.3 Black Hole Accretion in *Herschel* selected FR-I's at $z \sim 2$

As discussed in the various chapter introductions to this thesis, a key observational goal in the field of galaxy evolution is to measure the relative bolometric luminosity of star formation and active central black holes at different cosmological epochs. Clear separation of the star formation and AGN components is not always possible, particularly in high redshift objects. VLBI provides a high resolution brightness temperature filter that enables an unambiguous measurement of the active core and jet flux on parsec scales at high redshift. This is a unique tool in the multi-wavelength study of targets that exhibit both AGN and SF characteristics. We are currently halfway through an EVN programme to followup a sample of FIR-NIR-radio selected galaxies at intermediate to high redshift (PI: Virdee, Oxford). The aim of this programme is to measure the core and jet flux and hence delineate these starburst/AGN into their respective components. A more challenging aim is to explore possible anti-correlations between star formation rate and jet size - indirectly testing the idea that radiative feedback from AGN and jet outflows quench star formation. Such analyses are challenging at present, however will become standard practice in the age of the *SKA*.

A.4 Ionospheric Total Electron Content Measurements: Radio Astronomy vs. Global Positioning System Cross-Correlation

A significant percentage of the first year of this D.Phil was spent on an ionospheric study. The charged layer of particles at altitudes between 50 - 1000 km above the Earth impose a phase delay on incoming electromagnetic waves. A non-uniform ionosphere above a radio array will cause differential phase delays which can only be solved for at a single point in an imaged astronomical field using traditional calibration techniques. This is a major challenge for next-generation low-frequency, wide-field arrays in design and development, particularly for EoR and intermediate redshift H I surveys to be performed by the *SKA* and its low frequency pathfinders.

This research includes a series of experiments based on long duration ($\sim$12 hour) *MERLIN* observations of amplitude and pointing calibrators. The self-calibration phase solutions of these observations are expected to have ionospheric corruptions modulated onto them as the ionospheric Total Electron Content (TEC) delays propagating electromagnetic waves with a wavelength squared ($\tau_{\rm TEC} \propto \lambda^2$) dependance. The goal of the experiment is to investigate if Global Positioning Satellites can provide useful priors in phase calibration. The measured phase delays from GPS satellites can be used to construct a 2D TEC map with coarse time resolution (5-10 mins). Phase solutions from the radio observations are cross-correlated with differential TEC measurements derived through pierce-points in the TEC maps. The *MERLIN* array was selected to ensure some baselines are resolved by the $\sim$1 deg ($\sim$110 km) spatial resolution of the TEC maps produced by ionospheric physicists. We chose 1.4 GHz to approximately match the GPS carrier frequency and avoid a large extrapolation. The result is no significant correlation despite seeing some clear large amplitude travelling ionospheric disturbances in the radio visibility data (observations were selected in 2003, close to solar maximum). It appears the lack of a correlation is due to the poor time resolution of the GPS TEC measurements. This is aggravated by the TEC smearing as a result of the appreciable distance a GPS satellite travels during a 5-10 minute integration. The next step is to investigate special sight-lines when the satellite and astronomical source have a small angular separation on the sky.

Bibliography

Alexander, D. M., Brandt, W. N., Smail, I., Swinbank, A. M., Bauer, F. E., Blain, A. W., Chapman, S. C., Coppin, K. E. K., Ivison, R. J. & Menéndez-Delmestre, K., 2008. Weighing the Black Holes in z $\sim$ 2 Submillimeter-Emitting Galaxies Hosting Active Galactic Nuclei. *AJ*, **135**, 1968–1981.

Alexander, D. M., Chartas, G., Bauer, F. E., Brandt, W. N., Simpson, C. & Vignali, C., 2005. A Chandra observation of the z= 2.285 galaxy FSC 10214+4724: evidence for a Compton-thick quasar? *MNRAS*, **357**, L16–L20.

Antonucci, R., 1993. Unified models for active galactic nuclei and quasars. *ARA&A*, **31**, 473–521.

Ao, Y., Weiss, A., Downes, D., Walter, F., Henkel, C. & Menten, K. M., 2008. The CO line SED and atomic carbon in IRAS F10214+4724. *A&A*, **491**, 747–754.

Bally, J., Lanber, W. D., Stark, A. A. & Wilson, R. W., 1987. Filamentary structure in the Orion molecular cloud. *ApJL*, **312**, L45–L49.

Barger, A. J., Cowie, L. L., Mushotzky, R. F., Yang, Y., Wang, W.-H., Steffen, A. T. & Capak, P., 2005. The Cosmic Evolution of Hard X-Ray-selected Active Galactic Nuclei. *AJ*, **129**, 578–609.

Barvainis, R., Antonucci, R., Hurt, T., Coleman, P. & Reuter, H.-P., 1995. The Broadband Spectral Energy Distributions of the Cloverleaf Quasar and IRAS F10214+4724. *ApJL*, **451**, L9.

Baskin, A. & Laor, A., 2005. What controls the CIV line profile in active galactic nuclei? *MNRAS*, **356**, 1029–1044.

Beasley, A. J., Gordon, D., Peck, A. B., Petrov, L., MacMillan, D. S., Fomalont, E. B. & Ma, C., 2002. The VLBA Calibrator Survey-VCS1. *ApJS*, **141**, 13–21.

Becker, R. H., White, R. L. & Helfand, D. J., 1995. The FIRST Survey: Faint Images of the Radio Sky at Twenty Centimeters. *ApJ*, **450**, 559.

Benford, D. J., Cox, P., Omont, A., Phillips, T. G. & McMahon, R. G., 1999. 350 Micron Dust Emission from High-Redshift Objects. *ApJL*, **518**, L65–L68.

Bennert, V. N., Auger, M. W., Treu, T., Woo, J.-H. & Malkan, M. A., 2011. The Relation between Black Hole Mass and Host Spheroid Stellar Mass Out to z ˜ 2. *ApJ*, **742**, 107.

Biggs, A. D., Younger, J. D. & Ivison, R. J., 2010. Deep, ultra-high-resolution radio imaging of submillimetre galaxies using Very Long Baseline Interferometry. *MNRAS*, **408**, 342–351.

BLANDFORD, R. D., KOCHANEK, C. S., KOVNER, I. & NARAYAN, R., 1989. Gravitational lens optics. *Science*, **245**, 824–830.

BOUWENS, R. J. & ILLINGWORTH, G. D., 2010. Very Blue UV-Continuum Slopes of Star-Forming Galaxies at z˜7 and the Evolution to z˜2-4. **1294**, 208–210.

BOYCE, E. R., BOWMAN, J. D., BOLTON, A. S., HEWITT, J. N. & BURLES, S., 2006. A Search for Radio Gravitational Lenses, Using the Sloan Digital Sky Survey and the Very Large Array. *ApJ*, **640**, 62–68.

BRAATZ, J. A., REID, M. J., HUMPHREYS, E. M. L., HENKEL, C., CONDON, J. J. & LO, K. Y., 2010. The Megamaser Cosmology Project. II. The Angular-diameter Distance to UGC 3789. *ApJ*, **718**, 657–665.

BROADHURST, T. & LEHAR, J., 1995. A Gravitational Lens Solution for the IRAS Galaxy FSC 10214+4724. *ApJL*, **450**, L41.

BROWN, J. C. & MCLEAN, I. S., 1977. Polarisation by Thomson Scattering in Optically Thin Stellar Envelopes. I. Source Star at Centre of Axisymmetric Envelope. *A&A*, **57**, 141.

BROWN, R. L. & VANDEN BOUT, P. A., 1991. CO emission at Z = 2.2867 in the galaxy IRAS F10214 + 4724. *AJ*, **102**, 1956–1959.

BUNDY, K., ELLIS, R. S., CONSELICE, C. J., TAYLOR, J. E., COOPER, M. C., WILLMER, C. N. A., WEINER, B. J., COIL, A. L., NOESKE, K. G. & EISENHARDT, P. R. M., 2006. The Mass Assembly History of Field Galaxies: Detection of an Evolving Mass Limit for Star-Forming Galaxies. *ApJ*, **651**, 120–141.

BUNKER, A. J., WILKINS, S., ELLIS, R. S., STARK, D. P., LORENZONI, S., CHIU, K., LACY, M., JARVIS, M. J. & HICKEY, S., 2010. The contribution of high-redshift galaxies to cosmic reionization: new results from deep WFC3 imaging of the Hubble Ultra Deep Field. *MNRAS*, **409**, 855–866.

BURNS, J. O., LAZIO, J., BALE, S., BOWMAN, J., BRADLEY, R., CARILLI, C., FURLANETTO, S., HARKER, G., LOEB, A. & PRITCHARD, J., 2012. Probing the first stars and black holes in the early Universe with the Dark Ages Radio Explorer (DARE). *Advances in Space Research*, **49**, 433–450.

CARILLI, C. L., 2011. Intensity Mapping of Molecular Gas During Cosmic Reionization. *ApJL*, **730**, L30.

CARILLI, C. L., DADDI, E., RIECHERS, D., WALTER, F., WEISS, A., DANNERBAUER, H., MORRISON, G. E., WAGG, J., DAVÉ, R., ELBAZ, D., STERN, D., DICKINSON, M., KRIPS, M. & ARAVENA, M., 2010. Imaging the Molecular Gas in a Submillimeter Galaxy at z = 4.05: Cold Mode Accretion or a Major Merger? *ApJ*, **714**, 1407–1417.

CARLSTROM, J. E., HOLDER, G. P. & REESE, E. D., 2002. Cosmology with the Sunyaev-Zel'dovich Effect. *ARA&A*, **40**, 643–680.

CHEN, B., DAI, X., KOCHANEK, C. S., CHARTAS, G., BLACKBURNE, J. A. & MORGAN, C. W., 2012. X-Ray Monitoring of Gravitational Lenses with Chandra. *ApJ*, **755**, 24.

CIRASUOLO, M., MCLURE, R. J., DUNLOP, J. S., ALMAINI, O., FOUCAUD, S. & SIMPSON, C., 2010. A new measurement of the evolving near-infrared galaxy luminosity function out to z ˜= 4: a continuing challenge to theoretical models of galaxy formation. *MNRAS*, **401**, 1166–1176.

CLOSE, L. M., HALL, P. B., LIU, C. T. & HEGE, E. K., 1995. Spectroscopic and Morphological Evidence That IRAS FSC 10214+4724 Is a Gravitational Lens. *ApJL*, **452**, L9.

COLES, P. & LUCCHIN, F., 2002. Cosmology: The Origin and Evolution of Cosmic Structure, Second Edition.

COLPI, M. & DOTTI, M., 2009. Massive Binary Black Holes in the Cosmic Landscape. *ArXiv e-prints*.

CONDON, J. J., 1997. Errors in Elliptical Gaussian FITS. *PSPS*, **109**, 166–172.

CONDON, J. J., COTTON, W. D. & BRODERICK, J. J., 2002. Radio Sources and Star Formation in the Local Universe. *AJ*, **124**, 675–689.

CONDON, J. J., COTTON, W. D., GREISEN, E. W., YIN, Q. F., PERLEY, R. A., TAYLOR, G. B. & BRODERICK, J. J., 1998. The NRAO VLA Sky Survey. *AJ*, **115**, 1693–1716.

CROOM, S. M., 2011. Do Quasar Broad-line Velocity Widths Add Any Information to Virial Black Hole Mass Estimates? *ApJ*, **736**, 161.

DADDI, E., ELBAZ, D., WALTER, F., BOURNAUD, F., SALMI, F., CARILLI, C., DANNERBAUER, H., DICKINSON, M., MONACO, P. & RIECHERS, D., 2010. Different Star Formation Laws for Disks Versus Starbursts at Low and High Redshifts. *ApJL*, **714**, L118–L122.

DEKEL, A. & SILK, J., 1986. The origin of dwarf galaxies, cold dark matter, and biased galaxy formation. *ApJ*, **303**, 39–55.

DELLER, A. T., BRISKEN, W. F., PHILLIPS, C. J., MORGAN, J., ALEF, W., CAPPALLO, R., MIDDELBERG, E., ROMNEY, J., ROTTMANN, H., TINGAY, S. J. & WAYTH, R., 2011. DiFX-2: A More Flexible, Efficient, Robust, and Powerful Software Correlator. *PSPS*, **123**, 275–287.

DODELSON, S., 2003. *Modern cosmology*.

DOWNES, D., RADFORD, J. E., GREVE, A., THUM, C., SOLOMON, P. M. & WINK, J. E., 1992. Submillimeter spectrum and dust mass of the primeval galaxy IRAS 10214 + 4724. *ApJL*, **398**, L25–L27.

DOWNES, D. & SOLOMON, P. M., 1998. Rotating Nuclear Rings and Extreme Starbursts in Ultraluminous Galaxies. *ApJ*, **507**, 615–654.

DUNLOP, J. S. & PEACOCK, J. A., 1990. The Redshift Cut-Off in the Luminosity Function of Radio Galaxies and Quasars. *MNRAS*, **247**, 19.

DYER, C. C. & SHAVER, E. G., 1992. On the rotation of polarization by a gravitational lens. *ApJL*, **390**, L5–L7.

EALES, S., DUNNE, L., CLEMENTS, D., COORAY, A., DE ZOTTI, G. ET AL., 2010. The Herschel ATLAS. *PSPS*, **122**, 499–515.

EFSTATHIOU, A., 2006. A model for the infrared emission of FSC 10214+4724. *MNRAS*, **371**, L70–L73.

EISENHARDT, P. R., ARMUS, L., HOGG, D. W., SOIFER, B. T., NEUGEBAUER, G. & WERNER, M. W., 1996. Hubble Space Telescope Observations of the Luminous IRAS Source FSC 10214+4724: A Gravitationally Lensed Infrared Quasar. *ApJ*, **461**, 72.

Eisenstein, D. J., Zehavi, I., Hogg, D. W., Scoccimarro, R., Blanton, M. R. et al., 2005. Detection of the Baryon Acoustic Peak in the Large-Scale Correlation Function of SDSS Luminous Red Galaxies. *ApJ*, **633**, 560–574.

Elmegreen, B. G., 1999. Galactic Bulge Formation as a Maximum Intensity Starburst. *ApJ*, **517**, 103–107.

Elvis, M., Wilkes, B. J., McDowell, J. C., Green, R. F., Bechtold, J., Willner, S. P., Oey, M. S., Polomski, E. & Cutri, R., 1994. Atlas of quasar energy distributions. *ApJS*, **95**, 1–68.

Evans, A. S., Scoville, N. Z., Dinshaw, N., Armus, L., Soifer, B. T., Neugebauer, G. & Rieke, M., 1999. Hubble Space Telescope NICMOS Observations of Rest-Frame Optical Continuum and Hα+[i] Emission In FSC 10214+4724. *ApJ*, **518**, 145–152.

Faber, S. M. & Gallagher, J. S., 1979. Masses and mass-to-light ratios of galaxies. *ARA&A*, **17**, 135–187.

Faber, S. M. & Jackson, R. E., 1976. Velocity dispersions and mass-to-light ratios for elliptical galaxies. *ApJ*, **204**, 668–683.

Ferrarese, L. & Merritt, D., 2000. A Fundamental Relation between Supermassive Black Holes and Their Host Galaxies. *ApJL*, **539**, L9–L12.

Flower, D. R. & Pineau des Forêts, G., 2001. The thermal balance of the first structures in the primordial gas. *MNRAS*, **323**, 672–676.

Frayer, D. T., Smail, I., Ivison, R. J. & Scoville, N. Z., 2000. The Identification of the Submillimeter Galaxy SMM J00266+1708. *AJ*, **120**, 1668–1674.

Gebhardt, K., Bender, R., Bower, G., Dressler, A., Faber, S. M., Filippenko, A. V., Green, R., Grillmair, C., Ho, L. C., Kormendy, J., Lauer, T. R., Magorrian, J., Pinkney, J., Richstone, D. & Tremaine, S., 2000. A Relationship between Nuclear Black Hole Mass and Galaxy Velocity Dispersion. *ApJL*, **539**, L13–L16.

Genzel, R. & Stutzki, J., 1989. The Orion Molecular Cloud and star-forming region. *ARA&A*, **27**, 41–85.

Goldreich, P. & Kwan, J., 1974. Molecular Clouds. *ApJ*, **189**, 441–454.

Golse, G. & Kneib, J.-P., 2002. Pseudo elliptical lensing mass model: Application to the NFW mass distribution. *A&A*, **390**, 821–827.

Gong, Y., Cooray, A., Silva, M., Santos, M. G., Bock, J., Bradford, C. M. & Zemcov, M., 2012. Intensity Mapping of the [C II] Fine Structure Line during the Epoch of Reionization. *ApJ*, **745**, 49.

Gong, Y., Cooray, A., Silva, M. B., Santos, M. G. & Lubin, P., 2011. Probing Reionization with Intensity Mapping of Molecular and Fine-structure Lines. *ApJL*, **728**, L46.

Goodrich, R. W., Miller, J. S., Martel, A., Cohen, M. H., Tran, H. D., Ogle, P. M. & Vermeulen, R. C., 1996. FSC 10214+4724: A Gravitationally Lensed, Hidden QSO. *ApJL*, **456**, L9.

GREENE, J. E. & HO, L. C., 2005. Estimating Black Hole Masses in Active Galaxies Using the Hα Emission Line. *ApJ*, **630**, 122–129.

GREGG, M. D., BECKER, R. H., WHITE, R. L., HELFAND, D. J., MCMAHON, R. G. & HOOK, I. M., 1996. The First Bright QSO Survey. *AJ*, **112**, 407.

GREVE, T. R., BERTOLDI, F., SMAIL, I., NERI, R., CHAPMAN, S. C., BLAIN, A. W., IVISON, R. J., GENZEL, R., OMONT, A., COX, P., TACCONI, L. & KNEIB, J.-P., 2005. An interferometric CO survey of luminous submillimetre galaxies. *MNRAS*, **359**, 1165–1183.

HÄRING, N. & RIX, H.-W., 2004. On the Black Hole Mass-Bulge Mass Relation. *ApJL*, **604**, L89–L92.

HASINGER, G., MIYAJI, T. & SCHMIDT, M., 2005. Luminosity-dependent evolution of soft X-ray selected AGN. New Chandra and XMM-Newton surveys. *A&A*, **441**, 417–434.

HELMBOLDT, J. F., TAYLOR, G. B., TREMBLAY, S., FASSNACHT, C. D., WALKER, R. C., MYERS, S. T., SJOUWERMAN, L. O., PEARSON, T. J., READHEAD, A. C. S., WEINTRAUB, L., GEHRELS, N., ROMANI, R. W., HEALEY, S., MICHELSON, P. F., BLANDFORD, R. D. & COTTER, G., 2007. The VLBA Imaging and Polarimetry Survey at 5 GHz. *ApJ*, **658**, 203–216.

HERNANDEZ, O. F. & HOLDER, G. P., 2011. The high-redshift neutral hydrogen signature of an anisotropic matter power spectrum. *JCAP*, **9**, 31.

HERRNSTEIN, J. R., MORAN, J. M., GREENHILL, L. J., DIAMOND, P. J., INOUE, M., NAKAI, N., MIYOSHI, M., HENKEL, C. & RIESS, A., 1999. A geometric distance to the galaxy NGC4258 from orbital motions in a nuclear gas disk. *Nat*, **400**, 539–541.

HOLT, J., TADHUNTER, C. N. & MORGANTI, R., 2008. Fast outflows in compact radio sources: evidence for AGN-induced feedback in the early stages of radio source evolution. *MNRAS*, **387**, 639–659.

HOPKINS, P. F., HERNQUIST, L., COX, T. J., DI MATTEO, T., ROBERTSON, B. & SPRINGEL, V., 2006. A Unified, Merger-driven Model of the Origin of Starbursts, Quasars, the Cosmic X-Ray Background, Supermassive Black Holes, and Galaxy Spheroids. *ApJS*, **163**, 1–49.

HUGHES, D. H., SERJEANT, S., DUNLOP, J., ROWAN-ROBINSON, M., BLAIN, A., MANN, R. G., IVISON, R., PEACOCK, J., EFSTATHIOU, A., GEAR, W., OLIVER, S., LAWRENCE, A., LONGAIR, M., GOLDSCHMIDT, P. & JENNESS, T., 1998. High-redshift star formation in the Hubble Deep Field revealed by a submillimetre-wavelength survey. *Nat*, **394**, 241–247.

ILBERT, O., SALVATO, M., LE FLOC'H, E., AUSSEL, H., CAPAK, P. ET AL., 2010. Galaxy Stellar Mass Assembly Between $0.2 < z < 2$ from the S-COSMOS Survey. *ApJ*, **709**, 644–663.

IMPELLIZZERI, C. M. V., MCKEAN, J. P., CASTANGIA, P., ROY, A. L., HENKEL, C., BRUNTHALER, A. & WUCKNITZ, O., 2008. A gravitationally lensed water maser in the early Universe. *Nat*, **456**, 927–929.

ISRAEL, F. P. & BAAS, F., 2002. Neutral atomic carbon in centers of galaxies. *A&A*, **383**, 82–90.

IVISON, R. J., PAPADOPOULOS, P. P., SMAIL, I., GREVE, T. R., THOMSON, A. P., XILOURIS, E. M. & CHAPMAN, S. C., 2011. Tracing the molecular gas in distant submillimetre galaxies via CO(1-0) imaging with the Expanded Very Large Array. *MNRAS*, **412**, 1913–1925.

IWASAWA, K., VIGNALI, C., EVANS, A. S., SANDERS, D. B. & TRENTHAM, N., 2010. The gravitationally lensed, luminous infrared galaxy IRAS F10214+4724 observed with XMM-Newton. **15**, 58–60.

JARVIS, M. J. & MCLURE, R. J., 2002. On the black hole mass-radio luminosity relation for flat-spectrum radio-loud quasars. *MNRAS*, **336**, L38–L42.

JARVIS, M. J. & MCLURE, R. J., 2006. Orientation dependency of broad-line widths in quasars and consequences for black hole mass estimation. *MNRAS*, **369**, 182–188.

KEETON, C. R., GAUDI, B. S. & PETTERS, A. O., 2003. Identifying Lenses with Small-Scale Structure. I. Cusp Lenses. *ApJ*, **598**, 138–161.

KEETON, C. R. & KOCHANEK, C. S., 1997. Determining the Hubble Constant from the Gravitational Lens PG 1115+080. *ApJ*, **487**, 42.

KETTENIS, M., VAN LANGEVELDE, H. J., REYNOLDS, C. & COTTON, B., 2006. ParselTongue: AIPS Talking Python. **351**, 497.

KLÖCKNER, H.-R., MARTÍNEZ-SANSIGRE, A., RAWLINGS, S. & GARRETT, M. A., 2009. High-redshift obscured quasars: radio emission at sub-kiloparsec scales. *MNRAS*, **398**, 176–188.

KOCHANEK, C. S., 1991. The implications of lenses for galaxy structure. *ApJ*, **373**, 354–368.

KOOPMANS, L. V. E., BIGGS, A., BLANDFORD, R. D., BROWNE, I. W. A., JACKSON, N. J., MAO, S., WILKINSON, P. N., DE BRUYN, A. G. & WAMBSGANSS, J., 2003. Extrinsic Radio Variability of JVAS/CLASS Gravitational Lenses. *ApJ*, **595**, 712–718.

KOOPMANS, L. V. E., BOLTON, A., TREU, T., CZOSKE, O., AUGER, M. W., BARNABÈ, M., VEGETTI, S., GAVAZZI, R., MOUSTAKAS, L. A. & BURLES, S., 2009. The Structure and Dynamics of Massive Early-Type Galaxies: On Homology, Isothermality, and Isotropy Inside One Effective Radius. *ApJL*, **703**, L51–L54.

KOOPMANS, L. V. E., TREU, T., BOLTON, A. S., BURLES, S. & MOUSTAKAS, L. A., 2006. The Sloan Lens ACS Survey. III. The Structure and Formation of Early-Type Galaxies and Their Evolution since z ˜ 1. *ApJ*, **649**, 599–615.

KORMANN, R., SCHNEIDER, P. & BARTELMANN, M., 1994. Isothermal elliptical gravitational lens models. *A&A*, **284**, 285–299.

KORMENDY, J. & RICHSTONE, D., 1995. Inward Bound—The Search For Supermassive Black Holes In Galactic Nuclei. *ARA&A*, **33**, 581.

KURK, J. D., WALTER, F., FAN, X., JIANG, L., RIECHERS, D. A., RIX, H.-W., PENTERICCI, L., STRAUSS, M. A., CARILLI, C. & WAGNER, S., 2007. Black Hole Masses and Enrichment of z ˜ 6 SDSS Quasars. *ApJ*, **669**, 32–44.

LACY, M., LAURENT-MUEHLEISEN, S. A., RIDGWAY, S. E., BECKER, R. H. & WHITE, R. L., 2001. The Radio Luminosity-Black Hole Mass Correlation for Quasars from the FIRST Bright Quasar Survey and a "Unification Scheme" for Radio-loud and Radio-quiet Quasars. *ApJL*, **551**, L17–L21.

LACY, M., RAWLINGS, S. & SERJEANT, S., 1998. IRAS F10214+4724: the inner 100pc. *MNRAS*, **299**, 1220–1230.

LAING, R. A., RILEY, J. M. & LONGAIR, M. S., 1983. Bright radio sources at 178 MHz - Flux densities, optical identifications and the cosmological evolution of powerful radio galaxies. *MNRAS*, **204**, 151–187.

LARSON, R. B., 1974. Effects of supernovae on the early evolution of galaxies. *MNRAS*, **169**, 229–246.

LAUER, T. R., TREMAINE, S., RICHSTONE, D. & FABER, S. M., 2007. Selection Bias in Observing the Cosmological Evolution of the M-σ and M-L Relationships. *ApJ*, **670**, 249–260.

LAWRENCE, A., ROWAN-ROBINSON, M., OLIVER, S., TAYLOR, A., MCMAHON, R. G., BROADHURST, T., SCARROTT, S. M., ROLPH, C. D., DRAPER, P. W., ELLIS, R. S., TADHUNTER, C., CONDON, J. J., LONSDALE, C. J., HACKING, P., CONROW, T., EFSTATHIOU, G. P. & SAUNDERS, W. S., 1993. Optical, infrared, radio and polarization imaging of the high-redshift galaxy IRAS F10214 + 4724. *MNRAS*, **260**, 28–36.

LE FÈVRE, O., ABRAHAM, R., LILLY, S. J., ELLIS, R. S., BRINCHMANN, J., SCHADE, D., TRESSE, L., COLLESS, M., CRAMPTON, D., GLAZEBROOK, K., HAMMER, F. & BROADHURST, T., 2000. Hubble Space Telescope imaging of the CFRS and LDSS redshift surveys - IV. Influence of mergers in the evolution of faint field galaxies from z˜1. *MNRAS*, **311**, 565–575.

LIDZ, A., FURLANETTO, S. R., OH, S. P., AGUIRRE, J., CHANG, T.-C., DORÉ, O. & PRITCHARD, J. R., 2011. Intensity Mapping with Carbon Monoxide Emission Lines and the Redshifted 21 cm Line. *ApJ*, **741**, 70.

LIU, R. & POOLEY, G., 1991. The correlated radio and optical asymmetries of powerful radio galaxies. *MNRAS*, **253**, 669–674.

MA, C., ARIAS, E. F., EUBANKS, T. M., FEY, A. L., GONTIER, A.-M., JACOBS, C. S., SOVERS, O. J., ARCHINAL, B. A. & CHARLOT, P., 1998. The International Celestial Reference Frame as Realized by Very Long Baseline Interferometry. *AJ*, **116**, 516–546.

MADAU, P., FERGUSON, H. C., DICKINSON, M. E., GIAVALISCO, M., STEIDEL, C. C. & FRUCHTER, A., 1996. High-redshift galaxies in the Hubble Deep Field: colour selection and star formation history to z˜4. *MNRAS*, **283**, 1388–1404.

MADAU, P., GHISELLINI, G. & FABIAN, A. C., 1994. The Unified Seyfert Scheme and the Origin of the Cosmic X-Ray Background. *MNRAS*, **270**, L17.

MAGORRIAN, J., TREMAINE, S., RICHSTONE, D., BENDER, R., BOWER, G., DRESSLER, A., FABER, S. M., GEBHARDT, K., GREEN, R., GRILLMAIR, C., KORMENDY, J. & LAUER, T., 1998. The Demography of Massive Dark Objects in Galaxy Centers. *AJ*, **115**, 2285–2305.

MARCONI, A. & HUNT, L. K., 2003. The Relation between Black Hole Mass, Bulge Mass, and Near-Infrared Luminosity. *ApJL*, **589**, L21–L24.

MARSHALL, P. J., TREU, T., MELBOURNE, J., GAVAZZI, R., BUNDY, K., AMMONS, S. M., BOLTON, A. S., BURLES, S., LARKIN, J. E., LE MIGNANT, D., KOO, D. C., KOOPMANS, L. V. E., MAX, C. E., MOUSTAKAS, L. A., STEINBRING, E. & WRIGHT, S. A., 2007. Superresolving Distant Galaxies with Gravitational Telescopes: Keck Laser Guide Star Adaptive Optics and Hubble Space Telescope Imaging of the Lens System SDSS J0737+3216. *ApJ*, **671**, 1196–1211.

MARTÍNEZ-SANSIGRE, A., RAWLINGS, S., LACY, M., FADDA, D., MARLEAU, F. R., SIMPSON, C., WILLOTT, C. J. & JARVIS, M. J., 2005. The obscuration by dust of most of the growth of supermassive black holes. *Nat*, **436**, 666–669.

MCKEAN, J. P., IMPELLIZZERI, C. M. V., ROY, A. L., CASTANGIA, P., SAMUEL, F., BRUNTHALER, A., HENKEL, C. & WUCKNITZ, O., 2011. A search for gravitationally lensed water masers in dusty quasars and star-forming galaxies. *MNRAS*, **410**, 2506–2515.

MCKEAN, J. P., KOOPMANS, L. V. E., FLACK, C. E., FASSNACHT, C. D., THOMPSON, D., MATTHEWS, K., BLANDFORD, R. D., READHEAD, A. C. S. & SOIFER, B. T., 2007. High-resolution imaging of the anomalous flux ratio gravitational lens system CLASS B2045+265: dark or luminous satellites? *MNRAS*, **378**, 109–118.

MCLURE, R. J., CIRASUOLO, M., DUNLOP, J. S., SEKIGUCHI, K., ALMAINI, O., FOUCAUD, S., SIMPSON, C., WATSON, M. G., HIRST, P., PAGE, M. J. & SMAIL, I., 2006. The discovery of a significant sample of massive galaxies at redshifts $5 < z < 6$ in the UKIDSS Ultra Deep Survey early data release. *MNRAS*, **372**, 357–368.

MCLURE, R. J. & JARVIS, M. J., 2002. Measuring the black hole masses of high-redshift quasars. *MNRAS*, **337**, 109–116.

MERRITT, D., 2006. Mass Deficits, Stalling Radii, and the Merger Histories of Elliptical Galaxies. *ApJ*, **648**, 976–986.

MERRITT, D. & FERRARESE, L., 2001. Black hole demographics from the M-σ relation. *MNRAS*, **320**, L30–L34.

MILLER, J. S. & GOODRICH, R. W., 1990. Spectropolarimetry of high-polarization Seyfert 2 galaxies and unified Seyfert theories. *ApJ*, **355**, 456–467.

MILLER, P., RAWLINGS, S., SAUNDERS, R. & EALES, S., 1992. A spectrophotometric study of BQS quasars. *MNRAS*, **254**, 93–110.

MILLER, S. H., BUNDY, K., SULLIVAN, M., ELLIS, R. S. & TREU, T., 2011. The Assembly History of Disk Galaxies. I. The Tully-Fisher Relation to z ˜= 1.3 from Deep Exposures with DEIMOS. *ApJ*, **741**, 115.

MOR, R., NETZER, H. & ELITZUR, M., 2009. Dusty Structure Around Type-I Active Galactic Nuclei: Clumpy Torus Narrow-line Region and Near-nucleus Hot Dust. *ApJ*, **705**, 298–313.

MORE, A., MCKEAN, J. P., MORE, S., PORCAS, R. W., KOOPMANS, L. V. E. & GARRETT, M. A., 2009. The role of luminous substructure in the gravitational lens system MG 2016+112. *MNRAS*, **394**, 174–190.

MORE, A., MCKEAN, J. P., MUXLOW, T. W. B., PORCAS, R. W., FASSNACHT, C. D. & KOOPMANS, L. V. E., 2008. Probing a massive radio galaxy with gravitational lensing. *MNRAS*, **384**, 1701–1710.

MUXLOW, T. W. B., PEDLAR, A., WILKINSON, P. N., AXON, D. J., SANDERS, E. M. & DE BRUYN, A. G., 1994. The Structure of Young Supernova Remnants in M82. *MNRAS*, **266**, 455.

NEGRELLO, M., HOPWOOD, R., DE ZOTTI, G., COORAY, A., VERMA, A. ET AL., 2010. The Detection of a Population of Submillimeter-Bright, Strongly Lensed Galaxies. *Science*, **330**, 800–.

NEUFELD, D. A. & MCKEE, C. F., 1988. Fermi acceleration of Lyman-alpha photons by shocks. *ApJL*, **331**, L87–L90.

NGUYEN, H. T., EISENHARDT, P. R., WERNER, M. W., GOODRICH, R., HOGG, D. W., ARMUS, L., SOIFER, B. T. & NEUGEBAUER, G., 1999. Hubble Space Telescope Imaging Polarimetry of the Gravitational Lens FSC 10214+4724. *AJ*, **117**, 671–676.

OBRESCHKOW, D., HEYWOOD, I., KLÖCKNER, H.-R. & RAWLINGS, S., 2009. A Heuristic Prediction of the Cosmic Evolution of the Co-luminosity Functions. *ApJ*, **702**, 1321–1335.

OBRESCHKOW, D., HEYWOOD, I. & RAWLINGS, S., 2011. Detecting Cold Gas at z=3 with ALMA and SKA. *ArXiv e-prints*.

OBRESCHKOW, D. & RAWLINGS, S., 2009. Understanding the H_2/HI ratio in galaxies. *MNRAS*, **394**, 1857–1874.

OTA, K., IYE, M., KASHIKAWA, N., SHIMASAKU, K., OUCHI, M., TOTANI, T., KOBAYASHI, M. A. R., NAGASHIMA, M., HARAYAMA, A., KODAKA, N., MOROKUMA, T., FURUSAWA, H., TAJITSU, A. & HATTORI, T., 2010. Lyα Emitters at z = 7 in the Subaru/XMM-Newton Deep Survey Field: Photometric Candidates and Luminosity Functions. *ApJ*, **722**, 803–811.

PANUZZO, P., RANGWALA, N., RYKALA, A., ISAAK, K. G., GLENN, J. ET AL., 2010. Probing the molecular interstellar medium of M82 with Herschel-SPIRE spectroscopy. *A&A*, **518**, L37.

PEI, Y. C., 1992. Interstellar dust from the Milky Way to the Magellanic Clouds. *ApJ*, **395**, 130–139.

PENG, C. Y., HO, L. C., IMPEY, C. D. & RIX, H.-W., 2010. Detailed Decomposition of Galaxy Images. II. Beyond Axisymmetric Models. *AJ*, **139**, 2097–2129.

PENG, C. Y., IMPEY, C. D., RIX, H.-W., KOCHANEK, C. S., KEETON, C. R., FALCO, E. E., LEHÁR, J. & MCLEOD, B. A., 2006. Probing the Coevolution of Supermassive Black Holes and Galaxies Using Gravitationally Lensed Quasar Hosts. *ApJ*, **649**, 616–634.

PERCIVAL, W. J., COLE, S., EISENSTEIN, D. J., NICHOL, R. C., PEACOCK, J. A., POPE, A. C. & SZALAY, A. S., 2007. Measuring the Baryon Acoustic Oscillation scale using the Sloan Digital Sky Survey and 2dF Galaxy Redshift Survey. *MNRAS*, **381**, 1053–1066.

PERLMUTTER, S., GABI, S., GOLDHABER, G., GOOBAR, A., GROOM, D. E. ET AL., 1997. Measurements of the Cosmological Parameters Omega and Lambda from the First Seven Supernovae at $z>=$ 0.35. *ApJ*, **483**, 565.

POOLEY, D., BLACKBURNE, J. A., RAPPAPORT, S. & SCHECHTER, P. L., 2007. X-Ray and Optical Flux Ratio Anomalies in Quadruply Lensed Quasars. I. Zooming in on Quasar Emission Regions. *ApJ*, **661**, 19–29.

PRITCHARD, J. R. & LOEB, A., 2008. Evolution of the 21cm signal throughout cosmic history. *Phy. Rev. D*, **78**(10), 103511.

RADFORD, S. J. E., DOWNES, D., SOLOMON, P. M., BARRETT, J. & SAGE, L. J., 1996. Resolution of the Discrepancy in the CO(3-2) Flux of IRAS F10214+4724. *AJ*, **111**, 1021.

RENGELINK, R. B., TANG, Y., DE BRUYN, A. G., MILEY, G. K., BREMER, M. N., ROETTGERING, H. J. A. & BREMER, M. A. R., 1997. The Westerbork Northern Sky Survey (WENSS), I. A 570 square degree Mini-Survey around the North Ecliptic Pole. *AAPS*, **124**, 259–280.

RIECHERS, D. A., CARILLI, C. L., MADDALENA, R. J., HODGE, J., HARRIS, A. I., BAKER, A. J., WALTER, F., WAGG, J., VANDEN BOUT, P. A., WEISS, A. & SHARON, C. E., 2011a. CO $(1\rightarrow 0)$ in $z > 2$ Quasar Host Galaxies: No Evidence for Extended Molecular Gas Reservoirs. *ApJL*, **739**, L32.

RIECHERS, D. A., HODGE, J., WALTER, F., CARILLI, C. L. & BERTOLDI, F., 2011b. Extended Cold Molecular Gas Reservoirs in z ˜= 3.4 Submillimeter Galaxies. *ApJL*, **739**, L31.

RIECHERS, D. A., WALTER, F., BREWER, B. J., CARILLI, C. L., LEWIS, G. F., BERTOLDI, F. & COX, P., 2008. A Molecular Einstein Ring at z = 4.12: Imaging the Dynamics of a Quasar Host Galaxy Through a Cosmic Lens. *ApJ*, **686**, 851–858.

ROWAN-ROBINSON, M., BROADHURST, T., OLIVER, S. J., TAYLOR, A. N., LAWRENCE, A., MCMAHON, R. G., LONSDALE, C. J., HACKING, P. B., CONROW, T., SAUNDERS, W., ELLIS, R. S., EFSTATHIOU, G. P. & CONDON, J. J., 1991. A high-redshift IRAS galaxy with huge luminosity - Hidden quasar or protogalaxy? *Nat*, **351**, 719–721.

ROWAN-ROBINSON, M., EFSTATHIOU, A., LAWRENCE, A., OLIVER, S., TAYLOR, A., BROADHURST, T. J., MCMAHON, R. G., BENN, C. R., CONDON, J. J., LONSDALE, C. J., HACKING, P., CONROW, T., SAUNDERS, W. S., CLEMENTS, D. L., ELLIS, R. S. & ROBSON, I., 1993. The ultraviolet-to-radio continuum of the ultraluminous galaxy IRAS F10214 + 4724. *MNRAS*, **261**, 513–521.

RUBIN, V. C., FORD, W. K. J. & . THONNARD, N., 1980. Rotational properties of 21 SC galaxies with a large range of luminosities and radii, from NGC 4605 /R = 4kpc/ to UGC 2885 /R = 122 kpc/. *ApJ*, **238**, 471–487.

SALPETER, E. E., 1955. The Luminosity Function and Stellar Evolution. *ApJ*, **121**, 161.

SCARROTT, S. M., ROLPH, C. D., WOLSTENCROFT, R. D., WALKER, H. J. & SEKIGUCHI, K., 1990. The Nature of the Bipolar Nebula Associated with IRAS:0731-0147. *MNRAS*, **245**, 484.

SCHMIDT, B. P., SUNTZEFF, N. B., PHILLIPS, M. M., SCHOMMER, R. A., CLOCCHIATTI, A. ET AL., 1998. The High-Z Supernova Search: Measuring Cosmic Deceleration and Global Curvature of the Universe Using Type IA Supernovae. *ApJ*, **507**, 46–63.

SCHNEIDER, N., SIMON, R., KRAMER, C., KRAEMER, K., STUTZKI, J. & MOOKERJEA, B., 2003. A multiwavelength study of the S 106 region. II. Characteristics of the photon dominated region. *A&A*, **406**, 915–935.

SCHNEIDER, P., 2006. Part 1: Introduction to gravitational lensing and cosmology. 1–89.

SCHUMACHER, H., MARTÍNEZ-SANSIGRE, A., LACY, M., RAWLINGS, S. & SCHINNERER, E., 2012. Gas and dust in a z= 2.8 obscured quasar. *MNRAS*, **423**, 2132–2146.

SCHWEITZER, M., LUTZ, D., STURM, E., GENZEL, R., VEILLEUX, S., RUPKE, D., KIM, D.-C., BAKER, A. J., GROVES, B., TOMONO, D., NETZER, H. & STERNBERG, A., 2007. Silicate Emission in AGN: Emission from the Torus or (and) Extended Emission? **373**, 501.

SCOVILLE, N. Z., YUN, M. S. & BRYANT, P. M., 1997. Arcsecond Imaging of CO Emission in the Nucleus of ARP 220. *ApJ*, **484**, 702.

SERJEANT, S., LACY, M., RAWLINGS, S., KING, L. J. & CLEMENTS, D. L., 1995. Spectroscopic evidence that the extreme properties of IRAS F10214+4724 are due to gravitational lensing. *MNRAS*, **276**, L31–L34.

SERJEANT, S., RAWLINGS, S., LACY, M., MCMAHON, R. G., LAWRENCE, A., ROWAN-ROBINSON, M. & MOUNTAIN, M., 1998. A spectroscopic study of IRAS F10214+4724. *MNRAS*, **298**, 321–331.

SHEN, Y., GREENE, J. E., STRAUSS, M. A., RICHARDS, G. T. & SCHNEIDER, D. P., 2008. Biases in Virial Black Hole Masses: An SDSS Perspective. *ApJ*, **680**, 169–190.

SHI, Y., RIEKE, G. H., HINES, D. C., GORJIAN, V., WERNER, M. W., CLEARY, K., LOW, F. J., SMITH, P. S. & BOUWMAN, J., 2006. 9.7 μm Silicate Features in Active Galactic Nuclei: New Insights into Unification Models. *ApJ*, **653**, 127–136.

SILK, J., 1968. Cosmic Black-Body Radiation and Galaxy Formation. *ApJ*, **151**, 459.

SILK, J., 2011. Feedback in Galaxy Formation. **277**, 273–281.

SIMPSON, C., WILSON, A. S., BOWER, G., HECKMAN, T. M., KROLIK, J. H. & MILEY, G. K., 1997. A One-sided Ionization Cone in the Seyfert 2 Galaxy NGC 5643. *ApJ*, **474**, 121.

SOLOMON, P. M., DOWNES, D. & RADFORD, S. J. E., 1992a. Dense molecular gas and starbursts in ultraluminous galaxies. *ApJL*, **387**, L55–L59.

SOLOMON, P. M., RADFORD, S. J. E. & DOWNES, D., 1992b. Molecular gas content of the primaeval galaxy IRAS 10214 + 4724. *Nat*, **356**, 318.

SOLOMON, P. M. & VANDEN BOUT, P. A., 2005. Molecular Gas at High Redshift. *ARA&A*, **43**, 677–725.

SPERGEL, D. N., BEAN, R., DORÉ, O., NOLTA, M. R., BENNETT, C. L. ET AL., 2007. Three-Year Wilkinson Microwave Anisotropy Probe (WMAP) Observations: Implications for Cosmology. *ApJS*, **170**, 377–408.

SPRINGEL, V., WHITE, S. D. M., JENKINS, A., FRENK, C. S., YOSHIDA, N., GAO, L., NAVARRO, J., THACKER, R., CROTON, D., HELLY, J., PEACOCK, J. A., COLE, S., THOMAS, P., COUCHMAN, H., EVRARD, A., COLBERG, J. & PEARCE, F., 2005. Simulations of the formation, evolution and clustering of galaxies and quasars. *Nat*, **435**, 629–636.

STURM, E., HASINGER, G., LEHMANN, I., MAINIERI, V., GENZEL, R., LEHNERT, M. D., LUTZ, D. & TACCONI, L. J., 2006. Mid-Infrared Spitzer Spectra of X-Ray-Selected Type 2 QSOs: QSO2s Are Not Ultraluminous Infrared Galaxies. *ApJ*, **642**, 81–86.

SUYU, S. H., MARSHALL, P. J., AUGER, M. W., HILBERT, S., BLANDFORD, R. D., KOOPMANS, L. V. E., FASSNACHT, C. D. & TREU, T., 2010. Dissecting the Gravitational lens B1608+656. II. Precision Measurements of the Hubble Constant, Spatial Curvature, and the Dark Energy Equation of State. *ApJ*, **711**, 201–221.

SUYU, S. H., MARSHALL, P. J., BLANDFORD, R. D., FASSNACHT, C. D., KOOPMANS, L. V. E., MCKEAN, J. P. & TREU, T., 2009. Dissecting the Gravitational Lens B1608+656. I. Lens Potential Reconstruction. *ApJ*, **691**, 277–298.

SWINBANK, A. M., BOWER, R. G., SMITH, G. P., SMAIL, I., KNEIB, J.-P., ELLIS, R. S., STARK, D. P. & BUNKER, A. J., 2006. Galaxies under the cosmic microscope: resolved spectroscopy and new constraints on the z = 1 Tully-Fisher relation. *MNRAS*, **368**, 1631–1645.

TEPLITZ, H. I., ARMUS, L., SOIFER, B. T., CHARMANDARIS, V., MARSHALL, J. A., SPOON, H., LAWRENCE, C., HAO, L., HIGDON, S., WU, Y., LACY, M., EISENHARDT, P. R., HERTER, T. & HOUCK, J. R., 2006. Silicate Emission in the Spitzer IRS Spectrum of FSC 10214+4724. *ApJL*, **638**, L1–L4.

THOMPSON, T. A., QUATAERT, E. & MURRAY, N., 2005. Radiation Pressure-supported Starburst Disks and Active Galactic Nucleus Fueling. *ApJ*, **630**, 167–185.

TREMAINE, S., GEBHARDT, K., BENDER, R., BOWER, G., DRESSLER, A., FABER, S. M., FILIPPENKO, A. V., GREEN, R., GRILLMAIR, C., HO, L. C., KORMENDY, J., LAUER, T. R., MAGORRIAN, J., PINKNEY, J. & RICHSTONE, D., 2002. The Slope of the Black Hole Mass versus Velocity Dispersion Correlation. *ApJ*, **574**, 740–753.

TREU, T., 2010. Strong Lensing by Galaxies. *ARA&A*, **48**, 87–125.

TREU, T. & KOOPMANS, L. V. E., 2004. Massive Dark Matter Halos and Evolution of Early-Type Galaxies to z ˜ 1. *ApJ*, **611**, 739–760.

TREU, T., WOO, J.-H., MALKAN, M. A. & BLANDFORD, R. D., 2007. Cosmic Evolution of Black Holes and Spheroids. II. Scaling Relations at z=0.36. *ApJ*, **667**, 117–130.

TRISTRAM, K. R. W., RABAN, D., MEISENHEIMER, K., JAFFE, W., RÖTTGERING, H., BURTSCHER, L., COTTON, W. D., GRASER, U., HENNING, T., LEINERT, C., LOPEZ, B., MOREL, S., PERRIN, G. & WITTKOWSKI, M., 2009. Parsec-scale dust distributions in Seyfert galaxies. Results of the MIDI AGN snapshot survey. *A&A*, **502**, 67–84.

TRISTRAM, K. R. W. & SCHARTMANN, M., 2011. On the size-luminosity relation of AGN dust tori in the mid-infrared. *A&A*, **531**, A99.

TSUBOI, M. & NAKAI, N., 1997. CO(1-0), CO(3-2), and HCN(3-2) observations of IRAS F10214+4724. **170**, 468.

TUMLINSON, J. & SHULL, J. M., 2000. Zero-Metallicity Stars and the Effects of the First Stars on Reionization. *ApJL*, **528**, L65–L68.

VAN DER WERF, P. P., ISAAK, K. G., MEIJERINK, R., SPAANS, M., RYKALA, A. ET AL., 2010. Black hole accretion and star formation as drivers of gas excitation and chemistry in Markarian 231. *A&A*, **518**, L42.

VANDEN BOUT, P. A., SOLOMON, P. M. & MADDALENA, R. J., 2004. High-Redshift HCN Emission: Dense Star-forming Molecular Gas in IRAS F10214+4724. *ApJL*, **614**, L97–L100.

VEGETTI, S. & KOOPMANS, L. V. E., 2009. Bayesian strong gravitational-lens modelling on adaptive grids: objective detection of mass substructure in Galaxies. *MNRAS*, **392**, 945–963.

VESTERGAARD, M. & PETERSON, B. M., 2006. Determining Central Black Hole Masses in Distant Active Galaxies and Quasars. II. Improved Optical and UV Scaling Relationships. *ApJ*, **641**, 689–709.

VOLONTERI, M., LODATO, G. & NATARAJAN, P., 2008. The evolution of massive black hole seeds. *MNRAS*, **383**, 1079–1088.

WANG, R., CARILLI, C. L., NERI, R., RIECHERS, D. A., WAGG, J., WALTER, F., BERTOLDI, F., MENTEN, K. M., OMONT, A., COX, P. & FAN, X., 2010. Molecular Gas in z ˜ 6 Quasar Host Galaxies. *ApJ*, **714**, 699–712.

WARREN, S. J. & DYE, S., 2003. Semilinear Gravitational Lens Inversion. *ApJ*, **590**, 673–682.

WEISS, A., DOWNES, D., HENKEL, C. & WALTER, F., 2005. Atomic carbon at redshift $\sim$2.5. *A&A*, **429**, L25–L28.

WEISS, A., DOWNES, D., NERI, R., WALTER, F., HENKEL, C., WILNER, D. J., WAGG, J. & WIKLIND, T., 2007. Highly-excited CO emission in APM 08279+5255 at z = 3.9. *A&A*, **467**, 955–969.

WHITE, R. L., BECKER, R. H., GREGG, M. D., LAURENT-MUEHLEISEN, S. A., BROTHERTON, M. S., IMPEY, C. D., PETRY, C. E., FOLTZ, C. B., CHAFFEE, F. H., RICHARDS, G. T., OEGERLE, W. R., HELFAND, D. J., MCMAHON, R. G. & CABANELA, J. E., 2000. The FIRST Bright Quasar Survey. II. 60 Nights and 1200 Spectra Later. *ApJS*, **126**, 133–207.

WILMAN, R. J. & FABIAN, A. C., 1999. Fitting the spectrum of the X-ray background: the effects ofhigh-metallicity absorption. *MNRAS*, **309**, 862–870.

WUCKNITZ, O., 2004. LENSCLEAN revisited. *MNRAS*, **349**, 1–13.

ZWART, J. T. L., BARKER, R. W., BIDDULPH, P., BLY, D., BOYSEN, R. C. ET AL., 2008. The Arcminute Microkelvin Imager. *MNRAS*, **391**, 1545–1558.